SYNTHESIS, STRUCTURE AND PROPERTIES OF HIGH PIEZO - AND FERROELECTRIC COMPLEX PEROVSKITE SYSTEMS

by

Yonghong Bing

B. Sc., Shandong University, 1986
M. Sc., Shandong University, 1992

THESIS SUBMITTED IN PARTIAL FULFILLMENT OF
THE REQUIREMENTS FOR THE DEGREE OF

Doctor of Philosophy

In the Department
of
Chemistry

SIMON FRASER UNIVERSITY

Summer 2005

APPROVAL

Name: Yonghong Bing

Degree: Doctor of Philosophy

Title of Thesis: Synthesis, Structure and Properties of High Piezo- and Ferroelectric Complex Perovskite Systems

Examining Committee:

Chair: Dr. V.E. Williams (Assistant Professor)

Dr. Z-G Ye (Professor)
Senior Supervisor

Dr. R.H. Hill (Professor)
Committee Member

Dr. G.W. Leach (Associate Professor)
Committee Member

Dr. S. Watkins (Professor)
Internal Examiner

Dr. L.E. Cross (Professor)
External Examiner
Materials Science and Electrical Engineering
Pennsylvania State University

Date Approved: May 24, 2005

SIMON FRASER UNIVERSITY

PARTIAL COPYRIGHT LICENCE

The author, whose copyright is declared on the title page of this work, has granted to Simon Fraser University the right to lend this thesis, project or extended essay to users of the Simon Fraser University Library, and to make partial or single copies only for such users or in response to a request from the library of any other university, or other educational institution, on its own behalf or for one of its users.

The author has further granted permission to Simon Fraser University to keep or make a digital copy for use in its circulating collection.

The author has further agreed that permission for multiple copying of this work for scholarly purposes may be granted by either the author or the Dean of Graduate Studies.

It is understood that copying or publication of this work for financial gain shall not be allowed without the author's written permission.\

Permission for public performance, or limited permission for private scholarly use, of any multimedia materials forming part of this work, may have been granted by the author. This information may be found on the separately catalogued multimedia material and in the signed Partial Copyright Licence.

The original Partial Copyright Licence attesting to these terms, and signed by this author, may be found in the original bound copy of this work, retained in the Simon Fraser University Archive.

W. A. C. Bennett Library
Simon Fraser University
Burnaby, BC, Canada

Abstract

The complex morphotropic phase boundary (MPB) behaviour of the relaxor ferroelectric-based (1-x)Pb($Sc_{1/2}Nb_{1/2}$)O_3 – xPbTiO_3 (PSN–PT) solid solution system has been investigated systematically by experiments with both ceramics and single crystals. The study of PSN–PT ceramics with compositions within the MPB region by means of dielectric spectroscopy has revealed two phase transitions. A new phase with monoclinic symmetry has been found by X-ray phase analysis. A new phase diagram of PSN–PT solid solution with the MPB region and a curved upper boundary has been established.

Single crystals of Pb($Sc_{1/2}Nb_{1/2}$)O_3 (PSN) and PSN–PT with compositions near or within MPB region have successfully been grown by an improved high temperature solution method using the mixtures of PbO and B_2O_3 as flux. The effects of the chemical compositions, such as the ratios of PSN–PT vs. flux and PbO vs. B_2O_3, on the morphology and quality of grown crystals have been studied. The optimum chemical compositions were proposed, which have led to the growth of high quality crystals. The PSN-PT single crystals of the MPB composition show two phase transitions and complex structure symmetry, typical of the MPB behaviour.

The spontaneous phase transitions from the paraelectric to a relaxor, then to a normal ferroelectric state upon cooling have been disclosed in the disordered Pb($Sc_{1/2}Nb_{1/2}$)O_3 single crystals, with the existence of macro domain state with a possible rhombohedral symmetry at room temperature. In comparison, the structural phase transitions and the dielectric properties of $Pb(Zn_{1/3}Nb_{2/3})O_3$ (PZN) single crystals were also investigated. The electric field induced phase transition from relaxor to ferroelectric state has been revealed and discussed in terms of the kinetics of phase transition in relaxors.

In our search for new materials with high piezoelectric performance, we have investigated the solid solution of $(1-x)PbSnO_3 - xPbTiO_3$ (PbSnTi) system. Single crystals of PbSnTi with composition $x \approx 0.60$, close to the MPB have been successfully grown for the first time from high temperature solution. The grown crystals exhibit good dielectric, piezo- and ferroelectric properties, which make them a new family of piezocrystals with relatively high Curie temperature ($T_C \approx 206$ °C), potentially promising for electromechanical transducer applications.

Dedication

To my dear parents, Dequan Bing and Shuhua,

my brother, Jiansheng, and my sister, Yongjie,

and my nephews, Younan, and Xinyu

To my beloved husband, Tian Mai, and adorable son, Hantao

Acknowledgements

I would like to express my deep and sincere thanks to my senior supervisor, Dr. Z.-G. Ye, for giving me the opportunity to work on this research project and for his extremely helpful guidance and strong supports in all aspects throughout this thesis work.

I extend my thanks to the members of my supervisory committee, Dr. R. H. Hill and Dr. G. W. Leach, for their valuable suggestions, advice, and encouragement during the course of this work.

I would also like to thank Dr. S. Watkins for being the internal examiner of my thesis.

I would like to thank Dr. L. E. Cross for the acceptance to be the external examiner of my thesis.

I extend my gratitude to Dr. B. Noheda and late Dr. G. Shirane for giving me the opportunity to work with them on synchrotron radiation experiments at the Brookhaven National Laboratory. Their valuable contribution forms an important part of this work.

I would like to thank all members of Dr. Ye's research group, both past and present, for providing me with help, support and friendship. Especially, I would like to thank Dr. A. A. Bokov for his great help and useful discussions on ferroelectrics and relaxors, and for his valued contribution in the studies of PZN crystals. I would like to

thank Ms. L. Zhang and Mr. W. Chen for providing the PZN single crystals studied in this work (**Chapter 8**).

I wish to thank Dr. D. Yang for his assistance in X-ray powder diffraction experiments performed in the Department of Physics.

I would like to thank the members of Department of Chemistry for their support.

The financial supports from the Department of Chemistry, Simon Fraser University, the Natural Sciences and Engineering Research Council of Canada and the U.S. Office of Naval Research are greatly appreciated.

Finally, I wish to thank to my parents for their encouragement in my work. Above all, I am greatly indebted to my husband, Tian Mai, as well as to our lovely son, Hantao Mai for their constant support and many personal sacrifices during my thesis work.

Table of Contents

List of Figures

List of Tables

List of Abbreviations

BT	$BaTiO_3$
CT	$CaTiO_3$
d_{33}	piezoelectric coefficient
DSC	differential scanning calorimetry
E_C	coercive field
ε'	real permittivity
ε_{max}	maximum dielectric constant
ε_{RT}	dielectric constant at room temperature
f_a	antiresonance frequency
f_r	resonance frequency
FWHM	the full width at half maximum
k_{33}	electromechanical coupling factors
λ	wavelength
MPB	morphotropic phase boundary
PbSnTi	$PbSnO_3–PbTiO_3$
PLM	polarized light microscopy
PMN	$Pb(Mg_{1/3}Nb_{2/3})O_3$
PMN-PT	$Pb(Mg_{1/3}Nb_{2/3})O_3–PbTiO_3$
PNR	polar nanoregion
PSN	$Pb(Sc_{1/2}Nb_{1/2})O_3$
PSN-PT (PSNT)	$Pb(Sc_{1/2}Nb_{1/2})O_3–PbTiO_3$
PST	$Pb(Sc_{1/2}Ta_{1/2})O_3$
PT	$PbTiO_3$

PZ	$PbZrO_3$
PZN	$Pb(Zn_{1/3}Nb_{2/3})O_3$
PZN-PT	$Pb(Zn_{1/3}Nb_{2/3})O_3–PbTiO_3$
PZT	$PbZrO_3–PbTiO_3$
ST	$SrTiO_3$
T_C	Curie temperature
T_L	the temperature at which the slow cooling process was stopped
T_{max}	the temperature of the maximum dielectric constant
T_{MPB}	the temperature corresponding to the MPB phase transition
T_{r-t}	the temperature corresponding to the phase transition from rhombohedral to tetragonal phase
XRD	X-ray diffraction

Chapter 1:
General Introduction

1.1 Piezoelectricity and Ferroelectricity

Piezoelectric materials provide a coupling between electrical and mechanical forces and hence can convert mechanical energy to electricity (and vice – versa) in various applications, such as transducers, actuators and medical imaging [1]. The development of an electrical polarization proportional to an applied mechanical stress is called the direct piezoelectric effect. Vice versa, the development of a geometric strain proportional to an applied electric field is called the converse effect [2]. These effects can be expressed, ignoring tensor components, by the equations [3, 4]:

$$D = dT + \varepsilon^T E \qquad \text{Direct Effect (generator),} \tag{1.1}$$

$$S = s^E T + dE \qquad \text{Converse Effect (motor),} \tag{1.2}$$

where D is the dielectric displacement (consider it equal to polarization), T stress, E electric field, S mechanical strain, d piezoelectric coefficient, s the materials compliance, and ε the dielectric constant. The superscripts indicate a quantity held constant: in ε^T, the stress is held constant, which means that the piezoelectric element is mechanically unconstrained; in the case of s^E, the electric field is held constant. In practice, these properties are directional quantities, and hence, usually specified with subscripts to identify the conditions under which they are determined. For instance, d_{33} indicates the polarization generated in the direction 3 when the stress is applied in the same direction, i.e.

$$D_3 = d_{33}T_3 \qquad \text{(Direct effect)}, \tag{1.3}$$

$$S_3 = d_{33}E_3 \qquad \text{(Converse effect)}, \tag{1.4}$$

where the piezoelectric coefficient, d_{33} is numerically equal in both equations. The d coefficients are usually expressed as (x 10^{-12}) C/N for the direct effect and (x 10^{-12}) m/V for the converse effect. In general, high d coefficients are desirable for those materials that are utilized in motional or vibrational devices, such as sonar and sounders.

Ferroelectrics are polar dielectrics for which the dipole moment can be switched between two or more equilibrium symmetry-equivalent states by application of an appropriate electric field [5]. A ferroelectric crystal is a material that exhibits one or more ferroelectric phases in a realizable range of temperature and pressure [6]. In the ferroelectric phase, the crystal is spontaneously electrically polarized. An internal structure of spontaneously electrically polarized domains is a characteristic feature of the ferroelectric phase.

The ferroelectrics are characterized by the ferroelectric hysteresis loop, i.e., the polarization P is a double-valued function of the applied electric field E [4]. Figure 1.1 shows typical polarization – electric field hysteresis loop displayed by ferroelectrics. The virgin curve represents the relationship between polarization and electric field when a small electric field applied. As the electric field is high enough, all the ferroelectric domains are aligned in the direction of the field, the crystal becomes monodomain and the polarization is saturated. The extrapolation of the linear portion of the curve at high field back to the polarization axis represents the value of the spontaneous polarization Ps. When the electric field is removed, most of the domains remain aligned and the crystal still exhibits polarization. The polarization at zero field after saturation is called remnant polarization P_r. The remnant polarization can be removed when a field in the opposite direction is applied and reaches a critical value. The strength of the electric field required to reduce the polarization to zero is called the coercive field E_C.

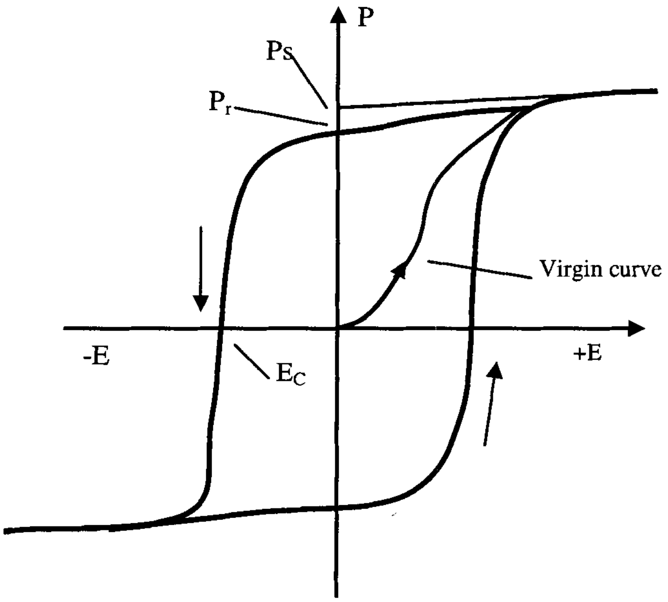

Figure 1.1: Typical polarization – electric field hysteresis loop displayed by ferroelectrics (adapted from Ref. [7])

Usually, the spontaneous polarization decreases when the temperature increases and falls to zero at a phase transition temperature T_C, which is called the Curie point. At temperatures above T_C the crystal does not exhibit ferroelectricity, and is in a non-polar phase, called a paraelectric phase. The ferroelectric structure of a crystal is created by a small distortion of the paraelectric structure, i.e. the lattice symmetry in the ferroelectric phase is always lower than that in the paraelectric phase. This low symmetry ferroelectric phase provides more than one possible polarization state with multiple equivalent local minima. The one dimensional free energy, in terms of free energy diagram (G) and polarization (P), showing two minima, is illustrated in Figure 1.2.

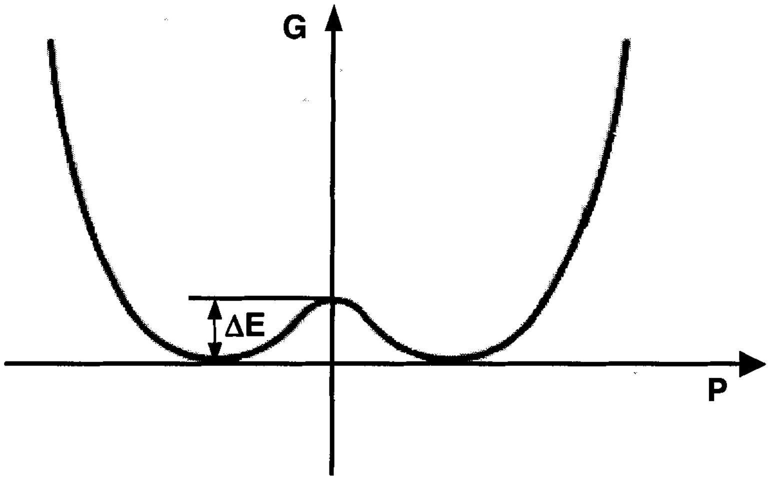

**Figure 1.2: One dimensional free energy diagram, in free energy (G) and polarization (P), showing two minima separated by a potential energy barrier (ΔE).
The minima correspond to the two possible polarization states +P and - P, after Jona [8]**

When the temperature decreases through the Curie point T_C, the properties that are temperature dependent, (such as dielectric, elastic, optical, and thermal properties) of a ferroelectric crystal show anomalies. A typical example is given by the dielectric permittivity as a function of temperature for normal ferroelectric materials, which shows a sharp anomaly at T_C (Figure 1.3).

In most ferroelectrics, the temperature dependence of the dielectric constant at temperatures above T_C follows the Curie-Weiss law:

$$\varepsilon = \frac{C}{T-\Theta} + \varepsilon_\infty \quad , \tag{1.5}$$

where ε is the dielectric permittivity, C is the Curie constant, Θ is the Curie-Weiss temperature and ε_∞ is the contribution of electronic polarization to the dielectric constant which can be neglected at temperatures near T_C.

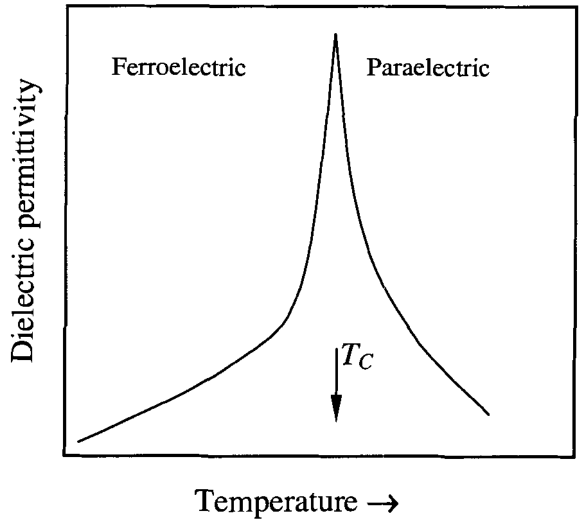

Figure 1.3: An illustration of dielectric permittivity as a function of temperature for normal ferroelectrics. The sharp anomaly corresponds to the phase transition at T_C.

1.2 Simple Perovskite Compounds: $BaTiO_3$ and $PbTiO_3$

The cubic perovskite structure, which is the high temperature form for many mixed oxides of the ABO_3 type, was one of the first simple structures identified for compounds that exhibit ferroelectric properties, and is still probably the most important ferroelectric prototype [6]. The simple cubic structure (point symmetry *m3m*) (Figure 1.4) is made up of a regular array of corner-sharing oxygen octahedra with smaller highly-charged cations like Ti^{4+}, Sc^{3+}, Nb^{5+}, Zr^{4+}, Sn^{4+}, etc, occupying the central octahedral B site, and lower-charged, larger cations like Ba^{2+}, Pb^{2+}, Ca^{2+}, etc, filling the interstices between octahedra in the larger 12-coordinated A-sites.

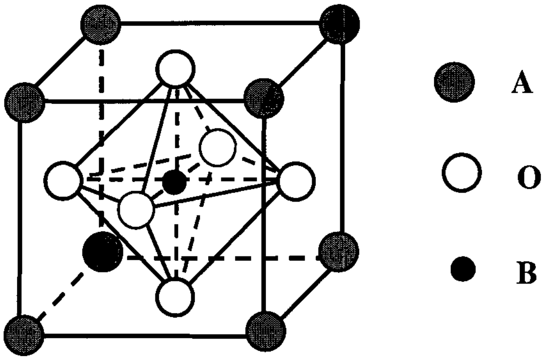

Figure 1.4: Cubic (m3m) prototype structure of perovskite-type ABO_3 compounds. For $BaTiO_3$, A = Ba^{2+}, B = Ti^{4+}, and O = O^{2-}.

Barium titanate ($BaTiO_3$) was the first perovskite-type compound shown to be ferroelectric and is to date, one of the most thoroughly investigated ferroelectric materials [6, 8]. The characteristic feature of $BaTiO_3$ unit cells is the TiO_6-octahedra, which, because of their high polarizability, essentially determine the dielectric properties. The high polarizability, is due to the fact the small Ti^{4+} ions have relatively more space within the oxygen octahedra. The cubic unit-cell with the Ti^{4+} ion in the center of the oxygen octahedron is, however, stable only above the Curie point T_C of about 130 °C. Below T_C the Ti^{4+} ions occupy off-center positions. This transition to the off-center position at T_C results in a series of important physical consequences. The crystal structure changes from cubic (C) to tetragonal (T), then to orthorhombic (O), and finally to a rhombohedral (R) phase. Passing through this sequence, a spontaneous polarization P_S appears, the direction of which is in the tetragonal phase alone one of the 6 edges, in the orthorhombic phase along one of the 12 surface diagonals, and in the rhombohedral phase along one of the 8 space diagonals of the ideal cubic unit cell. The direction of P_S can be switched by high electric field between the different crystallographically allowed positions, which are characteristic in each ferroelectric phase. In practice, $BaTiO_3$ has the ability to form extensive solid solutions. By this means, a wide variety of materials with continuously changing electrical properties can be produced.

$PbTiO_3$ is another well known perovskite compound and has the same type of crystal structure as that of $BaTiO_3$ [9], and its tetragonality increases with lead content, accompanying the rise of Curie temperature (490 ^{o}C), at which $PbTiO_3$ undergoes a single ferroelectric transition from the cubic to a tetragonal phase. $PbTiO_3$ shares the same features as $BaTiO_3$, and has the ability to form extensive solid solutions.

1.3 Relaxor Ferroelectrics

Relaxor ferroelectrics differ from normal ferroelectrics such as $BaTiO_3$ by three distinct phenomena [10, 11]:

(1) The relaxor ferroelectrics exhibit a broad maximum and a significant frequency dispersion of the dielectric permittivity (Figure 1.5), with the temperature of the maximum dielectric constant (T_{max}) increasing and its magnitude (ε_{max}) decreasing with increasing frequency.

(2) No macroscopic phase transition into a ferroelectric state takes place around T_{max}, not even a "diffuse" one. Neither birefringence nor macro polarization can develop without application of an electric field, the materials remaining isotropic to long coherent probing radiation, like polarized light, X-ray and neutron beams.

(3) The local polarization and nanopolar domains appear below a temperature T_d far above that of the maximum permittivity T_{max}, while the (induced) macro polarization vanishes at a temperature well below T_{max}.

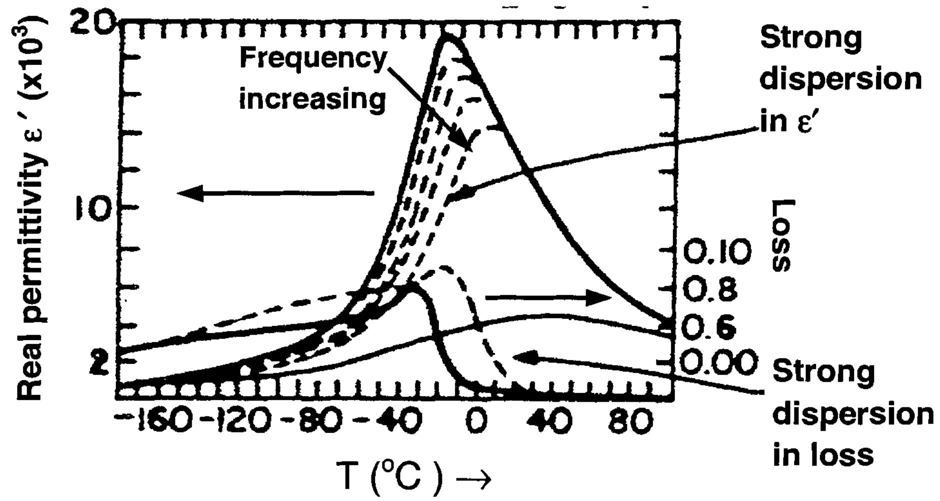

Figure 1.5: Characteristic features of a ferroelectric relaxor (Adapted from Cross Ref. [10]).

The crystal chemistry and structure features of relaxor ferroelectrics can be described in terms of the microstructural features, correlation of the local polar domains, order-disorder and nanostructure [11]. Figure 1.6 shows the schematic distribution of cations upon the B site of a complex $A(B_1B_2)O_3$ perovskite [10]. There are large B_1 or B_2 rich regions in Figure 1.6(a) that reveal the chemical disordered state. It is suggested that in these statistical composition fluctuations, i.e. random distributions of B_1 (B site cation with lower valence state) and B_2 (B site cation with high valence state) in the perovskite B-site, the translational symmetry, found in normal ferroelectrics, is strongly broken into a local polar region because of the different charged ions [12]. If however, that structure is ordered [Figure 1.6(b)], full translational symmetry is recovered, and the composition is completely uniform down to the unit cell scale. It is concluded [11] that [take $Pb(Mg_{1/3}Nb_{2/3})O_3$ (PMN) as an example] the ion shifts from their ideal positions at high temperature in long range structure, together with local polar structure, the chemical disorder and the related lattice distortion in the intermediate- and short-range structure, represent some structural factors essential to the relaxor behaviour.

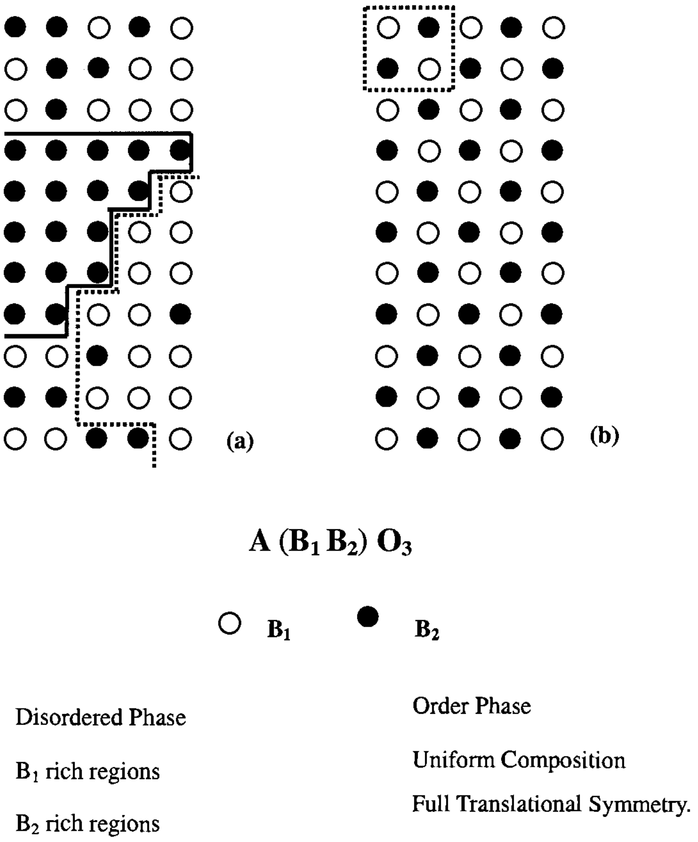

Figure 1.6: Two-dimensional illustration of chemical order-disorder in a hypothetical B_1: B_2 system, and expected consequences for $Pb(B_1: B_2)O_3$ perovskite (after Cross, [10]).

The effects of chemical ordering on the relaxor ferroelectric properties were initially studied in $Pb(Sc_{1/2}Ta_{1/2})O_3$ by Stenger [13, 14, 15], and Setter and Cross [16, 17], and since then have been extensively investigated [18, 19, 20]. It is found that with an increasing degree of order, the coherence length between the local polar domains increases, and a transition into a normal ferroelectric phase takes place. This phenomenon demonstrates that the fluctuation in the concentration of B-sites cations is responsible for the diffuse nature of the phase change in a $Pb(B_1B_2)O_3$ perovskite relaxor ferroelectric [10].

Various models have been proposed for the possible mechanisms of the dispersive dielectric relaxation and the polarization behaviour. The earliest model was proposed by Smolenskii, Isupov *et al.* [21, 22]. They pointed out that the compositional fluctuations on the B-sites with disordered B_1 and B_2 occupation cause the chemical inhomogeneity. Variation of the concentrations of B_1 and B_2 in different micro-regions gives rise to different local Curie temperature. The temperature T_{max} represents the mean Curie temperature. Therefore, the summed distribution of these micro-regions gives the broadened phase transition.

A superparaelectric model for the relaxor ferroelectrics was proposed by Cross [10] by analogy with the superparamagnetic state. This model pointed out that in the high temperature region, the micro polar regions are being dynamically disordered by thermal motion. The height of the barrier between domain states is directly proportional to the volume of the polar microregion. The polarizations with low thermal energies will be trapped into a preferential orientation and form a polar microdomain or cluster. The superparaelectric model accurately describes many of the observed properties of ferroelectric relaxors such as the frequency dependence of the permittivity, dielectric aging, metastable switching from micro- to macro domain states, and the nonlinear behaviour of the thermoelastic and optical properties.

The superparaelectric model has been extended by Veihland *et al.* [23], who described the dispersion of the maximum dielectric constant temperature, T_{max}, in terms of the AC frequency f by the Vogel-Fulcher (V-F) relationship,

$$f = f_0 \exp[-E_a/(T_{max}-T_f)] \qquad , \qquad (1.6)$$

where f_0, E_a, and T_f are the fitting parameters. The T_f is described as a static freezing temperature, at which the system freezes into a frustrated state (the state that dipole moment hesitate to choose the direction). It is believed that the polar clusters within the materials are interacting with dipolar fields to "freeze out" at T_f into a long range ordered ferroelectric.

A mechanism of random field-stabilized domain states was proposed by Westphal and Kleemann [24]. They proposed that the relaxor ferroelectricity in PMN can be attributed to the strong contribution of quenched random electric fields, arising from the charged nanodomains and the compositional fluctuations and chemical textures. The random fields are believed to be at the origin of the slowing down of the growing long range polar order, and freezing into nanometric ferroelectric domains and the slow relaxation of the polarization below the Curie temperature.

By means of dielectric spectroscopy, Bokov and Ye [25, 26, 27] have discovered a "universal" relaxor dispersion in PMN and related materials, and showed that it is an important common property of relaxor ferroelectrics. The universal relaxor polarization is described by a microscopic model of 'soft' polar nanoregions with unit cells that can freely choose several different directions, while the direction of the total moment of the nanoregion remains the same [27]. Such an approach makes it possible to apply a standard spherical model to relaxor ferroelectrics, which predicts the experimentally observed quadratic divergence of the universal part of the susceptibility above the critical temperature. This model is complementary to the so-called spherical random bond – random field model proposed by Blinc *et al.* [28, 29] to explain the NMR data and the non-linearity of the total dielectric susceptibility in relaxors.

The permittivity in a wide temperature range above T_{max} for $0.75PbMg_{1/3}Nb_{2/3}O_3 - 0.25PbTiO_3$ relaxor ceramics was successfully modeled by a single shape parameter, δ, using a quadratic law [30],

$$\frac{\varepsilon_A}{\varepsilon} = 1 + \frac{(T - T_A)^2}{2\delta_A^2} \quad , \tag{1.7}$$

where T_A ($< T_{max}$) and ε_A ($> \varepsilon_{max}$) are the parameters defining the temperature position of the peak and the extrapolated value of ε at $T = T_A$, respectively, and they should be independent of the frequency of the measurements. The parameter δ_A, also being practically independent of frequency, can be considered as a convenient measure for the degree of diffuseness of the permittivity peaks in relaxors. It was demonstrated [31] that the data for a large number of relaxors with different broadness of $\varepsilon(T)$ maximum can be collapsed perfectly onto a single scaling line with this quadratic law.

1.4 $PbTiO_3$-Containing Solid Solution and Morphotropic Phase Boundary (MPB)

1.4.1 Solid Solution of $PbZrO_3$-$PbTiO_3$ – The Phenomenon of Morphotropic Phase Boundary

For many years, lead zirconate-titanate solid solutions, $(1\text{-}x)PbZrO_3 - xPbTiO_3$ (PZT), were recognized as the number one high-performance piezoelectric perovskite materials and are the basis of practically all transducers and other piezoelectric devices.

This solid solution is cubic at high temperatures but becomes slightly distorted at lower temperatures, where it is ferroelectric [32]. Except for a narrow region close to $PbZrO_3$, the ferroelectric phase diagram is divided into two regions of different symmetry, rhombohedral for Zr-rich compositions and tetragonal for Ti-rich compositions [33]. The highest piezoelectric response in this system is found at the boundary between these two phases ($x \approx 0.47$) – the so-called morphotropic phase boundary (MPB). The term "morphotropic" was proposed by Jaffe *et al.* [34] and means literally "the boundary between two forms."

For nearly four decades, the excellent physical properties of PZT were associated with the nature of the MPB, especially in the concept of the coexistence of rhombohedral and tetragonal phases. However, the recent discovery of a monoclinic phase in PZT at the MPB has changed this picture dramatically [35]. A new phase diagram [36] has been reported and it is shown in Figure 1.7. The monoclinic region forms a narrow triangle in between the tetragonal and rhombohedral phases, with an essentially vertical rhombohedral-monoclinic boundary and a slightly slanted tetragonal-monoclinic boundary, which agrees very well with the original MPB reported by Jaffe *et al.* [34] above room temperature. It is believed that this new monoclinic phase is the key to understanding the anomalously high piezoelectric response in PZT. The advantage of this structure is that the polarization vector is no longer constrained to lie along a symmetry axis, as in the rhombohedral or tetragonal structure, but instead can rotate within the monoclinic plane and this easy rotation is responsible for the high values of the piezoelectric coefficient in PZT [37, 38].

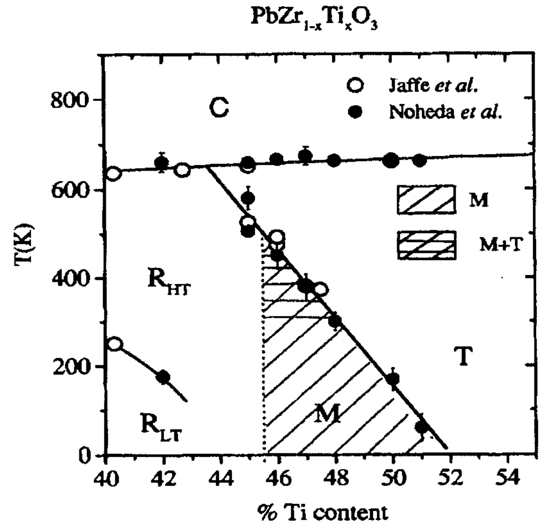

Figure 1.7: New (1-x)$PbZrO_3$ – $x$$PbTiO_3$ phase diagram around MPB. The solid symbols are the results from the work by Noheda *et al.* [36]. Data from Jaffe *et al.* (Ref. [34]) and Amin *et al.* (Ref. [39] are represented by open circles. The monoclinic region is shaded with diagonal lines. Horizontal lines are superimposed in the region of tetragonal-monoclinic phase coexistence. For x = 0.45, the solid symbols represent the limits of the tetragonal-rhombohedral coexistence region. (Ref. [36])*

1.4.2 Relaxor-Ferroelectric Solid Solutions and High Performance Piezocrystals

In their study of the MPB behaviour, Du *et al.* [40] used a phenomenological approach and found a great enhancement of the piezoelectric response in the <001>-oriented PZT with rhombohedral symmetry. Since the polar symmetry axes for tetragonal samples are known to be [001] that for rhombohedral samples is [111], the electric field or stress needs to be applied along those directions in order to be efficient. Accordingly, the largest piezoelectric deformations would be along the polar direction. Enhanced

---

* Reprinted with permission from authors, Physical Review B, Vol. 63, 014103, December 12, 2000 (Figure 6), p7 as follows: Copyright 2000 by the American Physical Society. At the request of APS, the following link is provided [http://link.aps.org/abstract/PRB/v63/e014103], and this notice is published: Readers may view, browse, and/or download material for temporary copying purposes only, provided these uses are for noncommercial personal purposes. Except as provided by law, this material may not be further reproduced, distributed, transmitted, modified, adapted, performed, displayed, published, or sold in whole or part, without prior written permission from the publisher.

piezoelectric responses occurring along the directions other than the polar direction would be unexpected. These factors brought about new research interest in the study of the dependence of the piezoelectric response on crystal orientation [41]. From this point of view, the need for single crystals and single domain studies were recognized. Unfortunately, PZT has proven difficult to study in this way due to difficulties in its crystal growth. More recently studies of the $Pb(Zn_{1/3}Nb_{2/3})O_3$ – $PbTiO_3$ (PZN-PT) and $Pb(Mg_{1/3}Nb_{2/3})O_3$ – $PbTiO_3$ (PMN-PT) have yielded "respectable" crystals for compositions close to the morphotropic phase boundaries between rhombohedral and tetragonal phases in both systems [42, 43]. In the early 1980s, Kuwata *et al.* [44] had already reported very high piezoelectric response in <001>-oriented single crystals of PZN-PT. Later, Shrout *et al.* [45] also reported the orientation dependence of the dielectric properties in the system of PMN-PT single crystals. But it was only recently when Park and Shrout [43, 46] reported ultra-high electromechanical strain values (up to 1.7% at high E-field), high piezoelectric coefficients ($d_{33} > 2500$ pC/N), and high electromechanical coupling factors ($k_{33} > 90\%$) attained in rhombohedral single crystals of PZN-PT and PMN-PT oriented along the [001] direction, that the potential of these systems in the next generation of electromechanical transducer devices has been appreciated.

The relationship between piezoelectric properties and crystal composition and orientation were studied for PZN-PT [46] and Figure 1.8 presents the piezoelectric coefficients d_{33} as a function of composition and crystal orientation for PZN-PT crystals. The remarkable thing is that all rhombohedral crystals oriented along their pseudocubic [001] direction exhibited large piezoelectric coefficients. Maximum d_{33} value of 2500 pC/N was determined with rhombohedral PZN-8% PT crystals oriented along [001]. Although [111] is the polar direction for rhombohedral crystals, this cut exhibits a quite poor piezoelectric response. In fact, the electromechanical coupling factor k_{33} and piezoelectric coefficients d_{33} of <111>-oriented rhombohedral crystals were found to be only 35% and 80 pC/N, respectively, regardless of composition.

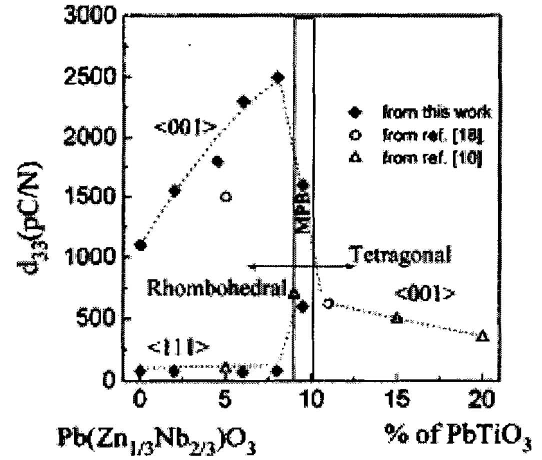

Figure 1.8: Piezoelectric coefficient d_{33} as a function of composition and orientation for $Pb(Zn_{1/3}Nb_{2/3})O_3$ – $PbTiO_3$ crystals. (Ref. [46][*]); A solid diamond: Ref: [46]; Open circle: Ref. [47]; Open triangle: Ref. [44].

The origin of the large piezoelectric properties for PZN-PT and PMN–PT single crystals was initially proposed by the same authors [46]. The very high electromechanical deformation in <001>-oriented rhombohedral crystal was related to an electric-field-induced phase transformation from rhombohedral to the tetragonal phase, as shown in Figure 1.9. Later, Durbin *et al.* [48] confirmed this assertion by performing X-ray diffraction experiments on PZN–8%PT crystals with an electric field applied in situ along the [001] direction.

---

[*] Reprinted with permission from Seung-Eek Park and Thomas R. Shrout, Journal of Applied Physics, 82, 1804 (1997). Copyright 1997, American Institute of Physics.

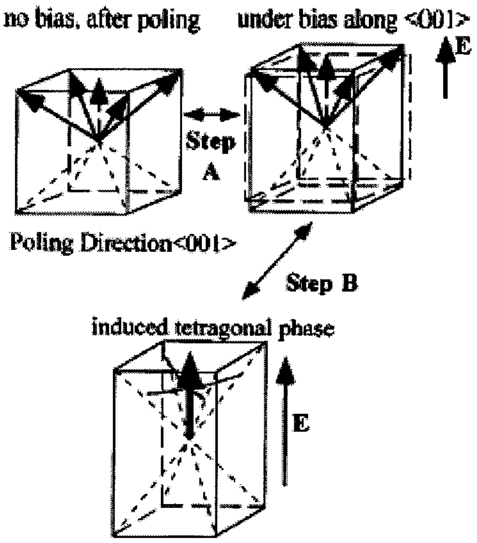

Figure 1.9: Schematic diagram of domain configurations in <001>-oriented rhombohedral crystals under bias (step A-piezoelectricity, step B-induced phase transition) ([46]).

In light of the discovery of a new monoclinic phase in the PZT ceramics, the phase diagram of PZN–PT and PMN–PT system were revisited by many researchers (see review by Noheda [49]). In the PZN-PT system, an orthorhombic phase was found to exist between the rhombohedral and the tetragonal phases at approximately 10%PT [50]. Upon application of an electric field along [001], evidence of polarization rotation via a monoclinic phase has been shown for PZN–8%PT [51]. In the PMN–PT system, a ferroelectric monoclinic phase has recently been discovered in PMN–35%PT crystals by means of high-resolution synchrotron X-ray diffraction [52]. Ye and Dong [53] reported the domain structure and phase transitions occurring in morphotropic (1-x)PMN – xPT single crystals. Xu *et al.* [54] observed monoclinic domains coexisting with rhombohedral domains in a PMN–33%PT crystal. A monoclinic phase has also been detected for (1-x)PMN – xPT system in the composition range of 31–37%PT in several other studies [55, 56, 57].

All these studies show that the nature and phase components of the MPB are very complicated, especially with the presence of the monoclinic phase [58]. The MPB and related effects are believed to be responsible for the excellent piezoelectric properties of the relaxor piezocrystals because crystals of compositions near MPB possess all the possible polarization orientation states of the coexisting MPB phases.

1.5 Current Status of Piezocrystals Growth

Various techniques, such as the flux method, top-seeded solution growth and modified Bridgman method, have been applied for the growth of piezocrystals [59, 60, 61]. In the improved flux growth method, chemical (flux composition and flux ratio) and thermal (profile, soaking temperature, cooling rates, etc.) parameters have been systematically investigated and optimized. The mixture of ($PbO+\delta B_2O_3$) was found to be an effective solvent for the growth of piezocrystals by combining the advantage of both the borate and PbO solvent. By appropriately adjusting the chemical and thermal parameters, PMN–PT and PZN–PT crystals of high quality with respectable size and regular morphology were grown [59, 62, 63]. Ref. [58] gives a review on the growth of piezocrystals.

High performance single crystal piezoelectricity has been reviewed by Park and Hackenberger [1]. The electromechanical properties and the uses of various PZT ceramics and single crystals have been summarized in Table 1.1.

Table 1.1: Electromechanical properties and device applications of (1-x)$PbZrO_3$ – $xPbTiO_3$ ceramics and relaxor-PT single crystals (Ref. [1]).

Materials type	Type II* PZT ceramics	Type III* PZT ceramics	Type VI* PZT ceramics	PZN–4.5%PT crystals[a]	PMN–33%PT crystals[a]
Dielectric constant (RT)	2050	1000	3900	5000	8000
Dielectric loss	0.018	0.003	0.025	0.01	0.01
Curie temperature (°C)	340	300	210	155	166
Coupling coefficient (k_{33})	0.73	0.64	0.79	0.92	0.94
Piezoelectric coefficient (d_{33},pC/N)	400	225	690	2200	2200
Applications	Accelerometer, Actuators, Flow meters, Hydrophones	Sonar projectors, Cleaners, Therapeutic, Ultrasound	Medical imaging, Transducers, Actuators, Hydrophones	Medical imaging, Actuators, Sonar, Accelerometers	Medical imaging, Actuators, Sonar, Accelerometers

[a] <001> oriented crystals.
*see Appendix I for descriptions.

There are several issues regarding the commercial applications of single crystals [1]. One of them is the low Curie temperature (T_C < 170 °C) of PMN–PT and PZN–PT (see Table 1.1), which will limit the acoustic power of devices, the temperature range of operation, and device fabrication processing. Moreover, materials with low T_C are not stable due to possible depolarization, which will degrade the performance of piezoelectric devices. High temperature stability is necessary for applications in many areas like high temperature electromechanical sensors and actuators used in automotives. To solve these issues, active studies have been pursued on several compounds with higher T_C. Piezoelectric single crystals of (1-x)Pb(Yb$_{1/2}$Nb$_{1/2}$)O$_3$ – xPbTiO$_3$ solid solution were grown using a flux technique and the electromechanical properties reported by Zhang *et al.* [64]. The Curie temperature of the grown crystals lies in range of 300–400 °C. The piezoelectric coefficients d_{33} are high and reach approximately 2500 pC/N for <001>-oriented PYN–46%PT single crystals.

The system of (1-x)BiScO$_3$ – xPbTiO$_3$ with MPB compositions was synthesized in the form of ceramics with a Curie temperature of 430 °C and d_{33} of 450 pC/N at a composition of x = 0.64 [65]. The (1-x)BiScO$_3$ – xPbTiO$_3$ single crystals were grown using a flux method. The Curie temperature of rhombohedral crystals was found to be about 404 °C, with a rhombohedral-tetragonal phase transition temperature around 350 °C [66]. Single crystals of (1-x)Pb(In$_{1/2}$Nb$_{1/2}$)O$_3$ – xPbTiO$_3$ and their electromechanical properties were also reported with a T_C around 320 °C and d_{33} of 400 pC/N [67].

Despite the above encouraging results, continued research on other new MPB systems of high-T_C piezoelectric materials in the form of ceramics and single crystals constitutes an important area of investigation for the future development of high-temperature transducers operating at temperature above 200 °C.

1.6 Objectives of This Work

Great opportunities for the development of new piezoelectric materials have emerged from the investigation of other perovskite systems that show the existence of a MPB, and a Curie temperature T_C >200 °C. The solid solution of (1-x)Pb($Sc_{1/2}Nb_{1/2}$)O_3 – $x$$PbTiO_3$ is found to be a good system to study.

(1-x)Pb($Sc_{1/2}Nb_{1/2}$)O_3 – $x$$PbTiO_3$ forms a solid solution between the relaxor Pb($Sc_{1/2}Nb_{1/2}$)O_3 and the normal ferroelectric $PbTiO_3$. Pb($Sc_{1/2}Nb_{1/2}$)O_3 (PSN) was first synthesized in the ceramic form by Smolenskii *et al.* [68]. This compound has the perovskite structure and its Curie temperature is T_C = 90 °C. Single crystals of PSN were grown using the flux method with PbO or PbO – B_2O_3 as flux [69, 70]. The study of the (1-x)Pb($Sc_{1/2}Nb_{1/2}$)O_3 – $x$$PbTiO_3$ binary system was first reported by Tennery *et al.* in 1968 [71] based on the experiments on ceramic specimens. Very high peak values of dielectric constant (about 26,000) with the peak value of loss in the order of 0.05 to 0.08, were observed at x = 0.20. The rhombohedral symmetry was assigned for the composition $x < 0.425$, and tetragonal for $x > 0.45$ at room temperature. In the range of $0.425 \le x \le 0.45$, a mixture of rhombohedral and tetragonal phases was proposed. The piezoelectric radial coupling coefficient (k_p) was studied as a function of x and the maximum value of $k_p = 0.46$ was observed with $x = 0.425$, which falls into the region of two phase coexistence. A preliminary phase diagram was established by means of dielectric measurements and a two-phase region corresponding to the composition around $x = 0.425$ with Curie temperature around 260 °C was roughly sketched (Figure 1.10).

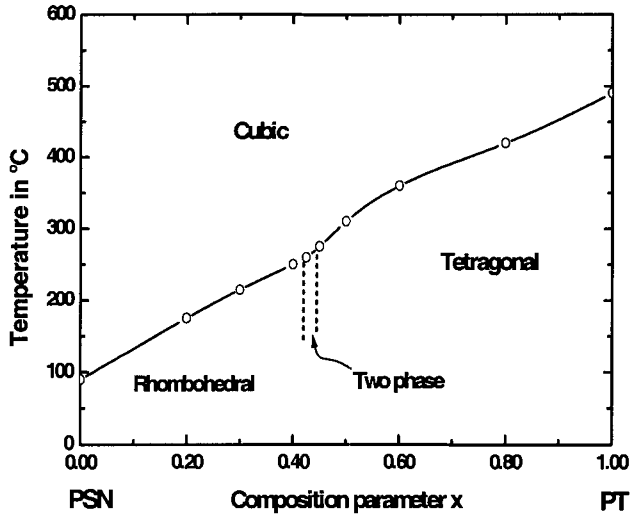

Figure 1.10:Temperature vs. composition phase diagram for the (1-x)Pb($Sc_{1/2}Nb_{1/2}$)O_3 – xPbTiO$_3$ system (after Tennery [71])

After Tennery's work, few studies were carried out on the (1-x)Pb($Sc_{1/2}Nb_{1/2}$)O_3 – xPbTiO$_3$ compounds. Recently, Yamashita [72] reported the large electromechanical coupling factors of k_p = 71%, k_{33} = 77%, and piezoelectric coefficient d_{33} = 450 pC/N for the PSN – xPT ceramics and Nb-doped PSN – PT ceramics with x = 0.43. Later, Yamashita and co-workers reported the crystal growth and electrical properties of (1–x)Pb($Sc_{1/2}Nb_{1/2}$)O_3 – xPbTiO$_3$ single crystals by a flux method using PbO–B_2O_3 [73, 74]. The grown crystals were 2-15 mm in size. The chemical analysis revealed that the composition of the crystals is in the range of 0.33 to 0.35, which is slightly different from the initially weighed MPB composition of x = 0.42. The <001>-oriented crystal showed a dielectric constant peak of 60,000 at T_C = 206 °C, the remnant polarization P_r = 26 μC/cm^2, a coercive field E_C = 6 kV/cm and k_{33} = 72%.

However, difficulties are still encountered in the growth of PSN–PT crystals because of the very high melting point, $T_m > 1425$ °C [75], of the solid solution system. The problems that arise from the growth and the factors that affect the quality of crystals have not been understood thoroughly. Consequently, the dielectric and piezoelectric properties of the PSN–PT crystals have not been fully studied and exploited due to the poor quality and significant composition fluctuations of the previously grown PSN–PT crystals [73].

1. The MPB region of the $(1\text{-}x)Pb(Sc_{1/2}Nb_{1/2})O_3 - xPbTiO_3$ system is not yet clearly defined. The preliminary phase diagram of PSN-PT in Figure 1.10 only sketched the region of the two-phase coexistence. For the solid solution system containing PT, a morphotropic phase boundary has been found in the PZT system [34, 36] and then in the PZN–PT [44, 76] and PMN–PT systems [52, 55, 77,]. It is expected that the phase diagram of PSN–PT system should show similar features, with the presence of a MPB region with a curved upper boundary. In addition, the complexity of the phase components and the presence of low symmetry phase(s) in the MPB region are also expected. Therefore, the first parts our work (**Chapter 3**) are to investigate the MPB behaviour of the $(1\text{-}x)Pb(Sc_{1/2}Nb_{1/2})O_3 - xPbTiO_3$ system. The ceramics of the solid solution system are synthesized by an improved two step precursor method and the properties of the materials were studied by means of dielectric permittivity, differential scanning calorimetry (DSC) and X-ray analysis, leading to establishment of the phase diagram of $(1\text{-}x)Pb(Sc_{1/2}Nb_{1/2})O_3 - xPbTiO_3$ and delimiting the MPB region.

2. Due to the highly refractory character of PSN–PT (with a melting point > 1425 °C), difficulties are encountered in the growth of $(1\text{-}x)\mathrm{Pb(Sc_{1/2}Nb_{1/2})O_3} - x\mathrm{PbTiO_3}$ crystals with compositions within the MPB region. In order to promote the PSN–PT single crystals for piezoelectric device application, it is necessary to optimize the growth with high quality crystals. The second part of our work (**Chapter 4**) describes the study of the effects of chemical parameters of the crystal growth and the optimization of growth conditions for the $(1\text{-}x)\mathrm{Pb(Sc_{1/2}Nb_{1/2})O_3} - x\mathrm{PbTiO_3}$ crystals.

3. The study of Chu *et al.* [78] on the disordered $\mathrm{Pb(Sc_{1/2}Nb_{1/2})O_3}$ ceramics by permittivity measurements demonstrates that upon cooling, a spontaneous (zero-field) transformation from a relaxor state to a ferroelectric state takes place when the lead vacancies are suppressed. This behaviour is different from that of other relaxors like PMN and PZN, in which such a transition can be observed in their dielectric properties only under an electric field. The typical relaxor behavior, which displays a broadened dielectric peak with frequency dispersion down to low temperature, can be only observed when introducing Pb-vacancies with a certain amount in the disordered $\mathrm{Pb(Sc_{1/2}Nb_{1/2})O_3}$ ceramics. On the other hand, the development of ferroelectric ordering in PMN-PT solid solution was studied by Ye *et al.* [79]. It is revealed that the substitution of $\mathrm{Ti^{4+}}$ ion at a concentration as low as 5% for the complex B-site $\mathrm{(Mg_{1/2}Nb_{2/3})^{4+}}$ ions results in the development of a rhombohedral phase. Since, the spontaneous relaxor to ferroelectric transition in $\mathrm{Pb(Sc_{1/2}Nb_{1/2})O_3}$ was only reported in the ceramic (probably due to the lack of high quality PSN single crystals), it is of interest to investigate the ferroelectric ordering and phase transition both in disordered $\mathrm{Pb(Sc_{1/2}Nb_{1/2})O_3}$ single crystals (**Chapter 5**) and in

$(1-x)Pb(Sc_{1/2}Nb_{1/2})O_3$ – $xPbTiO_3$ single crystals (**Chapter 6**). The formation of macrodomain states in these crystals is related to the effect of Pb-vacancies and presence of the Ti-content.

Another interesting solid solution which has been studied in this work is $(1-x)PbSnO_3 - xPbTiO_3$ system to exhibit high T_C and the MPB behaviour. The study of the effect of isovalent substitutions on crystal structure and transition temperature of ceramic $BaTiO_3$ [6] revealed that the Zr^{4+} and Sn^{4+} substitution for Ti^{4+} results in the decrease of the Curie temperature but the temperature for tetragonal-rhombohedral transition increases. It is expected that the same effects can apply to the $PbTiO_3$–containing solid solution, and the Zr^{4+} substitution for Ti^{4+} in $(1-x)PbZrO_3-xPbTiO_3$ (PZT) system indeed reflects these effects (see Figure 1.7).

Early studies of the $(1-x)PbSnO_3 - xPbTiO_3$ (PbSnTi) solid solution in the form of ceramics were carried out by Nomura *et al.* [80], Smolenskii *et al.* [81] and Jaffe *et al.* [82]. A preliminary phase diagram reported by Jaffe *et al.* suggested a possible boundary around x = 0.50, separating the ferroelectric tetragonal phase and another phase of unknown symmetry (Figure 1.11). The dielectric measurements reported in Ref. [81] showed an enhanced dielectric constant occurring at $x = 0.50$ with $T_C \approx 290$ °C, which is much higher than the T_C of PMN-33%PT (166 °C) and PZN-4.5%PT (155 °C) with compositions around the MPB.

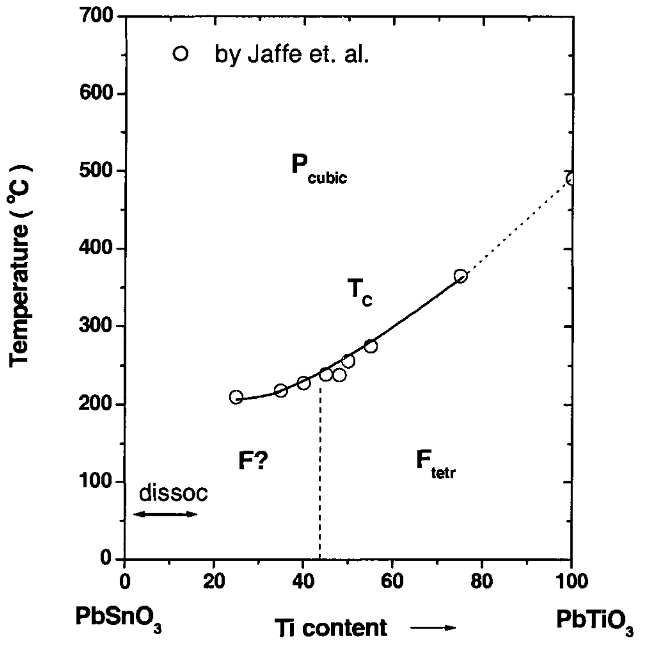

Figure 1.11:A preliminary phase diagram of (1-x)PbSnO$_3$ – xPbTiO$_3$ system. Curie temperature as function of Ti-content for the (1-x)PbSnO$_3$ – xPbTiO$_3$ system (after Jaffe (Ref. [82]).

As mentioned above, the piezoelectric properties are strongly correlated with crystal orientation. The study of the dependence of piezoelectric response on crystal orientation carried out on several complex relaxor ferroelectric crystals, such as PMN–PT, PZN–PT system, has led to the optimization of the crystal performance by domain engineering. It is expected that the (1-x)PbSnO$_3$ – xPbTiO$_3$ system shares some common features both in crystal chemistry and physical properties, with the PZT system. However, it has been known that it is extremely difficult to grow PZT single crystals. The development of the PbSnTi single crystals could provide a new piezocrystal resource. To the best of our knowledge, no PbSnTi single crystals have been grown and no properties have been reported so far. Therefore, it is of relevance to study the (1-x)PbSnO$_3$–xPbTiO$_3$

solid solution system in the form of single crystals in order to provide more insight and understanding of the mechanisms of piezoelectric properties. Our goal in this area (**Chapter 7**) is to study the growth and characterization of the $(1-x)PbSnO_3-xPbTiO_3$ single crystals with compositions close to the MPB.

In addition to above topics, the $Pb(Zn_{1/3}Nb_{2/3})O_3$ (PZN) crystal, another prototypical relaxor ferroelectric, is also investigated in terms of structure and dielectric properties by means of high-resolution synchrotron X-ray diffraction and dielectric spectroscopy (**Chapter 8**).

Finally, **Chapter 9** gives a brief general discussion and conclusions relating to this work. In this chapter, the relaxor phase transition behaviour of $Pb(Mg_{1/3}Nb_{2/3})O_3$, $Pb(Zn_{1/3}Nb_{2/3})O_3$, and $Pb(Sc_{1/2}Nb_{1/2})O_3$ are compared and discussed within the framework of the present models of relaxors.

Chapter 2:
Measurements and Characterization:
Principles and Techniques

2.1 Introduction

In this chapter, we describe the various basic experimental methods and principles applied in this thesis work. The measurements and characterizations of studied materials are related to phase analysis by X-ray diffraction, dielectric permittivity, piezoelectric, ferroelectric, thermal analysis by differential scanning calorimetry, and domain observations by polarized light microscopy. We shall try to give a brief introduction to the ideas and concepts of these experimental methods together with the related original reference.

2.2 X-ray Powder Diffraction (XRD)

2.2.1 X-ray Sources [83].

X-rays lie in the electromagnetic spectrum between ultraviolet light and gamma radiation and have wavelengths which range from 0.1 to 100Å. They are usually produced by rapidly decelerating fast-moving electrons to convert their kinetic energy motion into a quantum of radiation. To generate X-rays, electrons are accelerated by an electric field and directed against a metal target, which slows them rapidly by multiple collisions. Under the usual conditions most of the electrons are not brought to a full stop by a single collision, and a continuum of radiation is formed.

X-ray spectra are characterized by the element of which the target is made. When the electrons bombarding the target reach certain critical energies (threshold potentials) they are capable of knocking electrons out of their atomic orbitals. In particular, at energies of about 10,000 eV (for elements with atomic number ~30) they can remove electrons from the innermost (K) shell. The vacancy in the K shell is then filled by the descent of an electron from the next higher shell (L) or the one above that (M). The decrease in potential energy in going from the higher level to the lower appears as radiation, and as the energies of the shells are well defined, each transition gives a nearly monochromatic line. The principal peaks are:

$K_{\alpha 1}$, $K_{\alpha 2}$: $L \rightarrow K$

$K_{\beta 1}$, $K_{\beta 2}$: $M \rightarrow K$

Because the difference in energy between L and K is less than that between M and K, K_α is always at a longer wavelength than K_β. The lines are close doublets because transitions can occur from two possible electronic configurations, which differ slightly in energy. $K_{\alpha 1}$ is twice as intense as $K_{\alpha 2}$ and about three to six times as strong as $K_{\beta 1}$. $K_{\beta 2}$ is usually so weak that it is ignored.

Copper K_α is the conventional choice for use with crystals. The wavelength of Cu Kα, 1.5418 Å is used in our work (Philips). (1.5418 Å is the intensity-weighted average of α_1 and α_2 and is the figure usually used for the wavelength when the two lines are not resolved).

The giant particle accelerators are a great X-ray source in addition to a conventional characteristic one. Electrons or positrons are injected into a very large evacuated loop and kept circulating at relativistic velocities by energy pumped in from powerful radio-frequency sources. To constrain the circulating particles to the chamber, external magnets, often superconducting, provide an inward acceleration. A consequence of this acceleration is the emission of synchrotron radiation. This radiation is a broad-spectrum (white) emission that resembles the white radiation of an X-ray tube but is immensely more intense (100 to 10^4 times the intensity of a conventional characteristic line). The particular designs for radiation production contain additional devices (wigglers and undulators) to cause additional bending of the particle beam at locations that optimize the radiation generation. Wigglers cause sharper than usual bends in the particle current (and then a reverse bend so that there is no net deviation), leading to a shift of the radiation to shorter wavelengths and increasing the intensity in the range of interest. Undulators create a series of small deviations such that the emissions produced at each turn are subject to interference with radiation from all the other turns. This results in an approximately monochromatic radiation source with vastly enhanced intensity (as much as 10^4) at the selected wavelengths.

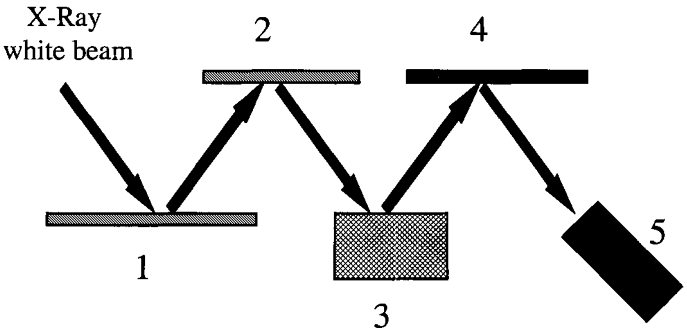

1 and 2: Ge(111) double-crystal monochromator
3: sample holder
4: Ge(220) crystal analyzer
5: scintillation detector.

Figure 2.1: The setup of synchrotron beam line facility for X-ray powder diffraction.

Synchrotron radiation is used to detect the complex and small structure changes in many materials, especially, the symmetry of phase in the morphotropic phase boundary (MPB) in the ferroelectric solid solution systems. The synchrotron radiation experiments in this work have been performed at Brookhaven National Laboratory, and in collaboration with Dr. B. Noheda and Dr. G. Shirane.

The desired wavelength in synchrotron experiments is usually selected by crystal monochromators. In Figure 2.1, an incident beam of the certain wavelength is obtained from a Ge(111) double-crystal monochromators. The diffraction beam from the sample is first passed a Ge(220) crystal as analyzer and then detected by the scintillation detector. The resulted instrumental resolution is about 0.01 ° on the 2θ scale [35].

2.2.2 X-ray Diffraction

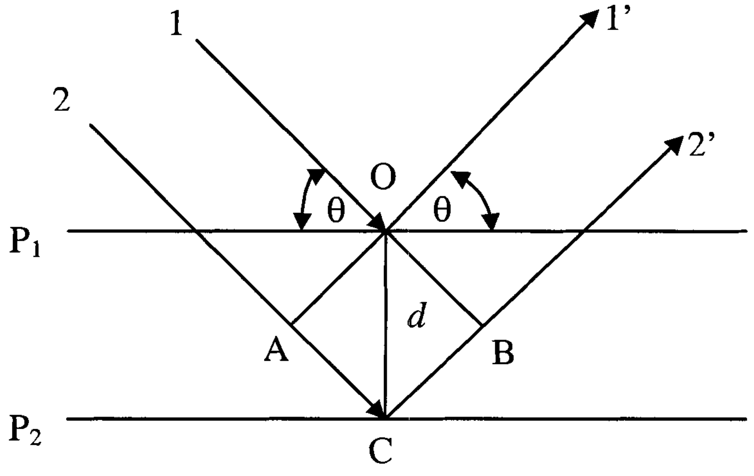

Figure 2.2: Construction showing condition for diffraction.

The diffraction of X-ray by crystals was discovered by von Laue in 1912. Following the experimental observation of X-ray diffraction, von Laue showed that the phenomenon could be described in terms of diffraction from a three-dimensional grating.

In the same year, while engaged in experimental studies, W. L. Bragg noticed the similarity of diffraction to ordinary reflection and deduced a simple equation treating diffraction as "reflection" from planes in the crystal lattice, i.e. the Bragg law:

$$2d\sin\theta = n\lambda \quad , \tag{2.1}$$

where d is the interplanar spacing between P_1 and P_2. θ is the angle between the incident rays and the planes P_1 or P_2. n is an integer number and λ is wavelength of X-rays (Figure 2.2).

The process of reflection is described above in terms of incident and reflected rays each making an angle θ with a fixed crystal plane. It can also be viewed as involving a fixed incident beam, in which case reflection occurs from planes set at the angle θ with respect to the beam and generates a reflected ray deviating through 2θ. This is more commonly used in actual experimental arrangements.

X-ray diffraction has been extensively used in this work, both for monitoring the purity of phases after chemical reactions and for determining the crystal symmetry of the phase in the region of MPB of the solid systems studied. The former application is based on the "fingerprint" feature of the X-ray spectrum. The principles for the latter application are explained as follows, which are used to describe the structure refinement by different functions.

2.2.3 Principles Used for Determining the Crystal Symmetry

There are seven three-dimensional coordinate systems that describe all the crystal structures and form the basis for their classification. In general, the unit cell is characterized by six parameters, three axial lengths and three interaxial angles (Figure

2.3). The length of the unit cell edges are designated *a*, *b*, *c*, and the interaxial angles α, β, and γ.

The observed X-ray diffraction pattern is related to the crystal symmetry. When a crystal structure undergoes a symmetry transition, the lattice parameters change. Accordingly, the X-ray diffraction pattern also changes. For example, when the crystal structure changes from cubic to tetragonal, the interaxial angle is kept the same, however, the lengths of the unit cell (*a, b, c*) are no longer all equal but a = b ≠ c (Figure 2.4).

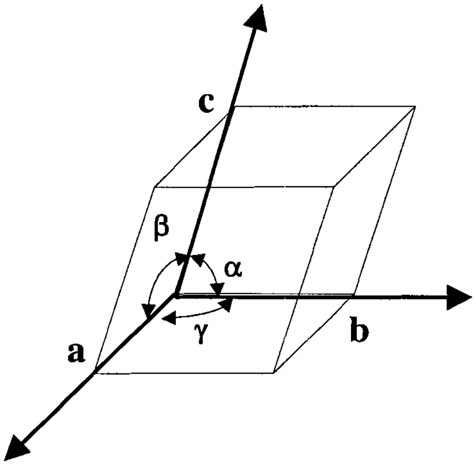

Figure 2.3: Parameters describing a unit cell.

As a result, the (100) reflection peak in the cubic phase, which is indistinguishable from the (010) and (001) reflections, will split into two peaks in the tetragonal phase so that one corresponds to the (001) reflection and the second (100) and (010) reflection. Figure 2.5 shows the splitting of the cubic (111), (200) and (220) reflection peaks when the crystal undergoes transition into a respective lower symmetry phase. Each vertical line represents the peak position with the relative intensity ratio. In the tetragonal phase, if we suppose the lengths of unit cell edge: $a = b > c$, the (001) reflection occurs at lower angle with the relative intensity ratio, i.e. the intensity of the

(001) peak over the sum of the intensity from the (100) and (010) reflections of about 1:2. The same consideration can also apply to the cubic (220) reflections.

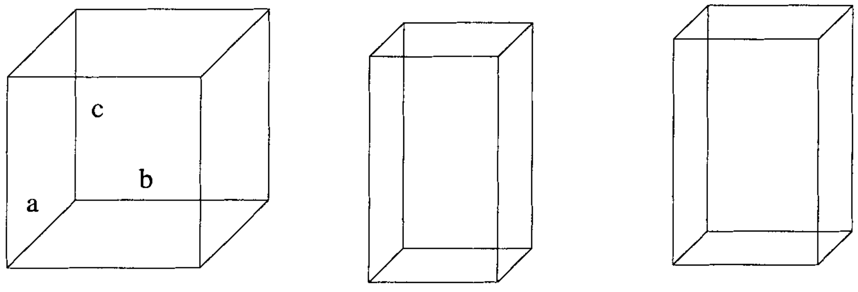

Cubic: a =b = c,
$\alpha = \beta = \gamma = 90°$

Tetragonal:
a =b ≠ c,
$\alpha = \beta = \gamma = 90°$

Orthorhombic:
a ≠ b ≠ c,
$\alpha = \beta = \gamma = 90°$

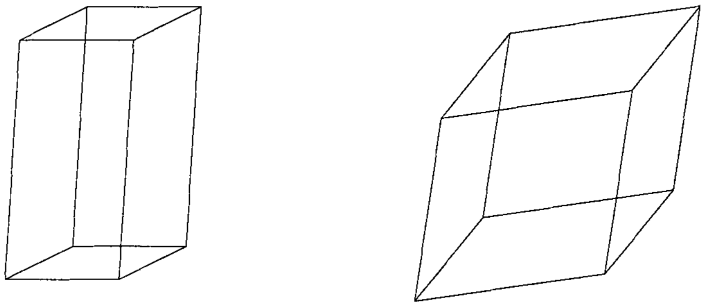

Monoclinic:
a ≠ b ≠ c,
$\alpha = \gamma = 90° \neq \beta$

Rhombohedral:
a =b = c,
$\alpha = \beta = \gamma \neq 90°$

Figure 2.4: Primitive cubic, tetragonal, orthorhombic, monoclinic and rhombohedral lattice, each showing the symmetry – lowering from the prototype-cubic symmetry for comparison.

For the cubic (111) reflection, because all the (111) reflections in the tetragonal phase are identical (the same as in the cubic phase), the tetragonal (111) reflections are all superimposed into one peak profile, as shown in Figure 2.5(b).

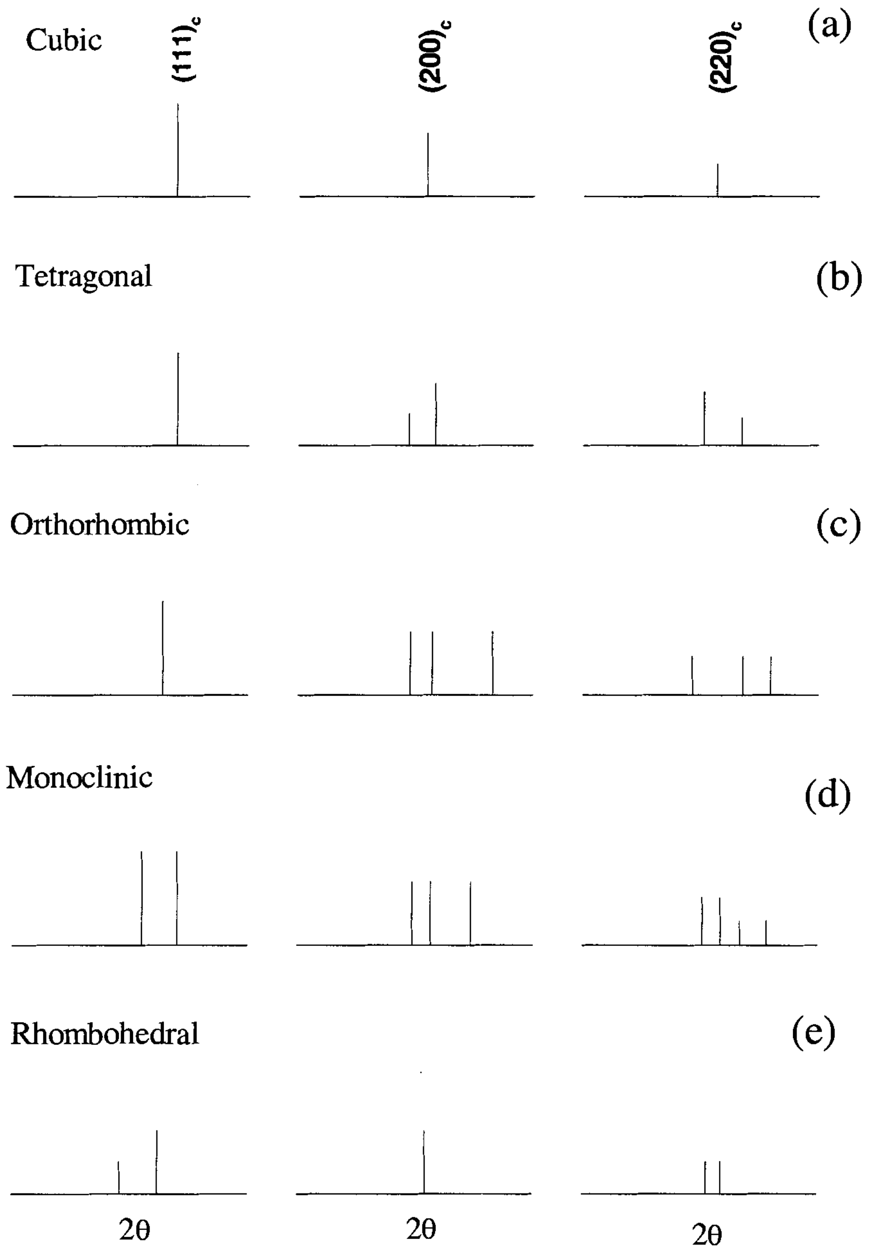

Figure 2.5: Characteristic X-ray diffraction pattern for the Cubic (prototype), Tetragonal, Orthorhombic, Monoclinic and Rhombohedral symmetry, showing the corresponding splitting with regard to the cubic (111), (200) and (220) reflections.

2.3 Measurements of Dielectric Permittivity

In this work, the dielectric permittivity as a function of temperature at various frequencies is measured by means of either an Alpha high-resolution dielectric/impedance analyzer (NovoControl) or a Solartron 1260 impedance analyzer combined with a Solartron 1296 dielectric interface. When an alternating electromotive force Φ with frequency f is applied to the electrodes of a parallel capacitor structure, an alternating current of magnitude, i, flows that follow equation [4]:

$$i = jf\varepsilon_r C_0 \Phi \qquad , \qquad (2.2)$$

where $j = \sqrt{-1}$; $C_0 = \varepsilon_0 S/d$ is the vacuum capacitance of the space cell with electrode area, S, and separation distance, d; $\varepsilon_0 = 8.854\text{x}10^{-14}$ F/cm is the permittivity of free space; ε_r is the relative dielectric constant. Because the dielectric loss (including the leakage current) exists in dielectric materials, ε_r must be written as a complex number:

$$\varepsilon_r^*(f) = \varepsilon'(f) - j\varepsilon''(f) \qquad , \qquad (2.3)$$

where ε' is the real part of the dielectric permittivity (commonly called dielectric constant) and ε'' is the imaginary part of the dielectric permittivity. The latter ε'' represents the dielectric loss. Most frequently used by engineers to express this loss is $\tan\delta$ (tangent of the dielectric loss angle) that is defined as:

$$\tan \delta = \varepsilon''/\varepsilon' \qquad (2.4)$$

2.4 Determination of Piezoelectric Constants and Electromechanical Coupling Factors

In our work, the piezoelectric resonance measurements are carried out to determine the piezoelectric constants and electromechanical coupling factors, using a Solartron 1260 impedance analyzer combined with a Solartron 1296 dielectric interface. The vibration of the piezoelectric sample is achieved by a small a.c. field [4], exciting a vibrational state with a frequency near its intrinsic resonance frequency. The resonance frequency is the frequency at which the sample element vibrates most readily, and most efficiently converts the electric energy input into mechanical energy [84]. A resonance frequency (f_r) (approximately the same as the frequency at which the impedance is minimum) and an antiresonance frequency (f_a) (approximately the same as the frequency at which the impedance is maximum) are measured. In general, a specific resonance mode may be excited by applying a variable frequency a.c. field to a piezoelectric sample of a specific shape and a specific polarization orientation. For example, for the measurement of the piezoelectric constant d_{33} and the longitudinal coupling factor k_{33}, an a.c. field is applied in the c-axis direction of a c-bar (i.e., a bar with length l along the c-axis direction), and from the frequencies f_r and f_a of vibrations in the longitudinal length expansion mode, s^E_{33}, s^D_{33}, k_{33} and d_{33} (see Appendix II for descriptions) can be derived by the following equations [85, 86]:

$$k^2_{33} = \frac{\pi}{2}\frac{f_r}{f_a}\cot\left(\frac{\pi}{2}\frac{f_r}{f_a}\right) \quad , \tag{2.5}$$

and

$$s^D_{33} = \frac{1}{4\rho(lf_a)^2} \quad , \tag{2.6}$$

$$s_{33}^{E}=\frac{s_{33}^{D}}{1-k_{33}^{2}} \quad , \tag{2.7}$$

$$d_{33}^{2}=k_{33}^{2}\varepsilon_{33}^{T}s_{33}^{E} \quad , \tag{2.8}$$

where l is the length (in meter) of the crystal rod, ρ is the density (in Kilogram/cubic meter) of material, and ε_{33}^{T} is the dielectric permittivity measured at a frequency f far below the sample's piezoelectric resonance frequency [4].

2.5 Thermal Analysis by Differential Scanning Calorimetry (DSC)

To investigate the phase transition of the materials synthesized, the temperature dependences of heat flow were measured on a differential scanning calorimeter (DSC6200, Seiko Exstar,). Samples of 60 to 80 mg each obtained from crushing ceramics or single crystals were used as specimens. The heating and cooling rate was at 10 °C/min. α-Alumina powder was used as reference.

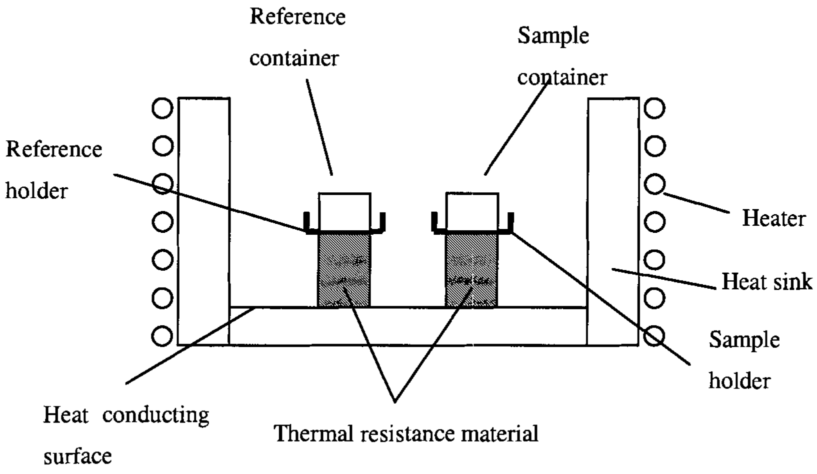

Figure 2.6: DSC Measurement setup.

Both the specimen and the reference were loaded in the separated alumina pans, and placed on top of the sample or reference holder, respectively, in a high heat conductance sink (Figure 2.6). The heater via commands from the temperature program accurately controlled the temperature of the high heat conductance sink. The heat flow is conducted from the heat conducting surface through the thermal resistance materials into the sample and reference holders and containers. Any increase or decrease of the temperature of the sample and reference will be monitored by the change in the heat flow.

The heat flow passing through the thermal resistance materials is proportional to the temperature difference between the heat conducting surface on one end and the sample holder on the other end. The specially designed heat sink is accurately controlled to maintain a uniform temperature at the heat conducting surface. Therefore, the measured difference in heat flow through the sample holder and reference holder is proportional to the sample and reference temperature differences. In this way, a heat flux type DSC detects the temperature difference signal and outputs it as a DSC signal. Such a temperature difference indicates, in our work, a phase transition taking place in the sample.

2.6 Ferroelectric Hysteresis Loop

The ferroelectric properties are characterized by the measurements of polarization as a function of electric field using an RT66A standard ferroelectric testing system (Radiant Tech.). A ferroelectric hysteresis loop can be observed by means of a Sawyer – Tower circuit [87]. Figure 2.7 shows a modified Sawyer – Tower circuit [88, 5]. An alternating voltage V is imposed across a pair of electrodes on the surfaces of a sample (as one capacitor C_x with thickness of d). Thus, the quantity plotted on the horizontal axis is proportional to the field ($E = V/d$) across the sample. A RC circuit is connected in series with the sample C_x. The parallel RC circuit allows compensation for any phase shift due to conductivity or dielectric loss in the sample. The voltage V_r across C_r is therefore proportional to the charge (Q) of the sample C_x by $V_r = Q/C_r = (A/C_r)P \propto P$ (A is the electrode area of the sample, P is the polarization of sample). This voltage is monitored by the vertical plates of the scope. To keep the consistency of characterization, the same sample used for the permittivity measurement was employed in the measurement of ferroelectric hysteresis loop.

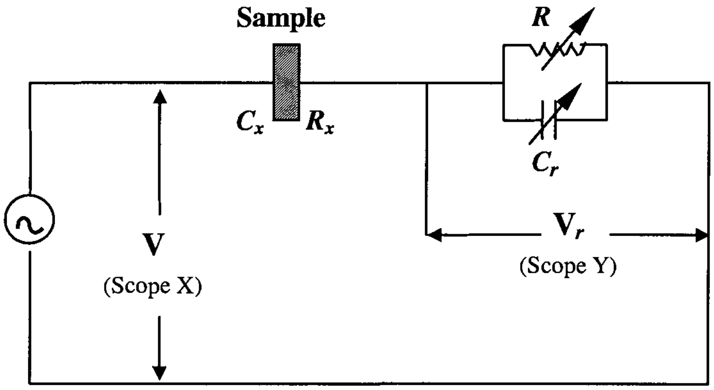

Figure 2.7: A modified Sawyer-Tower circuit used for measurement of ferroelectric hysteresis loops (after Sinha [88, 5]).

2.7 Strain – Electric Field Loop

The strain vs. electric field is measured by an MTI-2000 Fotonic Sensor (Mech. Tech. Inc). The MIT-2000 Fotonic probe modules contain two sets of optical fibers [89]. Light-transmitting fibers and light-receiving fibers are bundled together as shown in Figure 2.8(a). The displacement measurement is based on the interaction between the field of illumination of the transmitting fibers and the field of view of the receiving fibers. The platelet sample with electrode on both sides is connected into an external voltage source. The distance between the sample and the Fotonic probe is controlled by a screw device.

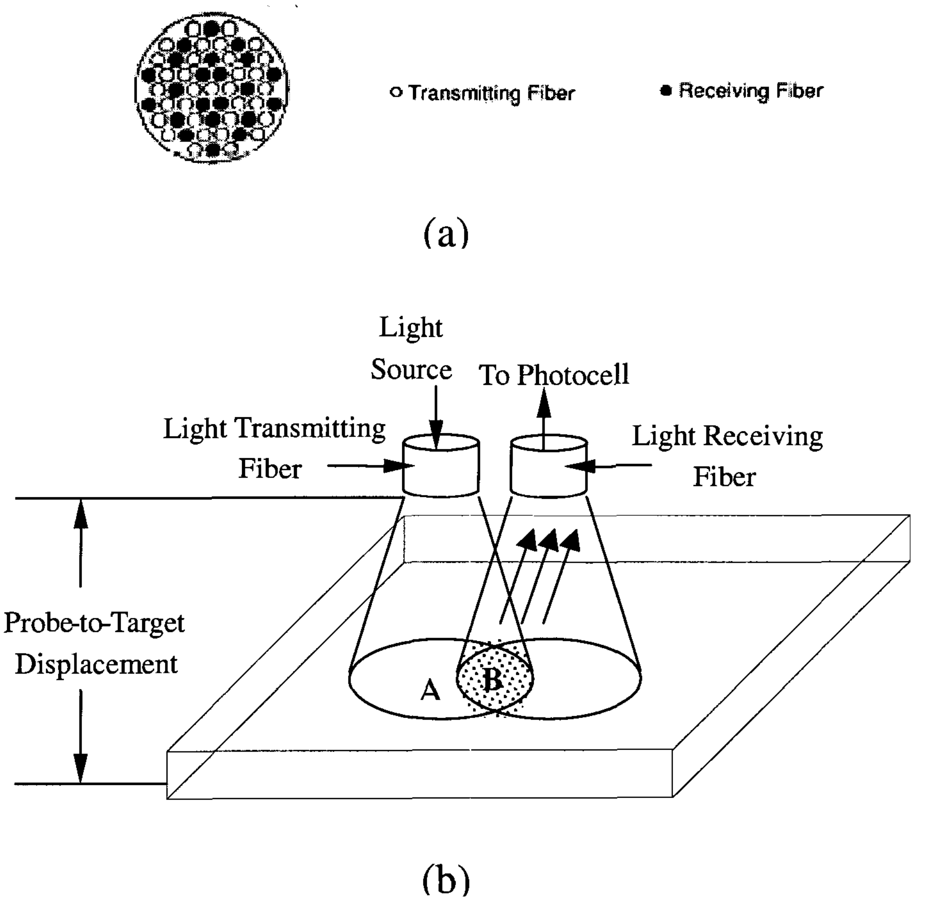

Figure 2.8: A setup for measurements of the strain vs. electric field loop. (a) Fiber-optical probe tip configurations; (b) Displacement sensing mechanism of adjacent fiber-optical elements (Ref. [89]).

At contact, or zero gap, most of the light exiting the transmitting fibers is reflected directly back into those fibers. No light is provided to the receiving fibers and the output electric signal (in the voltage scale) is “zero”. As the probe to target distance increases by tuning the screw in one direction [Figure 2.8(b)], increasing amounts of the light are captured by the receiving fibers. This relationship will continue until the entire face of the receiving fibers is illuminated with reflected light. This point is called the “optical peak” and corresponds to the maximum voltage output of the electrical signal. Any further turning of the screw in the same direction will cause the diverging field of the reflected light to exceed the field of view of the receiving fiber, thus causing a reversal in the output-versus-distance signal relationship. Therefore, The point at "optical peak" is set as a maximum point. Before the measurement starts, the distance between the sample and the Fotonic probe is first reduced by screwing backwards to get away from the optical peak to the point that gives rise to the minimum intensity of received light, then the electric signal is applied. Any displacement of sample in response to the electric field will then be compared with the optical peak and gives the relationship of displacement versus electric field.

2.8 Polarized Light Microscopy (PLM)

2.8.1 Investigation of Ferroelectric Domain Structure and Phase Transitions Between Crossed Polarizers

Polarized light microscopy (PLM) (Olympus BX60) is employed for the study of the domain structures and phase transitions of ferroelectric single crystals. In order to observe the domain structures as a function of temperature, a heating and cooling stage (Linkam HTMS600) (temperature range between –180 °C to 600 °C) was used. The domain structure was observed by birefringence contrast microscopy. The birefringence contrast is caused by the intensity and colour differences [90], which can be obtained between crossed polarizers, due to different extinction directions of birefringent domains. The extinction direction is such a direction, in which the polarization direction of optical indicatrix is align or perpendicular to the direction of polarizer or analyzer and the output imaging is in the dark filed.

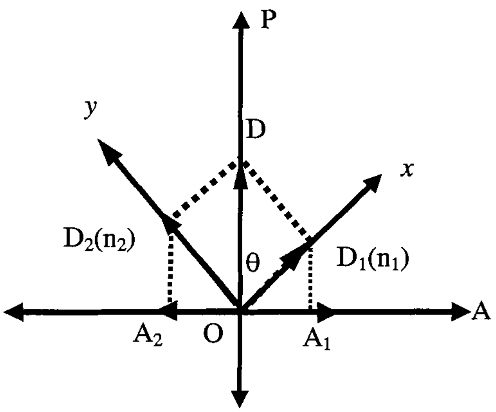

Figure 2.9: Configuration of linearly polarized light along the special directions of a crystal plate.

Consider a beam of linearly polarized light incident normally on a thin plate of a birefringent sample cut parallel to the optic axis, i.e. along optic axis the velocities of the ordinary ray and the extraordinary ray are equal [91]. The displacement vector D of the incident light (Figure 2.9) has an amplitude $a\cos\omega t$ and makes an angle θ with the optic axis x. Upon entering the crystal the displacement D breaks up into two components of amplitudes $D_1 = a\cos\theta\cos\omega t$ and $D_2 = a\sin\theta\cos\omega t$ in the directions Ox and Oy, respectively. After traversing the crystal plate of thickness d the two orthogonal components will be out of phase by an amount ϕ. The two components will then be:

$$D_1 = a\cos\theta\cos\omega t \quad , \tag{2.9}$$

and

$$D_2 = a\sin\theta\cos(\omega t + \phi) \tag{2.10}$$

After traversing the analyzer, the light has the components A_1 and A_2 (Figure 2.9). The light intensity for a birefringent sample after the analyzer can be expressed as [90]:

$$I = I_0 \sin^2 2\theta \bullet \sin^2 \phi/2 \quad , \tag{2.11}$$

ϕ can further be expressed as:

$$\phi = (2\pi / \lambda) \bullet d \bullet (n_2 - n_1) \quad , \qquad (2.12)$$

where λ is the light wavelength; d is the sample thickness; n_1 and n_2 represent the refractive indices for the D_1 and D_2 components, respectively. The maximum contrast between opposite domains is reached at $\phi = \pi/2$ for a fixed wavelength and extinction in one of the domains.

2.8.2 Crystal Optical Principle

For the samples considered in this thesis, the optical properties of the crystal are anisotropic and are related to the crystal symmetry. For example, for complex perovskite samples, in the tetragonal 4mm phase, the intrinsic spontaneous polarization is along one of the six equivalent <001> directions and the optical axes are also oriented parallel to <001>. In the rhombohedral *R3m* phase, the intrinsic polarization is along one of the eight equivalent <111> directions and the optical axes are also oriented parallel to the <111> direction. When the domain observations by polarized light microscope are taken on (001) oriented crystal plates, the cross section of the optical indicatrix, which is an sphere or ellipsoid surface defined by the indices of refraction, coupled to the crystallographic axes, will exhibit extinction directions parallel to <001> for the domains of tetragonal phase and along the <110> directions for the domains of rhombohedral phase [53]. The schematic presentations of these phenomena are shown in Figure 2.10.

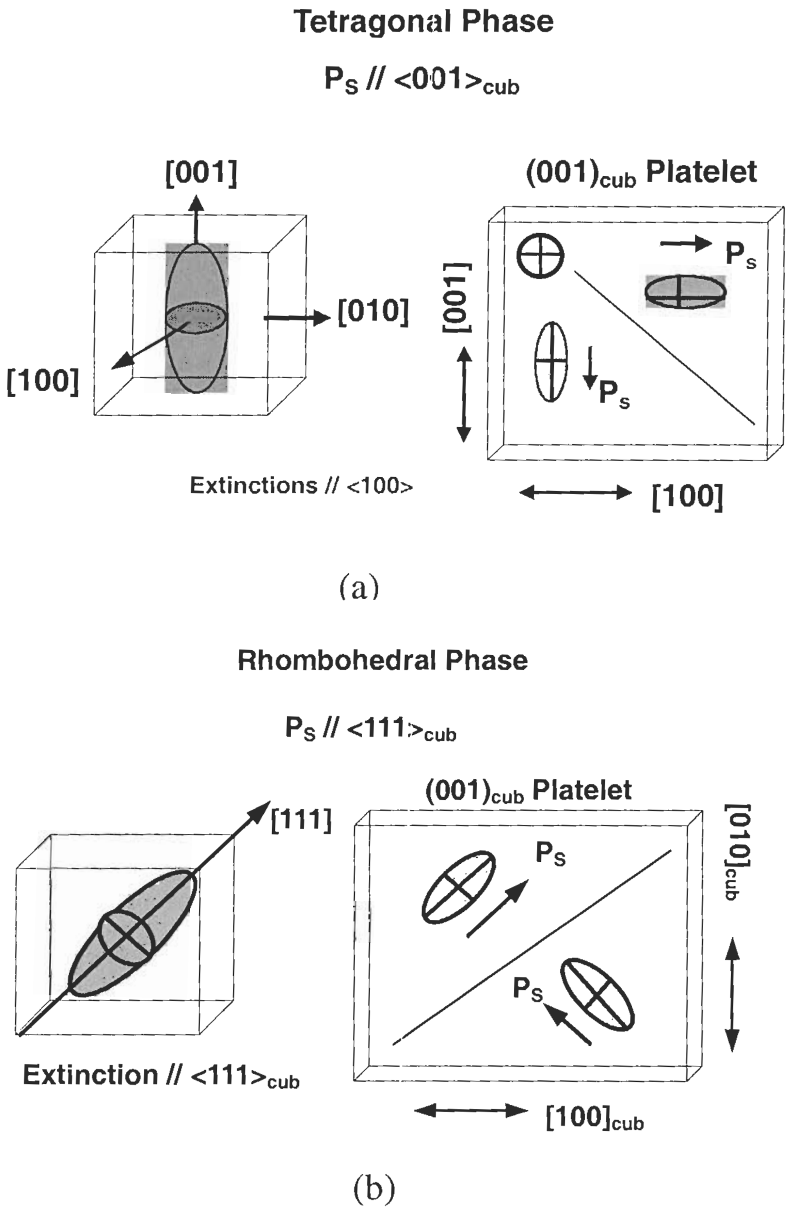

Figure 2.10: Schematic presentation of the domain structures
a): orientation and extinction directions of possible tetragonal domains;
b): orientation and extinction directions of possible rhombohedral domains
(P_S: spontaneous polarization in ferroelectric materials)

Chapter 3:
Synthesis, Structure and Properties of the $(1-x)Pb(Sc_{1/2}Nb_{1/2})O_3$-$xPbTiO_3$ Solid Solution Ceramics; Establishment of Morphotropic Phase Diagram

3.1 Abstract

In this chapter, we report the systematic study of the $(1-x)Pb(Sc_{1/2}Nb_{1/2})O_3$–$xPbTiO_3$ (PSN–PT) solid solution in the form of ceramics with compositions within the morphotropic phase boundary (MPB) region ($0.35 \leq x \leq 0.50$), in the aspects of synthesis, structure, and physical properties. The PSN-PT ceramics in this composition range have been synthesized by an improved two-step wolframite precursor method. The synthetic process has been optimized in terms of wet grinding, calcining, and sintering conditions. The complex phase behaviour of the PSN–PT solid solution system has been studied by means of dielectric spectroscopy and X-ray structural analysis. A new phase with monoclinic symmetry is found to be present. The morphotropic phase diagram has been established, providing a better understanding of the MPB behaviour. This information is useful for the preparation of these materials in high T_C piezoelectric applications.

3.2 Introduction

The term "Morphotropic phase boundary (MPB)" was first used by Jaffe *et al.* [34] to describe the separation of the rhombohedral and tetragonal phases in the phase diagram of the (1-x)$PbZrO_3$ – $x$$PbTiO_3$ (PZT) solid solution. Following this ground-breaking work, similar features have been found in many other solid solution systems, such as (1-x)$Pb(Mg_{1/3}Nb_{2/3})O_3$ – $x$$PbTiO_3$ (PMN-PT) [77], (1-x)$Pb(Zn_{1/3}Nb_{2/3})O_3$ – $x$$PbTiO_3$ (PZN-PT) [44] and (1-x)$Pb(Sc_{1/2}Nb_{1/2})O_3$ – $x$$PbTiO_3$ (PSN-PT) [71]. An interesting observation is that the outstanding dielectric and piezoelectric properties always occur in the compositions at or near the MPB, making them excellent materials for applications as capacitors, sensors, actuators and other high piezoelectric devices. Intensive studies have been undertaken on the understanding of the physics and chemistry of the MPB. One of the recent breakthroughs was the discovery of a monoclinic phase in the PZT system by Noheda *et al.* [35], which has opened new insights as to the phase components and structure of the MPB and provided a better understanding of the structural origin of the piezoelectric properties in the MPB region [92, 36]. Since then, a monoclinic or an orthorhombic phase has also been discovered in the PMN–PT [52, 57] and PZN–PT [93] systems.

On the other hand, the PSN–PT solid solution system has not been paid enough attention compared with the PMN–PT and PZN–PT systems which have been extensively investigated in the last few years. The basic features of the PSN-PT phase diagram were reported in the 1960's by Tennery *et al.* (Figure 1.10) [71]. The MPB was initially located around the composition of $x \approx 0.425$ and considered as a region of two-phase mixture. As we will see, the PSN-PT solid solution exhibits a higher Curie temperature, $T_C \approx 240–260$ °C (with compositions near the MPB), compared with that ($T_C < 170$ °C) of PMN–PT and PZN–PT systems. This advantage is important for applications in many areas that require a broad temperature range, such as high temperature electromechanical sensors and actuators used in automotives.

Since that initial report [71], only a few studies have been carried out on the PSN–PT solid solution. Yamashita [72, 94] reported the growth of PSN–PT and Nb–doped PSN–PT ceramics with a dielectric maximum (ε_{max}) of 39,100 and electromechanical coupling factors of k_p = 71%, and k_{33} = 76% in the compositions around the MPB. The value of k_p is the largest found in any piezoceramics. Given the high piezoelectric performance of the PMN–PT [46] and PZN–PT single crystals, it was naturally thought that the single crystals of PSN–PT would be of great interest. Following the initial trial of the growth of the PSN–PT single crystals by Yamashita *et al.* [73], we have developed an improved flux growth technique, which leads to good quality PSN-PT crystals [95]. A dielectric maximum as high as 60,000 is obtained in the grown PSN-PT single crystals. The details of crystal growth and characterizations will be described in **Chapter 4**. Recently, Haumont *et al.* [96] proposed a modified PSN–PT phase diagram based on the analysis of X-ray and neutron diffraction data. In this phase diagram, the rhombohedral symmetry was confirmed as a ground state for $x \leq 0.26$, while the tetragonal symmetry was observed for $x \geq 0.55$. A new monoclinic phase was deduced for $x \approx 0.43$. However, no anomaly was found in their permittivity measurements as a function of temperature, which would be associated with the phase transition of the monoclinic phase. It is well known in the PMN–PT [45] and PZN–PT [44] systems that two anomalies were detected in the dielectric permittivity upon cooling, corresponding to two phase transitions. One is the transition from the paraelectric to the ferroelectric tetragonal phase at T_C, another is the transition from the tetragonal to the ferroelectric rhombohedral or monoclinic phase.

It has been noticed from the earlier studies [71, 94] that the dielectric and piezoelectric properties of the PSN-PT closely depend on the quality of the ceramics. The difficulties encountered so far in preparing high quality PSN–PT ceramics explain the inferior performance reported by most researchers. Moreover, the preparation of the pure perovskite phase of (1-x)PSN – xPT is crucial for the phase analysis and thereby for the determination of the MPB phase diagram. Therefore, it is rewarding to systematically study the synthesis of the PSN–PT ceramics in the first stage of this work.

In the following sections, we report the approaches for the synthesis of $(1-x)\mathrm{Pb(Sc_{1/2}Nb_{1/2})O_3} - x\mathrm{PbTiO_3}$ ceramics with compositions within the MPB region, i.e. x = 0.35, 0.37, 0.38, 0.39, 0.40, 0.41, 0.42 0.45 and 0.50, and the investigations of the structure and phase transitions of the (1-x)PSN–xPT ceramics by means of X-ray structural analysis, differential scanning calorimetry (DSC) and dielectric spectroscopy. A new phase with monoclinic symmetry has been found by X-ray phase analysis. A new phase diagram of the PSN-PT solid solution has been established within the MPB region having a curved upper boundary.

3.3 Approaches for the Synthesis of $(1-x)\mathrm{Pb(Sc_{1/2}Nb_{1/2})O_3} - x\mathrm{PbTiO_3}$ in the Form of Ceramics

3.3.1 Background

It has been known that the manufacturing procedures of piezoelectric ceramics greatly influence their properties. Piezoelectric ceramics are traditionally made from powders formulated from the individual oxides because this is the most economical process. However, in the processing of complex perovskite relaxors, such as $Pb(Sc_{1/2}Nb_{1/2})O_3$ (PSN), $Pb(Mg_{1/3}Nb_{2/3})O_3$ (PMN) and $Pb(Zn_{1/3}Nb_{2/3})O_3$ (PZN), by this conventional method, a stable pyrochlore phase often appears, accompanying the products of the perovskite phases and this is responsible for the degradation of the dielectric properties. The stability of the perovskite ABO_3 structure was studied by Shrout *et al.* [97] in terms of thermodynamics and was related to the tolerance factor and the electronegativity difference. Figure 3.1 displays the plot of the tolerance factor vs. electronegativity difference for selected perovskite compounds. The tolerance factor was calculated from the equation $t = (r_A + r_O)/\sqrt{2}(r_B + r_O)$ using the ionic radii of Shannon [98]. Pauling's [99] electronegativity scale was used for the calculation of the electronegativity differences. For many lead-based perovskite relaxors, such as PSN, PMN and PZN, the electronegativity differences are relatively small compared to the ideal perovskites compounds, for example $SrTiO_3$. Moreover, the tolerance factor is considerably smaller than one, suggesting that their perovskite structure is less stable than the ideal perovskites. Consequently, the preparation of the lead-based complex relaxors with pure perovskite phase has always been a challenge.

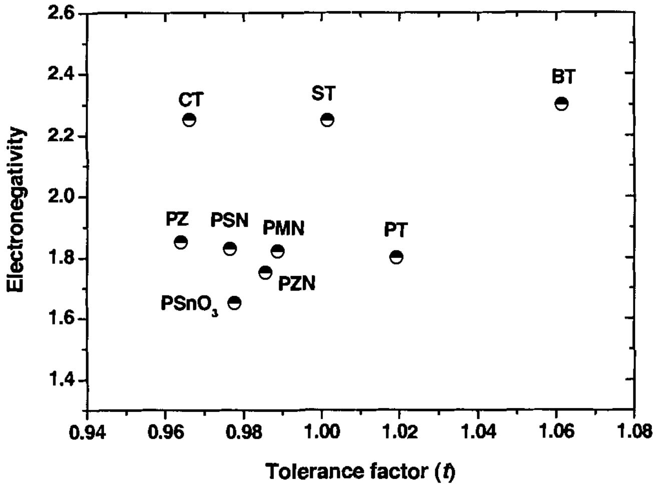

Figure 3.1: Plot of the tolerance factor vs. electronegativity differences for selected perovskite compounds
(CT: $CaTiO_3$; ST: $SrTiO_3$; BT: $BaTiO_3$; PZ: $PbZrO_3$; PT: $PbTiO_3$.) (after Shrout [97]).

The studies of the strategies for the fabrication of complex perovskite relaxors were carried out on several typical materials, such as PMN, PZN and PST. Inada first proposed the following reaction sequences for the preparation of PMN [100]:

$$3PbO + 2Nb_2O_5 \xrightarrow[\text{exo}]{530 \text{ to } 600^\circ\text{C}} > Pb_3Nb_4O_{13} \text{(anion – deficient, cubic pyrochlore)}, \qquad (3.1)$$

$$Pb_3Nb_4O_{13} + PbO \xrightarrow[\text{exo}]{600 \text{ to } 700^\circ\text{C}} > 2Pb_2Nb_2O_7 \text{(rhombohedral pyrochlore)}, \qquad (3.2)$$

$$Pb_2Nb_2O_7 + 1/3MgO \xrightarrow[\text{endo}]{700 \text{ to } 800^\circ\text{C}} > Pb(Mg_{1/3}Nb_{2/3})O_3 \text{ (perovskite)} + 1/3Pb_3Nb_4O_{13} \qquad (3.3)$$

As we can see, the formation of the perovskite PMN did not take place in one step from the oxides but by subsequent reactions with the pyrochlore phases. To form the completely pure perovskite phase, the repeating processes of calcining, crushing, and calcining were required. However, the complicated processing and a longer sintering time may lead to the following reverse reaction as a result of PbO loss:

$$Pb(Mg_{1/3}Nb_{2/3})O_3 \longrightarrow 1/6Pb_3Nb_4O_{13} + 1/2PbO + 1/3MgO \qquad (3.4)$$

Inada concluded that to form the single phase PMN, it is necessary to repeat the process of calcining while preventing the evaporation of PbO [100]. Clearly, preparing the materials using these procedures is time-consuming and even after many repeating processes, the pyrochlore phase could not be completely eliminated.

A greatly improved procedure for the synthesis of PMN and various relaxors was discovered by Swartz and Shrout [101]. To avoid the formation of the pyrochlore phase, the reaction sequences of the pyrochlore formation were bypassed by a novel approach. In this approach, the two refractory B-site oxides, i.e. MgO and Nb_2O_5 for PMN, were prereacted to form the columbite $MgNb_2O_6$ precursor phase before the final reaction with PbO, as follows:

$$MgO + Nb_2O_5 \xrightarrow{>1000^\circ C} MgNb_2O_6 \qquad (3.5)$$

$$MgNb_2O_6 + 3PbO \xrightarrow[exo]{>700^\circ C} 3Pb(Mg_{1/3}Nb_{2/3})O_3 \quad (PMN) \qquad (3.6)$$

This columbite method is successful in preparing the perovskite PMN ceramics completely free of pyrochlore phase and can be applied to many other perovskite relaxors.

Similar to PMN, perovskite PSN and PSN–PT ceramics were prepared based on this precursor method [94, 102]. In this case, the two B-site oxides, Sc_2O_3 and Nb_2O_5, were prereacted to form a wolframite compound $ScNbO_4$. This wolframite precursor method has been adopted in this work to synthesize the PSN-PT ceramics with the compositions around the MPB. Besides the two-step synthetic strategy mentioned above, we have studied some other issues, such as the calcining temperature and time, the compensation of the PbO loss and the sintering time. The effects of the processing parameters on the synthetic results have been discussed at each step.

3.3.2 Procedures for the Synthesis of (1-x)Pb($Sc_{1/2}Nb_{1/2}$)O_3 – xPbTiO$_3$ Ceramics.

In general, the procedures of synthesis include the following steps:

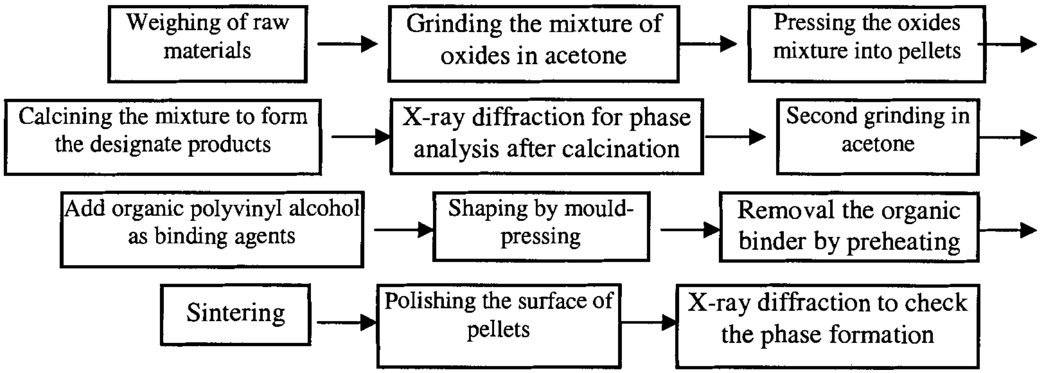

In the following, we describe each step in detail and discuss the considerations taken during the processing, as well as some key points.

1. Preparation of the wolframite precursor

The first step in the processing is to weigh the starting materials according to the stoichiometric formula. We want to prepare the (1-x)Pb($Sc_{1/2}Nb_{1/2}$)O_3 – xPbTiO$_3$ with compositions of x = 0.35, 0.37, 0.38, 0.39, 0.40, 0.41, 0.42, 0.45, and 0.50, i.e. within the MPB. The two B-site oxides for the formation of the precursor $ScNbO_4$ are Sc_2O_3 (99.99%, Japan) and Nb_2O_5 (99.99 %, Alfa Aesar) and they were weighed according to the stoichiometric formula of

$$\mathrm{Sc_2O_3 + Nb_2O_5}\,\frac{1200^{\circ}\mathrm{C}}{4\mathrm{hrs}} > 2\,\mathrm{ScNbO_4} \qquad . \qquad (3.7)$$

After reacting at T=1200 °C for 4 hrs, the formation of $ScNbO_4$ was verified by XRD and the powder was then mixed with PbO (99.99%, GFS Chemicals) and TiO_2

(99.99%, Aldrich Chemical) in stoichiometric amounts to form the complex perovskite compound according to the formula:

$$PbO + 1/2(1-x)\,ScNbO_4 + xTiO_2 \longrightarrow Pb(Sc_{1/2}Nb_{1/2})_{1-x}Ti_xO_3 \quad . \qquad (3.8)$$

The mixture of oxides is thoroughly ground in an acetone-based slurry. The fine powder of raw materials is necessary for the completion of solid-phase reactions through atomic diffusion. The study of the formation of PMN [97] revealed that grinding in acetone help promote the formation of perovskite more than in a water-based slurry. The second grinding of oxides mixture after calcining is also necessary for obtaining a homogeneous mixture before further processing.

2. Formation of the $(1\text{-}x)Pb(Sc_{1/2}Nb_{1/2})O_3 - xPbTiO_3$ solid solution

It was reported that the perovskite phase of $(1\text{-}x)Pb(Sc_{1/2}Nb_{1/2})O_3 - xPbTiO_3$ can be formed at temperatures above 800 °C [71]. In general, a higher calcination temperature favours the formation of the perovskite phase. However, the evaporation of PbO is significantly accelerated when the temperature is higher than 900 °C. Therefore, it is important to calcine the oxide mixture at a temperature below 900 °C. To minimize the evaporation of PbO, we synthesize the $(1\text{-}x)Pb(Sc_{1/2}Nb_{1/2})O_3 - xPbTiO_3$ solid solution at temperatures between 800 and 900 °C. In addition, the mixture is placed into an alumina crucible covered with an alumina lid. Our experimental results show that the perovskite PSN-PT can be formed by keeping the powders at 840 °C for 2 hours. For the formation of the PSN-PT perovskite phase, the reaction sequences are proposed as follows:

First step:

$$PbO + TiO_2 \xrightarrow{>500^\circ C} PbTiO_3 \qquad (3.9)$$

Second step:

$$x\mathrm{PbTiO_3} + 1/2(1-x)\mathrm{ScNbO_4} + (1-x)\mathrm{PbO} \xrightarrow{>800^\circ\mathrm{C}} > \mathrm{Pb(Sc_{1/2}Nb_{1/2})_{1-x}Ti_xO_3} \quad . \tag{3.10}$$

The formation of the perovskite PSN–PT after calcining is confirmed by the powder XRD spectra recorded on a Rigaku (for $x = 0.35, 0.40, 0.45$) or a Philips (for $x = 0.50$) diffractometer, as shown in Figure 3.2. In addition to the main perovskite peaks, a weak peak associated with the pyrochlore phase also appeared at $2\theta \approx 29\,^\circ$ and $34\,^\circ$, suggesting that the PSN-PT obtained by calcination process was not free of pyrochlore phase. The appearance of the pyrochlore phase is attributed to the relatively low reaction temperature (840 °C) and to the partial loss of PbO, both favouring the formation of the pyrochlore phase. Therefore, we tested several combinations with 2-5% excess of PbO added to the mixture prior to the calcining processing and monitored the weight loss of the mixture after calcining and sintering. We found that if the pellets were sintered in the special set up of PbO-rich environments (Figure 3.3), 2% excess of PbO added to the mixture was enough to compensate for the PbO loss by volatilization. Therefore, 2% excess of PbO was introduced in the later processing.

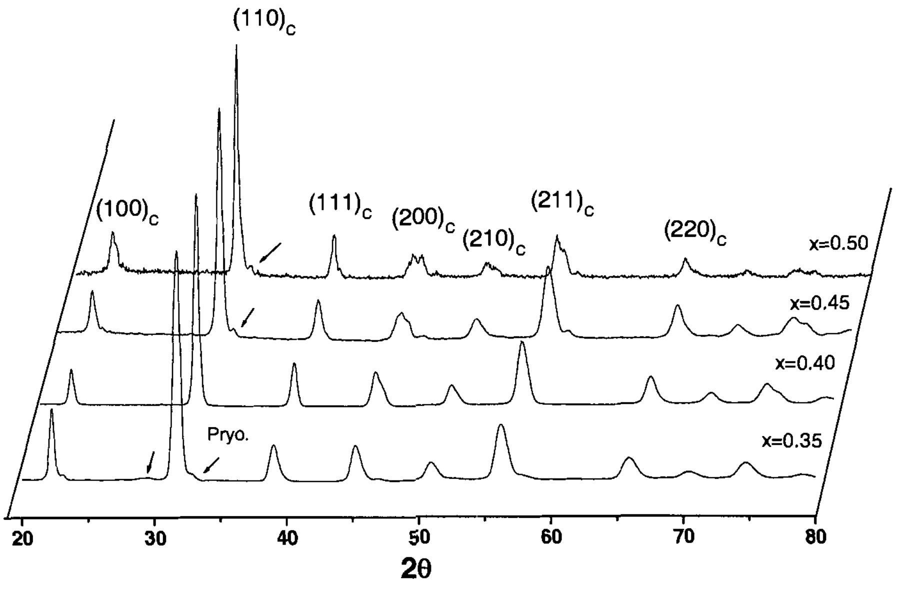

Figure 3.2: XRD spectra of the (1-*x*)PSN–*x*PT mixture (*x* = 0.35, 0.40, 0.45, and 0.50) after calcining at 840 °C for 2 hrs, showing the formation of the perovskite phase with trace amounts of the pyrochlore phase.

3. Sintering of the (1-x)$Pb(Sc_{1/2}Nb_{1/2})O_3 - x PbTiO_3$ ceramics

We found that to shape the PSN–PT powders into pellets, it was necessary to add a binder agent. Otherwise, the disk plates formed by mould-pressing often contain layers, making the final ceramics useless. Polyvinyl alcohol (PVA) of 3–7 wt.% of the total weight of the PSN-PT powder was added before the mould pressing. Disk-shaped pellets with a diameter of 15 mm were obtained. The pellets were then heated up at a rate of 200 °C/h and kept at 800 °C for 1.5 hours to remove the PVA binder in order to avoid the presence of porous structure in the resulting ceramic samples.

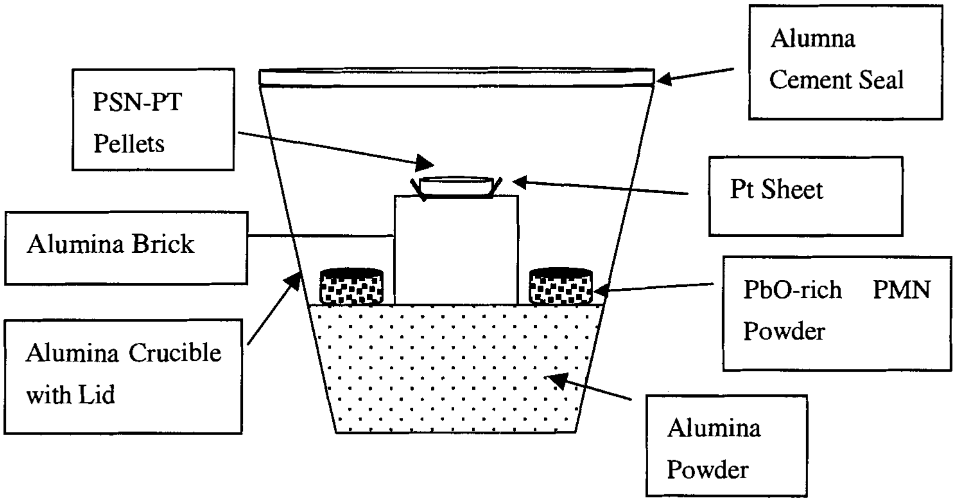

Figure 3.3: Schematic side section view of the crucible setup for the sintering of the $(1\text{-}x)Pb(Sc_{1/2}Nb_{1/2})O_3 - xPbTiO_3$ ceramics

The final step for the synthesis of PSN–PT ceramics is the sintering at high temperature to reach further densification. In order to obtain highly densified ceramics of high quality, the sintering process is a very important step. The key parameters of the sintering process are the sintering temperature and the sintering time. In general, a higher sintering temperature and a longer sintering time will results in grains of larger size [4]. We tested several combinations of sintering temperature and time in order to obtain good quality PSN–PT ceramics with pure perovskite phase. To optimize the sintering results, we also take into consideration the PbO loss. Obviously, a higher temperature and a longer time will cause more loss of PbO. Therefore, we sintered the PSN–PT pellets in a PbO-rich environment created within a sealed Al_2O_3 crucible. Because scandium oxide is relatively expensive, we use PbO-enriched PMN powder instead of PSN powder for creating the PbO-rich environment. This special set up is shown in Figure 3.3.

The phase formation in the sintered $(1\text{-}x)Pb(Sc_{1/2}Nb_{1/2})O_3 - xPbTiO_3$ ceramic pellets was checked by XRD spectra. It was found that the XRD patterns of the sintered

PSN–PT are slightly different from those of the calcined PSN–PT powders. Figure 3.4 shows the comparative XRD spectra of 0.50PSN–0.50PT as an example. The tetragonal splitting of the $(100)_c$, $(200)_c$ and other peaks appears very clearly in the sintered sample, but it is not as clear in the calcined sample. Although the smaller grain size in the calcined sample could result in some broadening of the X-ray peaks, this is unlikely the main reason for such a difference. This result suggests that the formation of the tetragonal phase in 0.50PSN–0.50PT was not complete after the calcining process, in other words, the chemical reactions continued during the sintering process.

Moreover, careful examination of the XRD spectra in Figure 3.4 reveals that in the 0.50PSN–0.50PT sample sintered at 1240 ^{o}C for 2 hours, the pyrochlore phase is still present, as shown by the weak peak at $2\theta \approx 29.5\ ^{o}$. Therefore, the composition of the ceramics sintering at 1240 ^{o}C for 2 hrs may have drifted away from the nominal composition of 0.50PSN-0.50PT.

Based on the above observations, the sintering temperature and time of the PSN–PT ceramics were adjusted to 1270 – 1280 ^{o}C for 6 to 8 hours, as shown by the temperature profile in Figure 3.5. Under these sintering conditions, the resulting PSN–PT ceramics show a shrinkage of about 13% in diameter. The relative density of the ceramics measured by the Archimedes method is higher than 95% (of the theoretical value). XRD spectra confirm the formation of a clean perovskite phase free of pyrochlore phase for all the samples. More detailed results will be discussed in the following section.

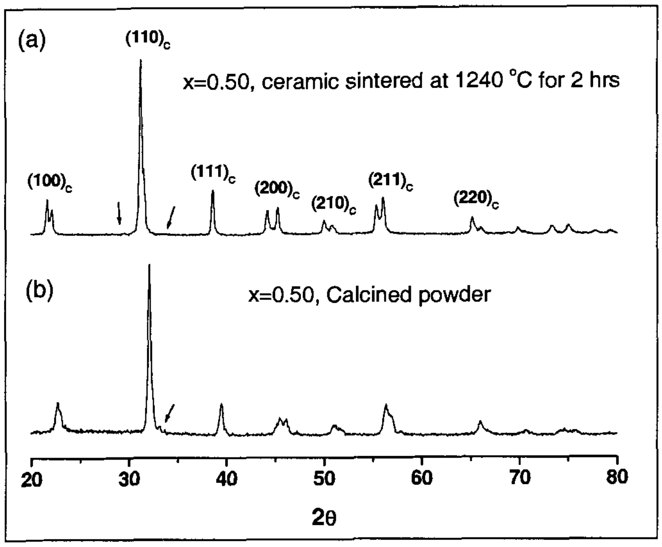

Figure 3.4: Comparison of the X-ray profiles between the calcined and sintered ceramic samples of 0.50PSN–0.50PT:
a) ceramic sintered at 1240 °C for 2 hrs; b) calcined powder.

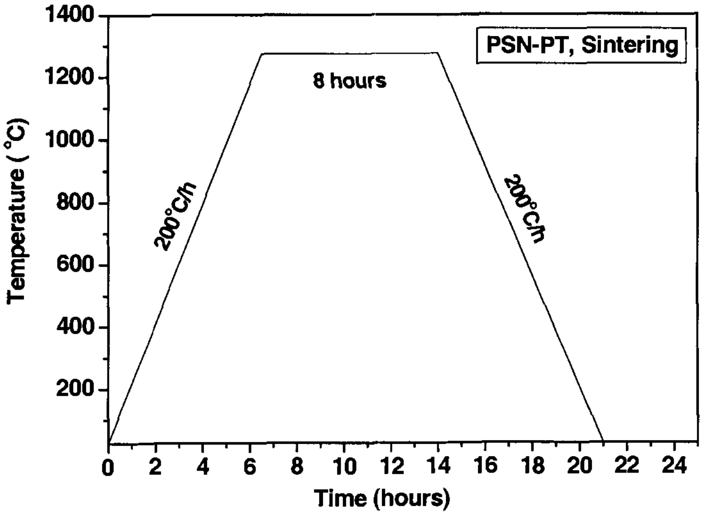

Figure 3.5: Typical temperature profile for the sintering of $(1\text{-}x)Pb(Sc_{1/2}Nb_{1/2})O_3 - xPbTiO_3$ ceramics

3.4 Composition–Induced Structural Phase Transition

3.4.1 Experimental

After sintering, the ceramic pellets were polished with fine diamond paste (9 μm) and cleaned in an ultrasonic bath. To eliminate possible strains caused during polishing and cleaning, the samples were annealed at 700 °C for 2 hrs. For X-ray diffraction, selected ceramic pieces were slowly ground into fine powder in order to obtain a better averaging of the data.

X-ray diffraction was performed on a Philips X-ray diffractometer with Cu Kα radiation. The data were collected with step scans at 0.02 ° intervals over an angular region from 10 to 80 ° and a count time of 2 seconds. For the structural analysis, the pseudocubic reflections $(111)_c$ and $(200)_c$ were fitted to a Lorentzian function using the intensity, the peak position (2θ) and the full width at half maximum (FWHM) as variables. One exception is for the $(200)_c$ reflection of $x = 0.35$, which was fitted better by a Gaussian function. The diffracted intensities were normalized with respect to the maximum of peak intensity in the entire spectrum.

The temperature dependences of the heat flow of the (1-x)PSN–xPT ceramics with compositions of x = 0.35, 0.37, 0.38, 0.39, 0.40, 0.41, 0.42, 0.45, and 0.50 were measured on a differential scanning calorimeter (DSC6200, Seiko Exstar). Approximately 60 mg of small crushed pieces of ceramics of each sample were used as specimens and a 10 °C/min heating and cooling rate was employed.

The dielectric permittivity as a function of temperature at various frequencies (from 10 to 100 kHz) was measured from 400 °C down to 10 °C at 2–3 °C intervals by means of an Alpha High Resolution Dielectric/Impedance Analyzer (NovoControl). The stabilization of temperature was within 0.1 °C with an error of ±0.025 °C. For the permittivity measurements, the circular surfaces of the samples were sputtered with gold layers as electrodes and two gold wires were attached to the electrode with silver paste.

3.4.2 X-ray Spectra of the (1-x)Pb(Sc$_{1/2}$Nb$_{1/2}$)O$_3$ – xPbTiO$_3$ Ceramics

Figure 3.6 shows the X-ray spectra of the (1-x)PSN–xPT ceramics with compositions of $x = 0.35$, 0.37, 0.38, 0.39, 0.40, 0.41, 0.42, 0.45, and 0.50.

From the X-ray spectra, we can draw the following conclusions: 1) all ceramics show a clean perovskite phase completely free of impurities; 2) for the composition $x = 0.45$, the tetragonal splits are visible on the cubic (100), (110), (200) (210) and (112) peaks, and these splits become more clear for the composition $x = 0.50$; 3) for $x = 0.42$, a broadened peak with an asymmetrical profile is observed for the cubic (200), (210) and (112) reflections; 4) apparently, the symmetry of the phase gradually changes from rhombohedral to tetragonal upon increasing Ti-content from $x = 0.35$ to $x = 0.50$.

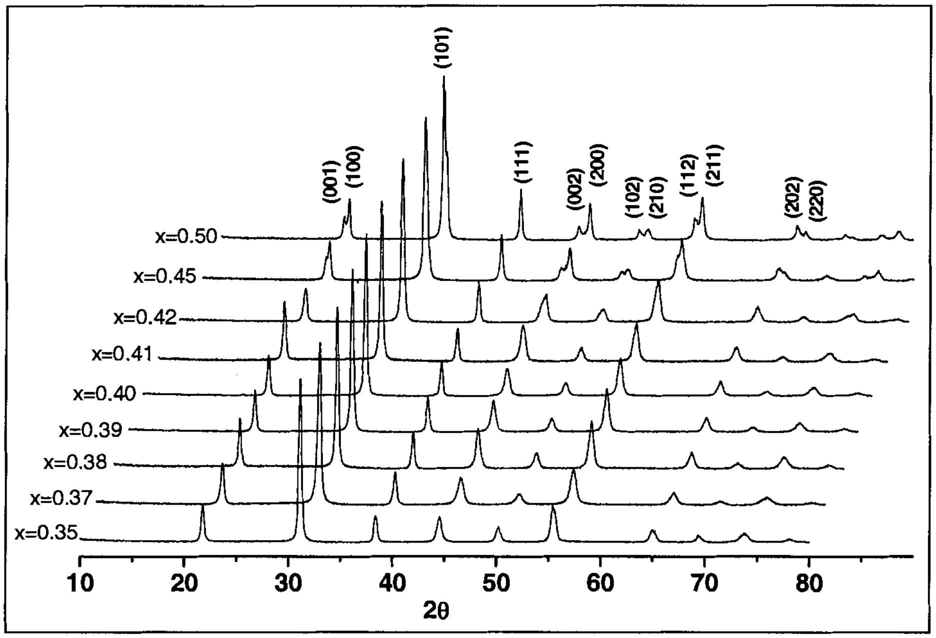

Figure 3.6: X-ray spectra of the (1-x)Pb($Sc_{1/2}Nb_{1/2}$)O_3 – xPbTiO_3 ceramics with compositions around the MPB.

3.4.3 Structural Analysis

Figure 3.7 shows the experimental XRD data (open circles) of the pseudocubic $(111)_c$ and $(200)_c$ reflections, the fitting profile, the curves after deconvolution and the residues of the fitting results for compositions of x =0.35, 0.37, 0.38, 0.39, 0.41, 0.42, 0.45, and 0.50 [The $(220)_c$ reflection was unfortunately too weak to be analyzed]. The residues represent the difference between the fitting to the theoretical functions and the experimental data. The vertical lines indicate the peak positions after deconvolution of the peak profile with approximate intensity ratios, as explained in **Chapter 2** (Figure 2.5). The detailed fitting results are shown in Appendix III.

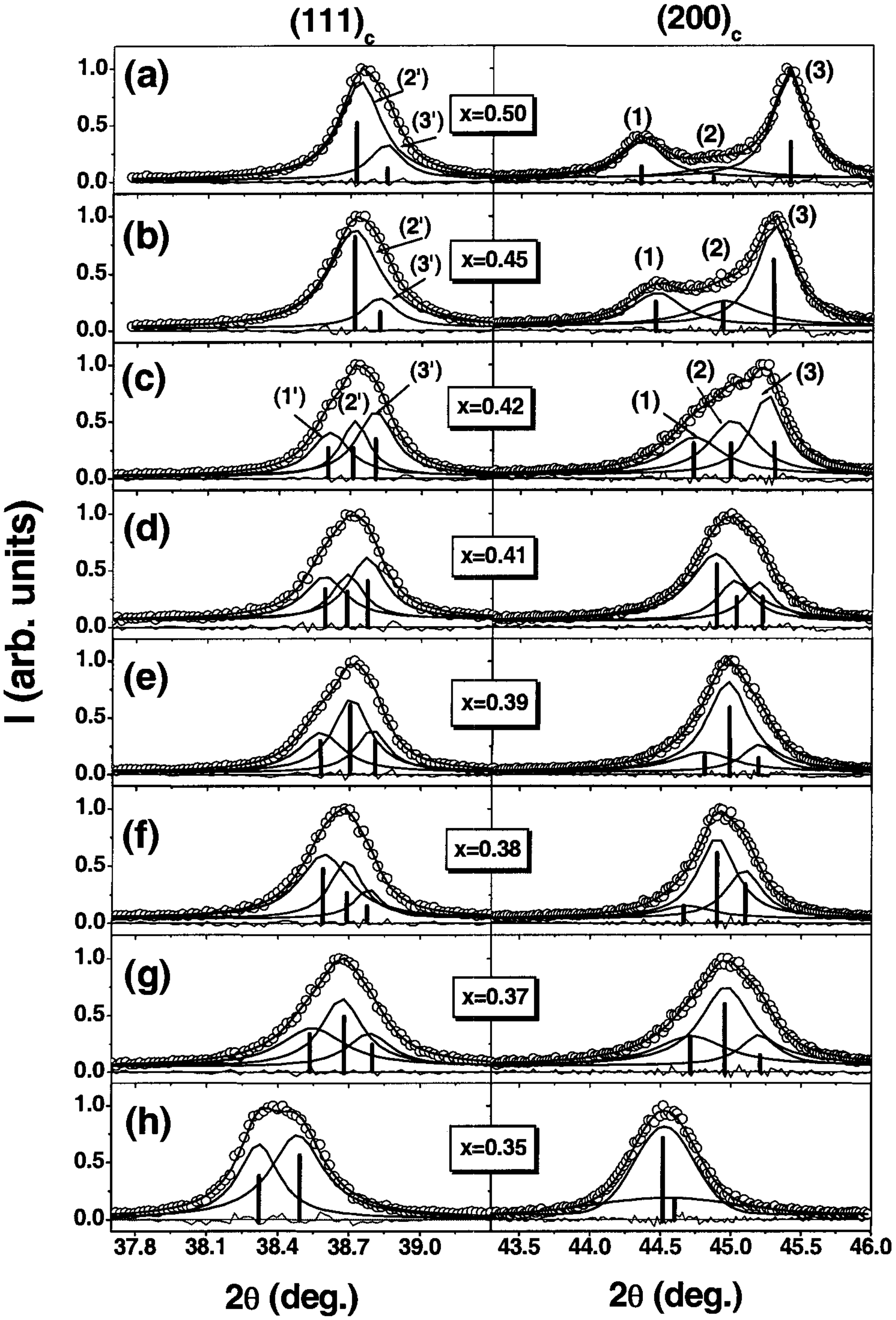

Figure 3.7: Pseudocubic $(111)_c$ and $(200)_c$ reflections (open circles) of (1-x)PSN–xPT with composition x = 0.35, 0.37, 0.38, 0.39, 0.41, 0.42, 0.45 and 0.50 at room temperature, and the deconvolution of the peak profile with different phase components (see the text for details).

For x = 0.50, the splitting of the $(200)_c$ reflection into peak (1) and peak (3) [Figure 3.7(a)] and the dominant peak on the $(111)_c$ reflection [peak (2′)] indicate that the major phase adopts the tetragonal symmetry. However, a weak peak [peak (2)] exists between peak (1) and peak (3) of the $(200)_c$ reflection and another one [peak (3′)] appears besides peak (2′) of the $(111)_c$ reflection. These weak peaks reveal the onset of another phase of different symmetry. For $x = 0.45$, the tetragonal symmetry can still be identified by the two distinct peaks [peak (1) and peak (3) in Figure 3.7(b)], but the intensity of peak (2) has increased, indicating that the second phase steadily grows as the Ti-content decreases.

For $x = 0.42$ [Figure 3.7(c)], the tetragonal splitting of $(200)_c$ becomes less clear as peak (1) and peak (3) tend to merge, giving rise to a broadened complex reflection profile, which can be fitted into three peaks: peaks (1) – (3). With the appearance of peak (1′), the $(111)_c$ reflection of $x = 0.42$ also shows three distinct peaks: peaks (1′) – (3′) [Figure 3.7(c)]. According to the theoretically calculated characteristic splittings for the different phases (Figure 2.5, **Chapter 2**), peaks (1′) and (3′) on the $(111)_c$ reflection and peaks (1) – (3) on the $(200)_c$ reflection indicate the presence of a monoclinic phase, which has become the major phase in $x = 0.42$. This monoclinic phase is mixed with some amount of the tetragonal phase which corresponds to peak (2′) on $(111)_c$ and peaks (1) and (3) on $(200)_c$ that overlap with two of the monoclinic peaks. This mixture of monoclinic and tetragonal phases is also found for the compositions of $x = 0.41$ to 0.37 [Figure 3.7(d) – (g)], in which both the $(111)_c$ and $(200)_c$ reflections show qualitatively the features similar to $x = 0.42$.

As x decreases to 0.35 [Figure 3.7(h)], the $(111)_C$ reflection can be fitted into two peaks that are significantly shifted to lower angles, while the $(200)_C$ reflection can be well defined by a single peak (plus a broad peak due to background diffusion) of Gaussian function. According to Figure 2.5, the two distinct peaks for $(111)_C$ and the dominant peak for $(200)_C$ are the signature of the rhombohedral symmetry, indicating the formation of the *R3m* phase for $x = 0.35$.

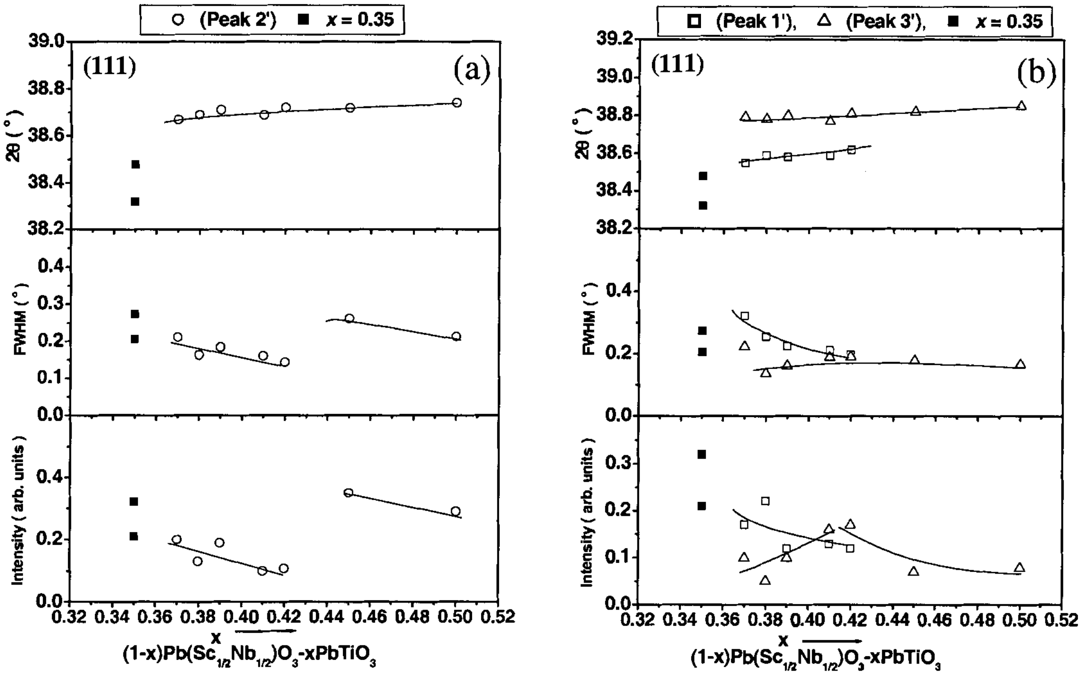

Figure 3.8: Plot of 2θ, FWHM and intensity for the characteristic peaks obtained by the deconvolution of the $(111)_C$ reflection, as a function of composition x, for PSN-PT ($0.35 \leq x \leq 0.50$).
(a): peak (2′), and (b): peak (1′) and peak (3′), of the (111) reflection (see Figure 3.7). The data for $x = 0.35$ are shown in both (a) and (b) for comparison.

To study the transformation of the phases upon variation of composition within the MPB of $(1-x)$PSN − xPT, we have plotted the 2θ angle, the full width at half maximum (FWHM) and the intensity as a function of composition x for peak (2′) [(a)] and peaks (1′) and (3′) [(b)] of the $(111)_c$ reflection in Figure 3.8. It can be seen that the FWHM and intensity of peak (2′), which initially indicates the tetragonal phase, undergo a discontinuous change between $x = 0.45$ and 0.42. This indicates the transformation of the tetragonal phase into the monoclinic phase. The appearance of peak (1′) at $x = 0.42$ [Figure 3.8 (b)], which is one of the signature peaks for the monoclinic symmetry, also confirms the sudden growth of the monoclinic phase which becomes the major phase at the expense of the tetragonal phase for the compositions of $0.37 \leq x \leq 0.42$.

As x decreases from 0.37 to 0.35, the structural parameters undergo discontinuous changes in 2θ, FWHM and intensity, as shown by the solid squares in Figure 3.8 (a) and (b) for both $(111)_c$ and $(200)_c$ reflections, indicating an abrupt phase transition into the rhomboderal symmetry for $x = 0.35$.

Based on the above analysis, we can see that the solid solution of (1-x)PSN – xPT with compositions in the MPB region exhibits a complex phase mixture with the monoclinic phase that appears as the major phase for $0.37 \leq x \leq 0.42$, and some amount of the tetragonal phase. This observation is in agreement with the recent report by Haumont *et al.* [96], who evidenced a monoclinic phase (of *Pm* or *Cm* symmetry) as the ground state combined with some amount of the tetragonal phase for PSN-PT of composition $x = 0.43$.

3.4.4 Thermal Analysis by Differential Scanning Calorimetry (DSC)

Figure 3.9 shows the DSC measurement for the 0.50PSN–0.50PT ceramics as an example. The thermal anomalies with an endothermic peak on heating and an exothermic peak on cooling have been observed. The thermal events show an onset temperature of

306 °C upon heating and 310 °C upon cooling, but the corresponding peak temperatures (from DDSC) are 310 °C and 305 °C, respectively, showing a normal thermal hysteresis. The peak temperature on cooling is consistent with the permittivity peak temperature of 0.50PSN–0.50PT (304 °C). The same measurements were carried out on the ceramic samples of different compositions. Figure 3.10 shows the plots of the DSC measurements on heating.

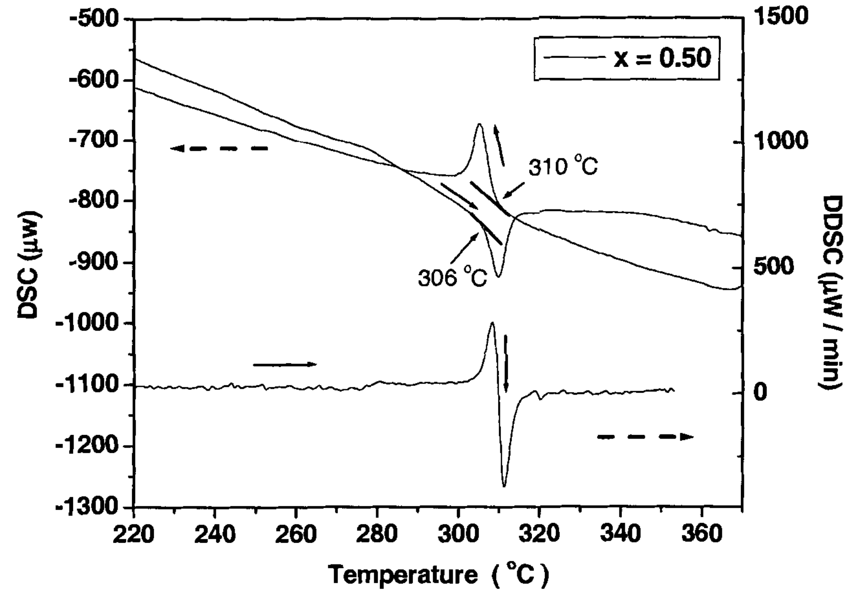

Figure 3.9: DSC measurement of 0.50PSN–0.50PT ceramics as a function of temperature on heating and cooling.

The thermal events detected by the DSC measurements indicate a structural phase transition for all the samples studied. The temperature of the phase transition is in good agreement with the Curie temperature T_C, at which the peak of dielectric permittivity occurs (see **Section 3.4.5**). An additional weak anomaly is observed in the low temperature side of the major DSC peak for x = 0.35, which corresponds to the morphotropic phase transition temperature T_{MPB}, also observed in the dielectric permittivity measurements (see details in the following section). This transition should appear in some other compositions, but the thermal anomalies are too weak to be detected.

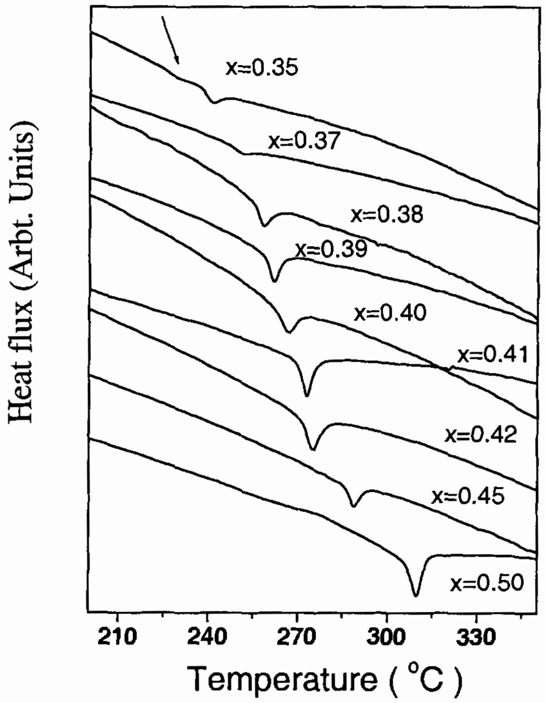

Figure 3.10:DSC measurements for the (1-x)Pb($Sc_{1/2}Nb_{1/2}$)O_3 – xPbTiO$_3$ ceramics with compositions of x =0.35, 0.37, 0.38, 0.39, 0.40, 0.41, 0.42, 0.45, and 0.50.

3.4.5 Dielectric Permittivity Studied by Impedance Analysis

The real permittivity of the PSN–PT ceramics as a function of temperature for the compositions x = 0.35, 0.37, 0.38, 0.39, 0.40, 0.41, 0.42, 0.45, and 0.50 is shown in Figure 3.11 for the frequency f = 100 kHz. The spectral features depend on the compositions. For $x = 0.45$ and $x = 0.50$, only one anomaly appears at $T_C \approx 286$ °C and $T_C \approx 305$ °C, respectively, corresponding to the phase transition from the paraelectric cubic to the ferroelectric tetragonal phase. For the compositions of $0.35 \leq x \leq 0.42$, however, the permittivity spectrum clearly shows two anomalies. In addition to the sharp peak at T_C, another shoulder-like anomaly appears at a lower temperature, named T_{MPB}, indicating a second transition from the ferroelectric tetragonal phase into another ferroelectric phase(s). As Ti-content decreases, T_C moves to a lower temperature, while T_{MPB} shifts to a higher temperature. The two anomalies are nearly merged for $x = 0.35$. The appearance of T_{MPB} and the associated phase transition in PSN–PT indicate the typical features of the morphotropic phase boundary behaviour, as previously observed in the PZT, PMN–PT and PZN–PT systems [35, 45, 52, 44, 93,].

Figure 3.12 shows the plot of the maximum dielectric constant, ε'_{max}, and the room temperature dielectric constant, ε'_{RT}, as a function of composition x. For the plot of ε'_{max} vs. x (upper part), as x decreases to 0.35, ε'_{max} shows a sharp increase, reaching a value of 50,000. The plot of ε'_{RT} vs. x (lower part) shows a dome shape: as x increases from 0.35 to 0.50, ε'_{RT} gradually increases and reaches a maximum value of about 1800 for the composition around $x = 0.44$; it then decreases at $x > 0.45$. The high dielectric constant ε'_{RT} in the composition rang $0.42 \leq x \leq 0.45$ is attributed to the effects of multiple polarization states within the morphotropic phase boundary region (see **Section 3.5**), which are believed to enhance the dielectric properties of the materials.

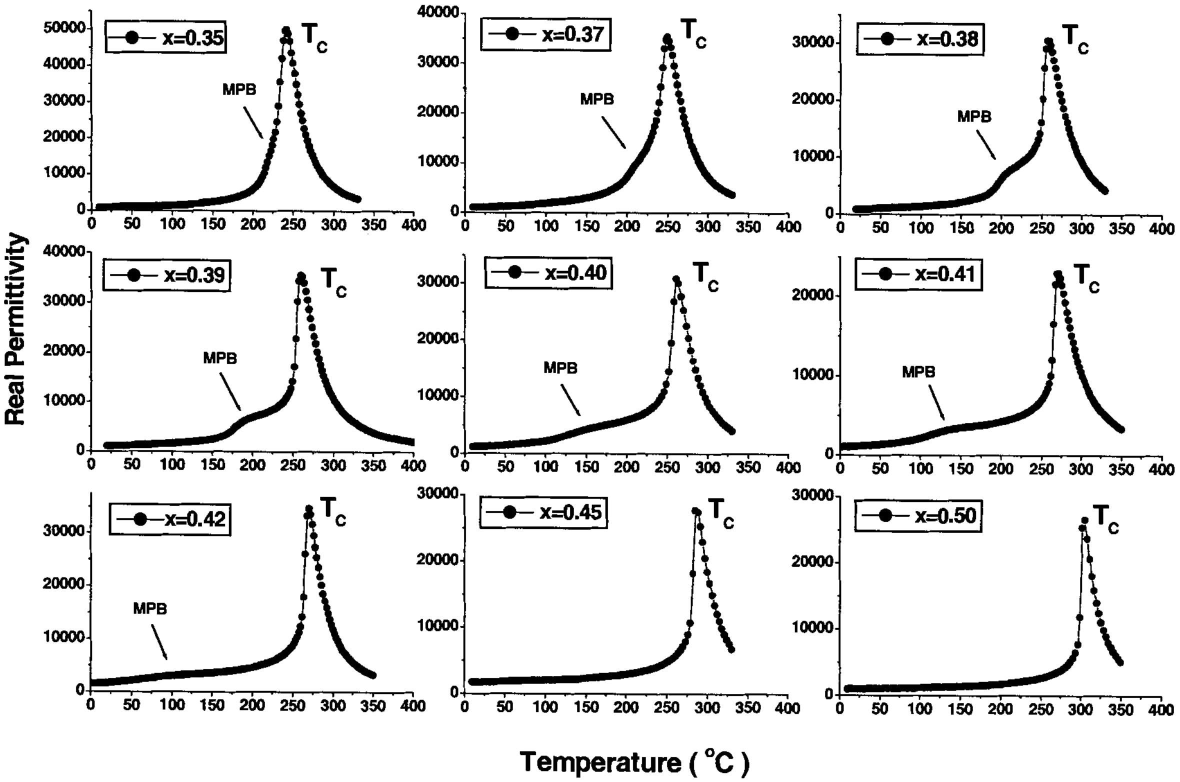

Figure 3.11:Real permittivity of the PSN–PT ceramics as a function of temperature for the compositions x = 0.35, 0.37, 0.38, 0.39, 0.40, 0.41, 0.42, 0.45, and 0.50 at the frequency f = 100 kHz.

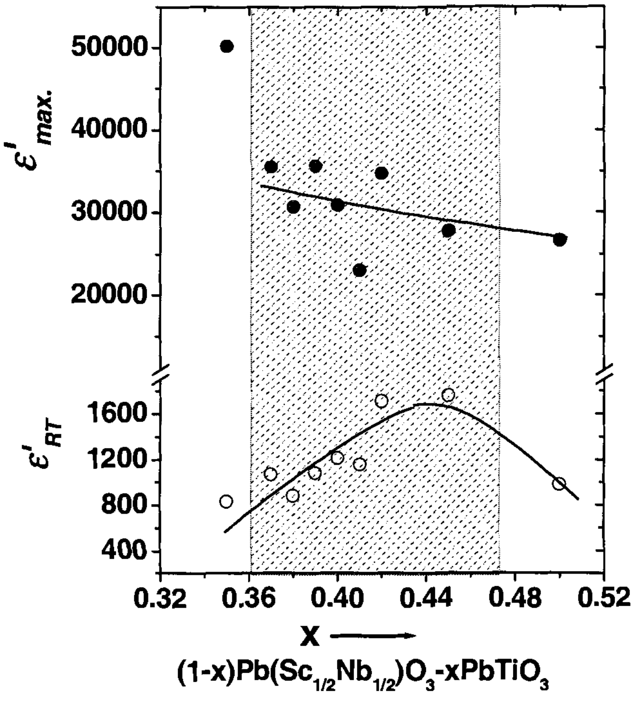

Figure 3.12:Plots of ε'_{max} (solid circles) and ε'_{RT} (open circles) as a function of composition x for the PSN–PT solid solution. The trend lines are for eye guide.

3.5 Establishment of the Morphotropic Phase Diagram of the $(1\text{-}x)Pb(Sc_{1/2}Nb_{1/2})O_3 - xPbTiO_3$ Solid Solution System

Based on the above X-ray, DSC, and dielectric results, we have established the phase diagram for the solid solution of PSN–PT with compositions around the MPB, as shown in Figure 3.13. The data from Ref. [71] and Ref. [96] are also shown for comparison. The para-/ferroelectric phase transition temperature T_C is in good agreement with the previously reported data [71, 96].

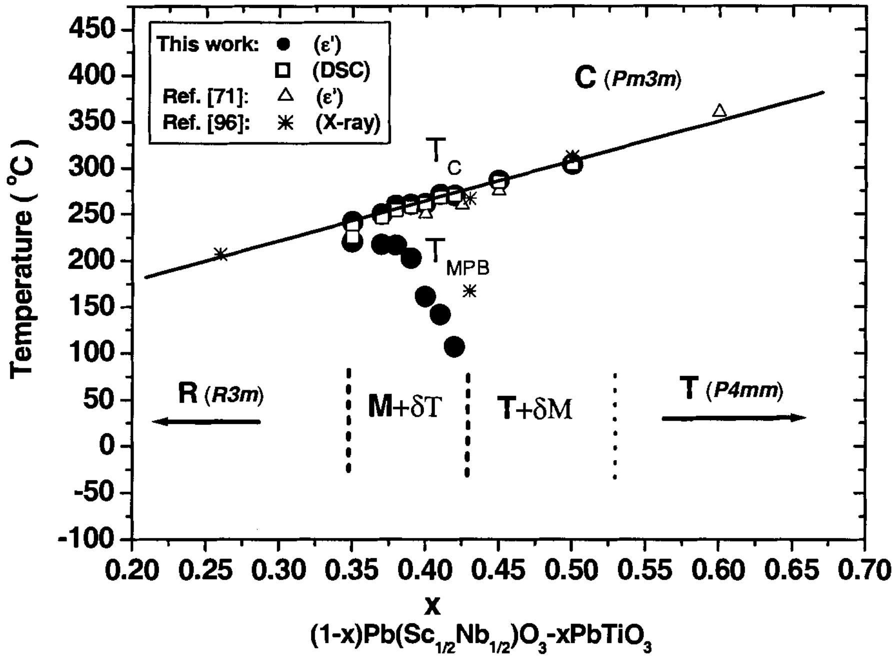

Figure 3.13:Phase diagram for the (1-x)Pb($Sc_{1/2}Nb_{1/2}$)O_3 – xPbTiO_3 solid solution around its MPB established based on the results of this work. Data from *Ref.* [71] (open triangles), and data from *Ref.* [96] (stars) are also shown for comparison. Solid circles are the boundary between the tetragonal phase (at high temperature) and M+δT phase(s) at low temperature, which represents the upper limit of the MPB region with the monoclinic phase in majority.

The most important feature of this phase diagram is that the MPB region is identified as a mixture of the monoclinic (M) phase in majority and some amount of the tetragonal (T) phase for $0.35 < x < 0.42$ at or around room temperature. At RT, with x increasing from 0.42 to 0.50, the tetragonal phase (T) becomes the major phase with the monoclinic phase persisting in a small amount. Therefore, as PT–content (x) increases, the (1-x)PSN–xPT solid solution undergoes a sequence of structural changes from the rhombohedral (R) phase ($x \leq 0.35$), to the monoclinic M+δT ($0.35 < x < 0.45$), to the tetragonal T+δM ($0.45 \leq x \leq 0.50$) and then to the tetragonal (T) phase ($x > 0.50$) (the pure tetragonal phase was observed in Ref. [96] for $x \geq 0.55$).

The morphotropic phase boundary region shows a curved upper limit, which indicates the temperatures of the morphotropic phase transition T_{MPB}. Upon cooling through T_{MPB}, PSN–PT transforms from a tetragonal phase into either a mixture of the monoclinic and tetragonal phases (for $0.37 \leq x \leq 0.42$) or to the rhombohedral phase (for $0.35 \leq x < 0.37$). The curvature of the MPB upper limit indicates the dependence of the morphotropic phase transition temperature on the composition. Interestingly, the compositions of $0.35 \leq x \leq 0.39$ exhibit both a high T_{MPB} (> 175 °C) and a high T_C (> 200 °C), making them the most interesting materials for high temperature piezoelectric applications.

3.6 Electrical Characterization

The temperature and frequency dependences of the dielectric permittivity were measured on unpoled $(1-x)\mathrm{Pb(Sc_{1/2}Nb_{1/2})O_3} - x\mathrm{PbTiO_3}$ ceramics. Figure 3.14 shows the real permittivity and the losses as a function of temperature at the frequencies of 1, 10, and 100 kHz for the selected compositions of 35, 40, and 50 mol% $\mathrm{PbTiO_3}$. A sharp peak of the real permittivity appears at the ferroelectric Curie temperature, T_C *(or* T_{max}) = 240, 261, and 305 °C, respectively. No frequency dispersion of the real permittivity can be observed in the whole temperature range near and below the dielectric maximum (T_{max}), indicating that the PSN-PT ceramics with compositions in the range of $0.35 \leq x \leq 0.50$ behave mostly like normal ferroelectrics. The sharp transition also points to the high quality of the ceramics. However, frequency dispersion in the loss data can be observed.

This suggests that PSN–PT with compositions near the MPB still retains some degrees of relaxor characters. As expected, T_C (T_{max}) increases linearly as a function of the $PbTiO_3$ content.

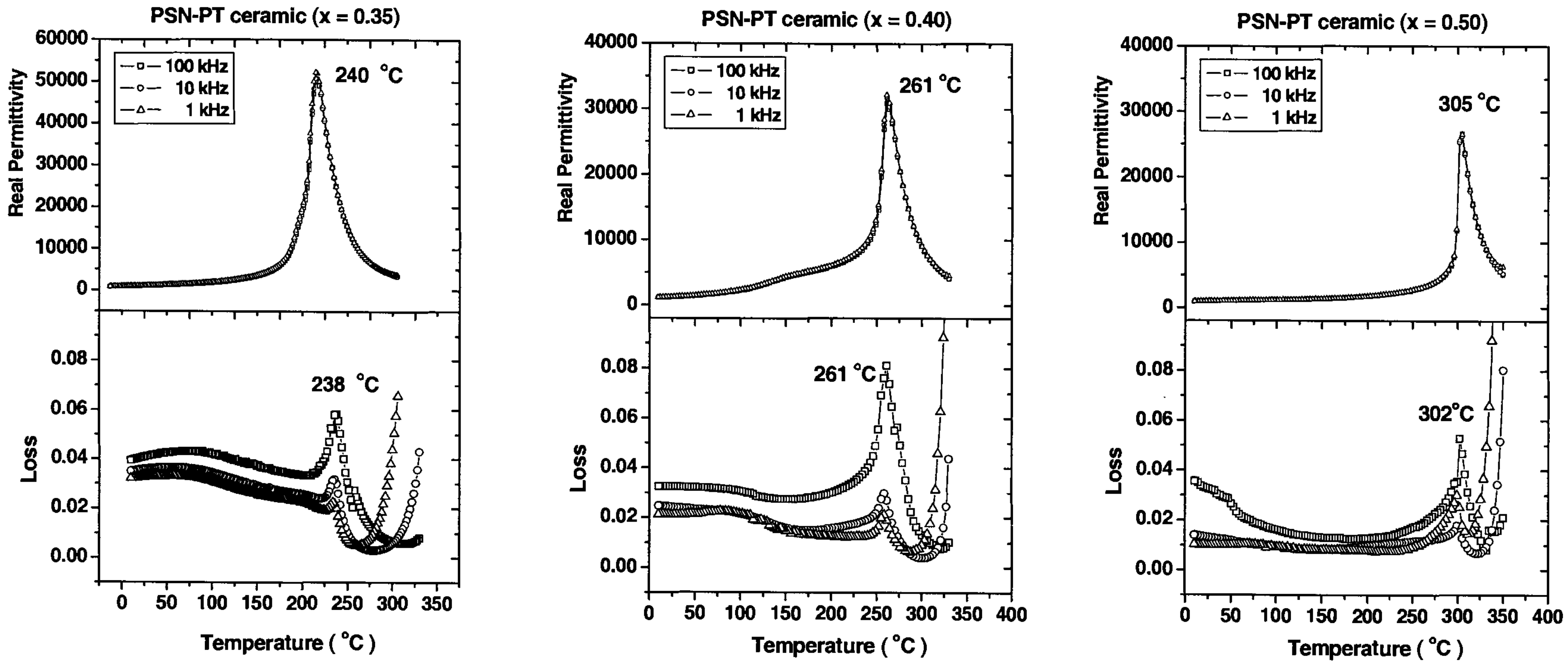

Figure 3.14:The real permittivity and loss, at frequencies of 1, 10, and 100 kHz for the selected compositions of 35, 40, and 50 mol% $PbTiO_3$

PSN-PT samples with compositions near the MPB are confirmed to be ferroelectric at room temperature by polarization –electric field hysteresis loops. Typical hysteresis loops for 0.60PSN-0.40PT at different applied electric fields (±7.5 kV/cm and ±12 kV/cm) are shown in Figure 3.15(a). The remnant polarization reaches $P_r \approx 22$ μC/cm^2 under a drive of $E \approx \pm 12$ kV/cm with a coercive field of $E_C \approx 5$ kV/cm.

Figure 3.15(b) shows the variation of strain as function of a bipolar electric field for the same sample. It displays a symmetric "butterfly" loop, resulting from the bipolar ferroelectric switching behaviour. A peak-to-peak strain value of 0.15% is obtained at $E = \pm 10$ kV/cm.

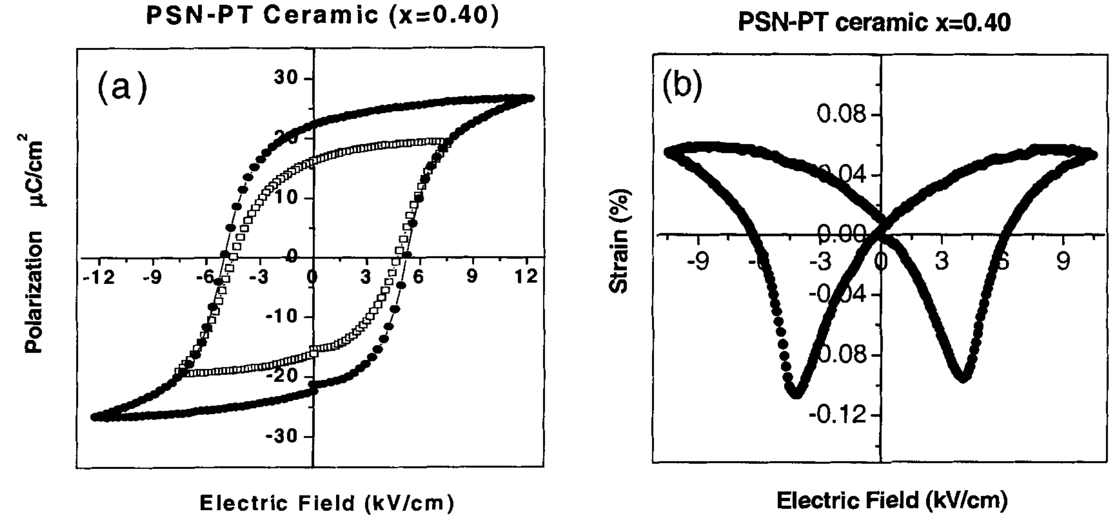

Figure 3.15: Typical hysteresis loops and strain-electric field variation for 0.60PSN – 0.40PT ceramics under a bipolar drive.
(solid circle: 12 kV/cm, and open square: 7.5 kV/cm)

3.7 Summary

The ceramics of (1-x)Pb($Sc_{1/2}Nb_{1/2}$)O_3 – xPbTiO_3 solid solution with compositions within the MPB region ($0.35 \le x \le 0.50$) have been synthesized by an improved two-step wolframite precursor method. The synthetic process has been optimized in terms of wet grinding, calcining, and sintering conditions. Based on the proposed procedures, pure perovskite ceramics have been synthesized, completely free of impurities as measured by XRD. The $(1-x)Pb(Sc_{1/2}Nb_{1/2})O_3 - xPbTiO_3$ ceramics have been characterized by the dielectric, ferroelectric and piezoelectric properties. A dielectric maximum as high as 50,000 is obtained for the 0.65PSN-0.35PT ceramic with losses smaller than 0.05. The values of the remnant polarization and the strain level of the PSN–PT ceramics are comparable to those of the PZT ceramics.

The studies of the phase transition by permittivity and DSC measurements show a clear peak at T_C, at which the transition from the paraelectric to ferroelectric phase takes place. Two anomalies, corresponding to the MPB transition and the ferro-/paraelectric transition, are detected in the spectrum of dielectric constant as a function of temperature for the compositions of $0.35 \leq x \leq 0.42$ upon cooling, while only one anomaly is observed for the compositions of $x = 0.45$ and 0.50. Analysis of the X-ray powder diffraction patterns reveals that for the compositions of $0.37 \leq x \leq 0.42$ the spectra cannot be resolved by a single phase model, nor by a simple mixture of the tetragonal and the rhombohedral phase. Instead, a third phase of monoclinic symmetry is found to be present. It exists as the major phase in the composition range of $0.37 \leq x \leq 0.42$.

Based on these results, a new phase diagram of the PSN–PT solid solution has been established. It delimits the MPB region with a curved upper boundary. Interestingly, the solid solution of the MPB compositions ($0.35 \leq x \leq 0.39$) displays a $T_{MPB} > 175$ °C and a $T_C > 200$ °C, both higher than those of the PMN–PT and PZN–PT solid solutions, making the PSN–PT system very promising piezo- and ferroelectric materials for high temperature applications.

It should be mentioned that due to the complexity of phase mixture in the MPB compositions, high resolution synchrotron X-ray diffraction is needed in the future to determine more accurately the MPB phase components and ratios, and the structure of the monoclinic phase. These pieces of information are very desirable because it is expected that the different phase components affect the local structure and hence the properties of PSN–PT with compositions within the MPB region.

Chapter 4:
Growth and Characterization of Relaxor Ferroelectric $Pb(Sc_{1/2}Nb_{1/2})O_3$ and $(1-x)Pb(Sc_{1/2}Nb_{1/2})O_3 - xPbTiO_3$ Single Crystals

The following chapter is a revised version of the paper published in **Journal of Crystal Growth** by **Y. -H. Bing, and Z. -G. Ye,** (*J. Cryst. Growth*, **250**, 118-125, 2003). The use of this article is by permission of the publisher of Elsevier, Science Direct (Home websites: http://www.elsevier.com)

In this chapter, the effects of chemical compositions and thermodynamic and kinetic parameters on the growth of relaxor ferroelectric $Pb(Sc_{1/2}Nb_{1/2})O_3$ and $(1-x)Pb(Sc_{1/2}Nb_{1/2})O_3 - xPbTiO_3$ solid solution single crystals have been investigated. The electric properties of the grown $(1-x)Pb(Sc_{1/2}Nb_{1/2})O_3 - xPbTiO_3$ single crystals have been characterized by the measurements of dielectric, ferroelectric and piezoelectric properties.

4.1 Abstract

Single crystals of complex perovskite $Pb(Sc_{1/2}Nb_{1/2})O_3$ and $(1-x)Pb(Sc_{1/2}Nb_{1/2})O_3-xPbTiO_3$ (PSN–PT/PSNT) solid solution with composition near the morphotropic phase boundary (MPB) ($x=0.425$) were grown by an improved high temperature solution method. The mixtures of PbO and B_2O_3 with different ratios were used as flux. The variations of chemical compositions, such as the ratios of PSN–PT vs. flux and PbO vs. B_2O_3, were shown to influence the morphology and quality of the

grown crystals. By appropriately adjusting the chemical parameters, the optimum chemical compositions were found, which resulted in the growth of high quality crystals. The dielectric, ferroelectric and piezoelectric properties of the grown (1-x)Pb($Sc_{1/2}Nb_{1/2}$)O_3 – xPbTiO_3 single crystals are reported.

4.2 Introduction

The solid solutions between the lead-based relaxor ferroelectric materials [10, 11], such as Pb($Mg_{1/3}Nb_{2/3}$)O_3 (PMN) and Pb($Zn_{1/3}Nb_{2/3}$)O_3 (PZN), and the normal ferroelectric PbTiO_3 (PT), have been attracting a great deal of attention recently due to their high dielectric constant and extraordinary piezoelectric properties. The success in the growth of single crystals has made it possible to systematically investigate the excellent piezoelectric properties for a wide range of applications as electromechanical transducers. These superior properties outperforming those of the (1-x)PbZrO_3 – xPbTiO_3 (PZT) ceramics have been demonstrated in the single crystals when appropriate crystallographic axes are used [1, 58].

While (1-x)Pb($Zn_{1/3}Nb_{2/3}$)–xPbTiO_3 (PZN–PT) and (1-x)Pb($Mg_{1/3}Nb_{2/3}$)–xPbTiO_3 (PMN-PT) single crystals, with compositions close to the so-called morphotropic phase boundary (MPB), are being intensively investigated and exploited as the next generation of high piezoelectric materials [46, 60,103, 104], lead scandium niobate, Pb($Sc_{1/2}Nb_{1/2}$)O_3 (PSN), and its solid solution with PT are much less-well known. This system could exhibit excellent piezoelectric properties, with a Curie temperature higher than that of either PMN–PT or PZN–PT, which would provide many advantages in a large variety of advanced applications. Therefore, it is of relevance to systematically study this solid solution system.

The $(1-x)Pb(Sc_{1/2}Nb_{1/2})O_3 - xPbTiO_3$ (PSN–PT) binary system was first reported by Tennery *et al.* [71] based on the experiments on ceramic specimens. An MPB was found near the composition $x = 0.425$ (0.575PSN–0.425PT or PSNT57.5/42.5). Yamashita *et al.* [74] reported the electric properties of Nb-doped PSN–PT ceramic samples and the preliminary growth of PSN–PT binary single crystals by a flux method. However, difficulties are still encountered in the growth of PSN–PT crystals because of the very high melting point, $T_m > 1425$ °C [75], of the solid solution system. The problems that arise from the growth and the factors that affect the quality of crystals have not been understood thoroughly. Consequently, the dielectric and piezoelectric properties of the PSN-PT crystals have not been fully studied and exploited due to the poor quality and significant composition fluctuations of the previously grown crystals [74].

It is the purpose of this work to systematically study the growth and properties of the PSN–PT single crystals with compositions near the MPB. The effects of the growth parameters on the morphology and quality of crystals have been investigated. The chemical compositions, such as the ratios of PSN-PT vs. flux and PbO vs. B_2O_3, have been adjusted to optimize the quality of the grown crystals.

4.3 Effects of Chemical Compositions on the Growth of Relaxor Ferroelectric $(1\text{-}x)Pb(Sc_{1/2}Nb_{1/2})O_3 - xPbTiO_3$ Single Crystals

4.3.1 Experimental

Because the melting points of $Pb(Sc_{1/2}Nb_{1/2})O_3$ (PSN) and PSN–PT are quite high [75], the use of a flux environment is necessary for the crystal growth in order to lower the temperature limits. The previous work in our laboratory revealed that the mixture of $(PbO+\delta B_2O_3)$ is an effective solvent for the growth of the PMN–PT and PZN–PT piezocrystals because it combines the advantage of both the borate and PbO solvent [59, 62]. Therefore, we grew the 0.575PSN–0.425PT crystals using the high temperature flux technique based on the growth conditions established in our Lab. Table 4.1 lists the melting points of $Pb(Sc_{1/2}Nb_{1/2})O_3$ (PSN) [75], $PbTiO_3$ [105], PbO [106] and B_2O_3 [107].

Table 4.1: Melting points of $Pb(Sc_{1/2}Nb_{1/2})O_3$ (PSN), $PbTiO_3$, PbO and B_2O_3.

Compounds	Melting point
PSN	1425 °C
$PbTiO_3$	1285 °C
PbO	886 °C
B_2O_3	450 °C

High purity (>99.99%) powders of PbO, Sc_2O_3, Nb_2O_5, and TiO_2 were used as starting materials of PSN-PT. It is found that the two-step precursor method used in the ceramic synthesis is not necessary for the crystal growth. Therefore, stoichiometric mixtures of the starting powders of PSN-PT were directly used without the need of pretreatment. The chemicals were weighed according to the chemical reaction:

$$PbO+1/4(1\text{-}x)Sc_2O_3+1/4(1\text{-}x)Nb_2O_5+xTiO_2 \rightarrow Pb(Sc_{1/2}Nb_{1/2})_{(1\text{-}x)}Ti_xO_3 \qquad (4.1)$$

or

$$4PbO+Sc_2O_3+Nb_2O_5 \rightarrow 4Pb(Sc_{1/2}Nb_{1/2})O_3 \qquad (4.2)$$

A complex flux of ($PbO+\delta B_2O_3$) at various ratios (see Table 4.2 for details) was mixed with the "PSN–PT" powders and the mixture of 100 gram raw materials was loaded into a Pt crucible (35 ml). The mixture was ground for more than one hour and then premelted at a temperature around 900 °C. The Pt crucible was then placed in an alumina crucible that was sealed with an alumina lid using Al_2O_3 cement to prevent the evaporation of PbO, as shown in Figure 4.1 [59]. The loaded crucible was then put into a muffle furnace and heated to 1200 °C for PSN–PT crystals or 1300 °C for pure PSN crystals and soaked for 5 hrs. It was then slowly cooled down at a gradually increasing rate of 0.5 °C/h to 5 °C/h. Different lower limits of growth temperature (T_L), at which the slow cooling process was stopped, were used to study the temperature effects on the phase formation and the quality of the crystals. The typical temperature profile used in this work is shown in Figure 4.2 [59, 108]. The solidified flux was leached out with hot HNO_3 (2M) aqueous solution.

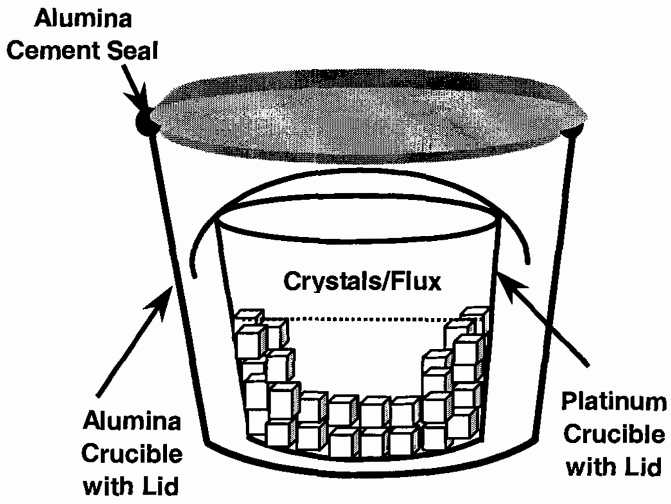

Figure 4.1: Pt and Al_2O_3 crucibles used in the growth of PSN-PT single crystals from high temperature solution (adapted from Dong and Ye [59]).

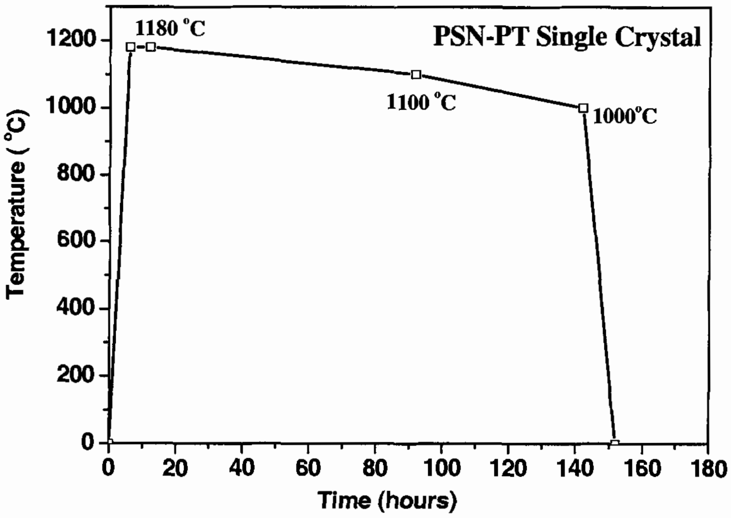

Figure 4.2: A typical thermal profile with gradually accelerated slow cooling for the PSN-PT crystal growth by high temperature solution method.

X-ray powder diffraction was performed on ground single crystals using a Rigaku diffractometer. The data were used to analyze the phase and symmetry of the grown crystals.

4.3.2 Results and Discussion

4.3.2.1 Effects of Growth Parameters on the Formation of Perovskite Crystals

Table 4.2 summarizes the various growth parameters and the results of the PSN–PT crystal growth. The crystals were nucleated and grown on the bottom and walls of the crucibles (Figure 4.3), probably due to heat dissipation through the walls of the container. The X-ray powder diffraction pattern in Figure 4.4 shows that the majority of the crystals grown exhibit the pure perovskite phase without impurities, i. e. the growth was dominated by the formation of the PSN–PT crystals. No distinguishable splits were found for the cubic $(100)_c$ and $(110)_c$ peaks, indicating a rhombohedral symmetry for the grown crystals. The rhombohedral split of the $(111)_c$ peak could not be observed by a conventional diffractometer due to the resolution limit, as in the case of PMN–PT and PZN–PT crystals.

Table 4.2: Summary of various growth parameters and growth results of the $(1-x)\mathrm{Pb(Sc_{1/2}Nb_{1/2})O_3} - x\mathrm{PbTiO_3}$ [PSNT] single crystals

Batch	Composition	Ratio of PSNT/Flux (mol%)	Ratio of PbO/B_2O_3 (mol%)	Lower limit temperature T_L for growth (°C)	Phase components (wt %)
1	x = 0.425	15/85	75/25	1000	100%Perovskite
2	x = 0.425	15/85	70/30	980	80%Perovskite +20%Pyrochlore
3	x = 0.425	25/75	70/30	1030	100%Perovskite
4	x = 0.425	25/75	70/30	1000	98%Perovskite + 2%Pyrochlore
5	x = 0	25/75	70/30	1080	98%Perovskite+ 2%Pyrochlore

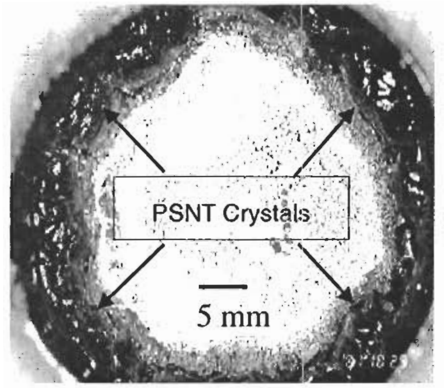

Figure 4.3: Top-view of an as-cooled crucible from Batch 4 of PSNT57.5/42.5 single crystal growth, showing the growth by spontaneous nucleation around the crucible walls.

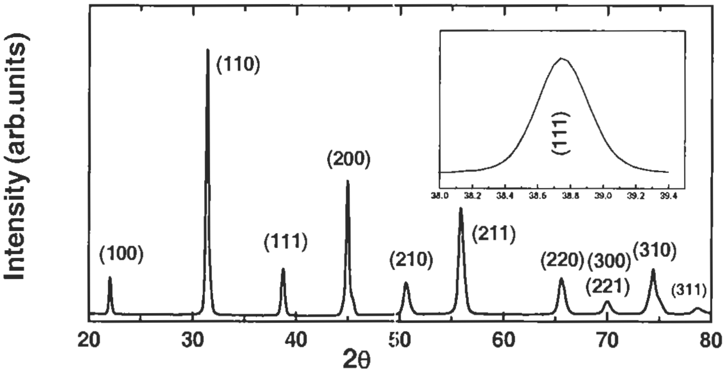

Figure 4.4: Powder XRD pattern of PSNT 57.5/42.5 single crystals

Crystals of the pyrochlore phase of the $Pb_{1.5}Nb_2O_{6.5}$-type were also found in some growth batches. Interestingly, the formation of the pyrochlore phase was found to depend on the lower limit of growth temperature T_L, below which the crystallization process is stopped, and the chemical compositions. In Batch 1, the pure perovskite phase grew in the temperature range above T_L = 1000 °C. In Batch 2, however, when the ratio of PbO/B_2O_3 was decreased while the ratio of PSNT/Flux remained the same as in Batch 1, a large portion (up to 20%) of the pyrochlore crystals appeared. In Batches 3, 4 and 5, the ratio of PSNT/Flux was increased while the chemical composition of the flux was kept the same as in Batch 2. Comparing Batches 3 and 4 with the same chemical composition, it can be seen that the formation of the pyrochlore phase took place below 1030 °C, and that ending the slow cooling process at 1030 °C has prevented the formation of the pyrochlore phase, thus leading to 100% perovskite crystals. In Batch 1, T_L was much lower than in Batch 3 and was the same as in Batch 4, but no pyrochlore phase crystals were found. This fact reveals that a higher portion of flux vs. solute and a larger ratio of PbO vs. B_2O_3 in Batch 1 have helped stabilize the perovskite phase down to a lower temperature. From the comparisons of Batches 1 and 2, we observe that a higher amount of B_2O_3 in the flux favours the formation of the pyrochlore phase. In other words, the pyrochlore phase may form at even higher temperature when the flux is richer in B_2O_3. In the growth of pure PSN crystals (Batch 5), the pyrochlore phase seemed to form at a higher temperature than for the PSN-PT crystals (Batch 4), probably due to the higher melting point of PSN.

If we consider PSNT57.5/42.5 – ($0.7PbO+0.3B_2O_3$) as a pseudo-binary system, it can be concluded from the above discussion that the primary growth of the perovskite PSN-PT crystals takes place in the composition range of PSNT/Flux =15/85 to 25/75 (molar ratio) within a certain temperature interval, as sketched by the dashed area in Figure 4.5, where Ts_1 and $Ts_{1'}$ represent the upper limit of the solidification temperature range for the perovskite phase, and Ts_2 and $Ts_{2'}$ indicate the upper limit of the temperature range in which the pyrochlore phase starts to form.

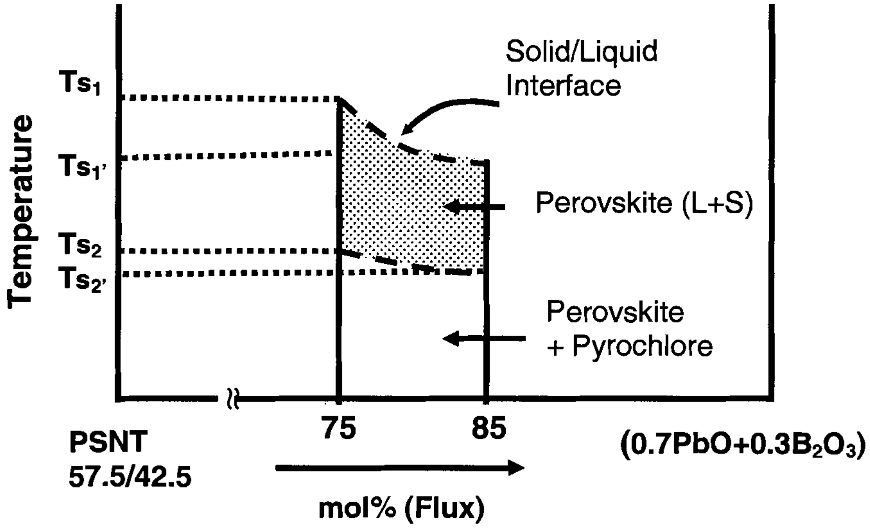

Figure 4.5: Schematic diagram showing the formation of the perovskite crystals (shaded area) in the pseudo-binary system of PSNT57.5/42.5 – $(0.7PbO+0.3B_2O_3)$

4.3.2.2 Effects of the PSNT/Flux and PbO/B_2O_3 Ratios on the Growth Thermodynamics

Table 4.3 lists the yields (percentages) of the crystallized PSN–PT perovskite crystals, which were calculated from the ratios of the amount (weight) of the grown PSN–PT crystals over that of the charged nominal PSN–PT powder in the stoichiometric composition in different batches.

Table 4.3 Summary of the yields of the grown $(1\text{-}x)Pb(Sc_{1/2}Nb_{1/2})O_3 - xPbTiO_3$ [PSN–PT] single crystals

Batch	*Yields of Grown PSNT Crystals (%)*
1	85 ± 5
2	22 ± 2
3	64 ± 2
4	62 ± 2

According to these data, we have constructed [109] in Figure 4.6 the possible variation of the yields (percentages) of PSN–PT single crystals, in (100-Yield%), vs. temperature for Batches 1, 2 and 4. Comparing Batches 1 and 2 that have the same PSNT/Flux ratio, we observe that in the same cooling temperature interval the yield of PSN–PT single crystals in Batch 2, which has a smaller ratio of PbO/B_2O_3, is dramatically decreased. In other words, an increase in the portion of B_2O_3 in the flux composition in Batch 2, with a fixed ratio of PSNT/Flux, decreases the percentage yields of crystallized PSN–PT in the same temperature range, corresponding to a relatively flat temperature curve, as shown in Figure 4.6. The effect of the chemical composition of the flux on the solubility of the solute was also observed in the growth of other crystals, for example, $Y_2Fe_5O_{12}$ [109].

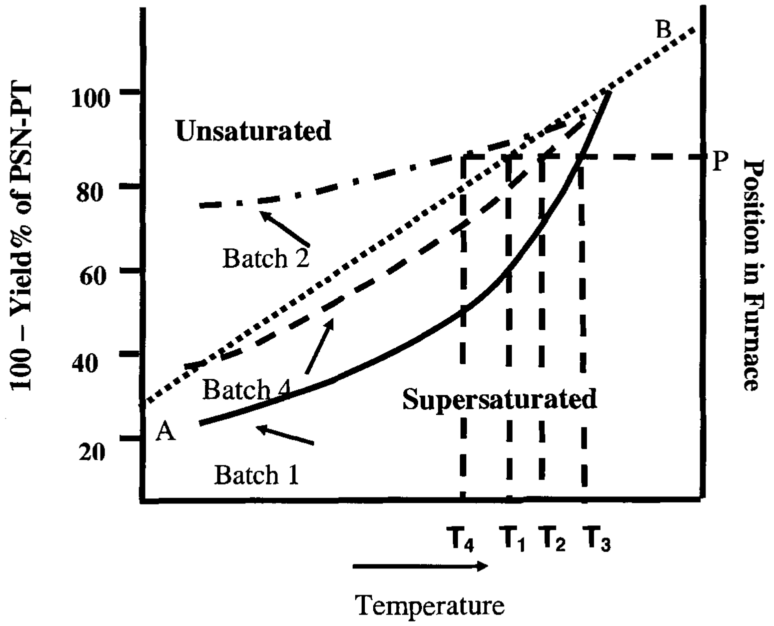

Figure 4.6: Schematic variation of (100-Yield%) of the grown PSN–PT single crystals vs. temperature. (T_1 – T_4: the crystallization temperature). Solid line: Batch 1 (T_3); Dash-dot line: Batch 2 (T_4); Long dash line: Batch 4 (T_2). Short dash line AB (T_1 for ideally crystallization temperature) represents the expected temperature gradient curve of the furnace.

When we increased the ratio of PSNT/Flux in Batch 3 and 4, while keeping the same ratio of PbO/B_2O_3 as in Batch 2, an increase in the yield of crystallized PSN–PT and hence in the slope of its temperature variation was observed. Therefore, by changing the chemical compositions, the slope of the variation of the yield of the grown PSN–PT crystals as a function of temperature can be appropriately adjusted to achieve a more stable growth, as discussed in the following.

In spontaneously nucleated growth, an appropriate supersaturation is required to trigger the formation of the nuclei. On the other hand, the habit of the crystal depends not only on its structure but also on the degree of the supersaturation, the temperature profile and the composition of environment [109], especially, when the growth takes place in polycomponent systems, e.g., [(PSN-PT) + flux] in this case, with a distribution constant k for a given component. Usually, at slow rates of growth, the distribution constant can be expressed as k_{eff} [110] i.e.:

$$k_{eff} = \frac{C_{s(act)}}{C_{l(act)}} \quad , \tag{4.3}$$

where k_{eff} is the effective-distribution coefficient, $C_{s(act)}$ and $C_{l(act)}$ are the actual concentrations in the solid and liquid phases. $C_{l(act)}$ is the "bulk" concentration in the liquid far enough from the growing interface that concentration gradients are negligible. The value of k_{eff} depends on the growth rate, the diffusion constant for the materials in the melt, and the width of the diffusion layer. For polycomponent systems, k_{eff} can be greater or less than one. The concentration gradient can be built up through the growing interface to the bulk concentration. If the temperature gradient is smaller, i.e. the melting point (or crystallization point) of the composition existing near the growing crystal as a function of distance, is encountered, constitutional supercooling may occur, in which the crystallization will tend to take place in front of the solid/liquid interface. Therefore, the following factors are important parameters to ensure stable growth: 1) the variation of the yield of the grown PSN–PT crystals as a function of temperature, which is related to the melting point of the PSN–PT compositions in the flux (i.e. the solubility); 2) the temperature gradient of the furnace. Constitutional supercooling may occur when the gradient of the melting point of PSN-PT in the corresponding flux is significantly larger than the temperature gradient of the furnace, leading to cellular structure and facets, or dendrite growth, which will be discussed in detail below.

4.3.2.3 Effects of the PSNT/Flux and PbO/B_2O_3 Ratios on the Growth Kinetics

To study kinetic factors affecting the growth of PSN–PT crystals, the morphology of PSN–PT crystals was carefully examined with respect to the growth conditions in each batch. The PSN–PT crystals show a pseudo-cubic form when grown on the crucible bottom, but a distorted form when grown on the walls. Figures 4.7(a) and (b) show a typical crystal plate cut from a bulk cubic crystal from Batch 1 and its sketch. It can be clearly seen that cellular growth structure was built in this crystal. In addition, a single nucleus is lying in the crystal as indicated in Figure 4.7(a). This suggests that the crystal was developed from a single nucleus and grown under stable conditions at the beginning. Then, the "ribbons" structure appeared and spread. Such a structure is typical of the earlier stage of the so-called "cellular structure" as described in Ref. [109]. The formation of the cellular structure implies that the growth was under severe constitutional supercooling conditions, in which the solid/liquid interface of growth could not adjust itself to keep in a planar surface shape, necessary for stable growth [110]. The "ribbon" structure in this crystal further developed into a hexagonal network in the final stage of the growth, indicating that the degree of supersaturation in the solution was even higher at the final growth stage. The formation of the cellular structure is illustrated in Figure 4.7(c) [110].

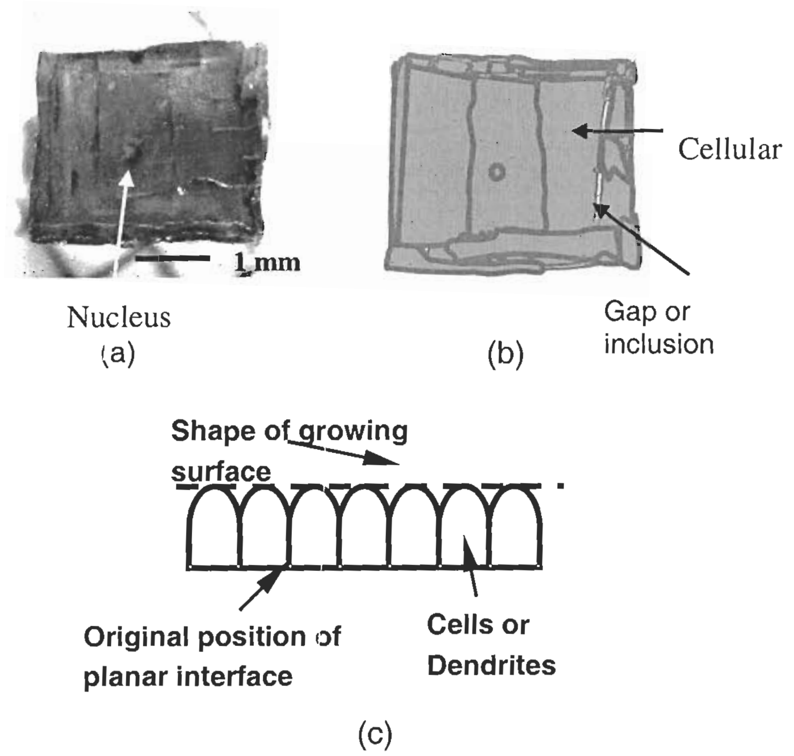

Figure 4.7: (a) A selected PSNT $(001)_{cub}$ crystal plate (thickness=620 μm) from Batch 1; (b) a sketch showing the cellular structure; (c) schematic of the formation of cellular or dendrite structure.

In Figure 4.6, the dashed AB line represents the expected temperature gradient of the furnace or the temperature gradient in the solution for the stable crystal growth to occur. We can establish a relationship between the variation of the yield of crystallized PSN–PT vs. temperature (e.g. the melting point of the composition) and the temperature gradient of the furnace. If we look at the growth position P at the furnace, the crystallization temperature (T_3) of PSN–PT in Batch 1 lay in front of the furnace temperature (T_1), i.e. $T_3 > T_1$. Because T_1 was well below T_3, the crystallization tended to take place in front of the solid/liquid surface, i.e. the crystallization started at temperature much high than that expected for the stable crystal growth, indicating the constitutional supercooling or high supersaturation occurring in this crystal growth process.

The best way to repress constitutional supercooling is to change the composition of the growth environment in order to adjust the melting point (or crystallization point) of the composition existing near the growing crystal as a function of distance to match with a fixed furnace temperature gradient. Accordingly, an increase in the portion of B_2O_3 was introduced in the flux in Batch 2, which was originally intended to lower the temperature coefficient of solubility. However, another problem, the so-called skeletons or dendrite growth (faceted growth), appeared, as shown in Figure 4.8.

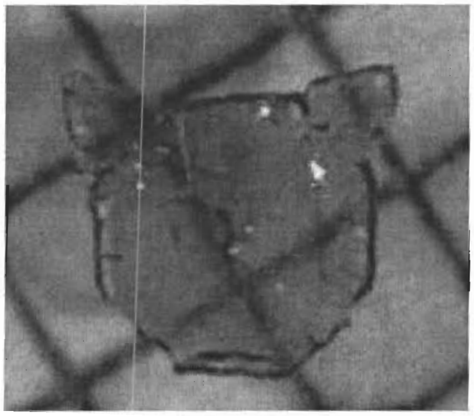

Figure 4.8: A selected crystal plate (thickness=90 μm, scale in mm) from Batch 2, showing the skeletons/dendrite structure.

It can be seen that the elongated-protrusion is along the $<111>_{\text{cubic}}$ direction and the tip of the primary arm of the dendrite appears to be round. The mechanism of the formation of the skeletons and dendrite structure has been well described by Chernov *et al.* in Ref. [109]. From Figure 4.8, we can assume that the crystal was first grown from a single nucleus and then developed into a relatively round shape. The initial stage in the loss of stability due to the convex form of solid/liquid interface gave rise to the skeleton/dendrite growth.

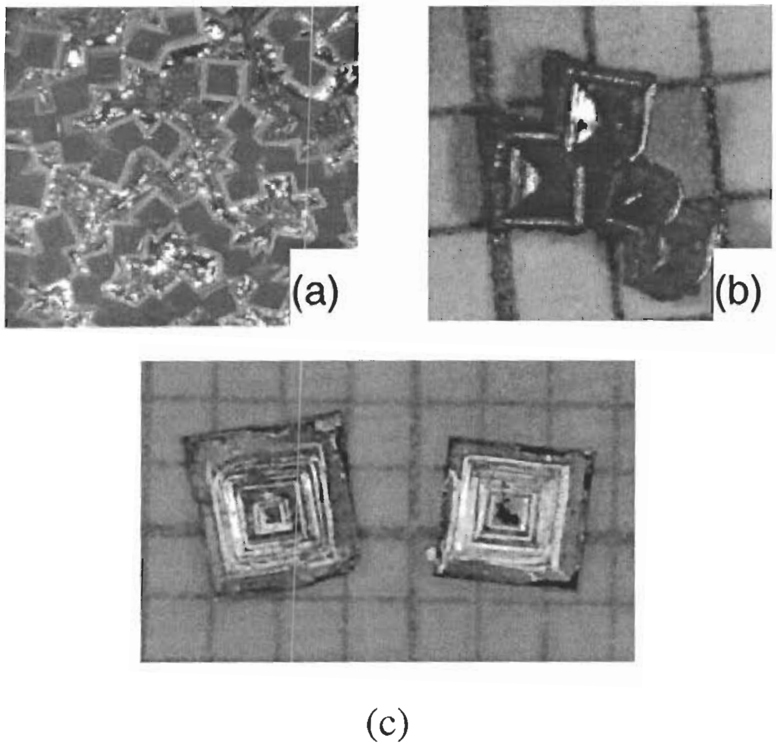

Figure 4.9: (a) As-grown crystals in the flux showing the branches of dendrites and cubic corner and edge connections; (b) and (c) Some selected crystals showing the concave surface on (100) face.

Figure 4.9 presents the morphology of smaller crystals formed at the center of the crucible (a), and some selected crystals after leaching out (b). Figure 4.9(a) shows that individual crystals tended to link with their neighbours through the corners, i.e. along $<111>_{\text{cub.}}$ or $<110>_{\text{cub.}}$ directions, which started in the very early stage of growth (probably just after nucleation). The crystals were connected to each other and formed the network. The concave shape at the center of crystals shown in Figure 4.9(b) also provides evidence that the growth proceeded on the convex form of the solid/liquid interface.

Using the Wulff construction [110], as shown in Figure 4.10, which is a polar plot of the crystal surface energy, we can explain the mechanisms of the connections between the crystal corners. From a surface free energy point of view, if we consider that the crystals first grew in a spherical shape, the distribution of concentration was isotropic. Therefore there was no faceted growth. But in reality the free energy of the crystals was anisotropic, i.e. OA > OB in Figure 4.10, and accordingly the growth rate at a certain face, e.g. the $\{111\}_{\text{cubic}}$ face, was greater than at the others. With any accidental perturbation, such as the changes of temperature, supersaturation, impurity content, etc [111], the fast growing face would be in the high-supersaturation area and would grow even faster. In principle, the greater the distance from the crystal center, the greater of the surface free energy. Hence, the $\{111\}_{\text{cubic}}$ faces of crystals were under critically unstable conditions and were energetically favored to grow.

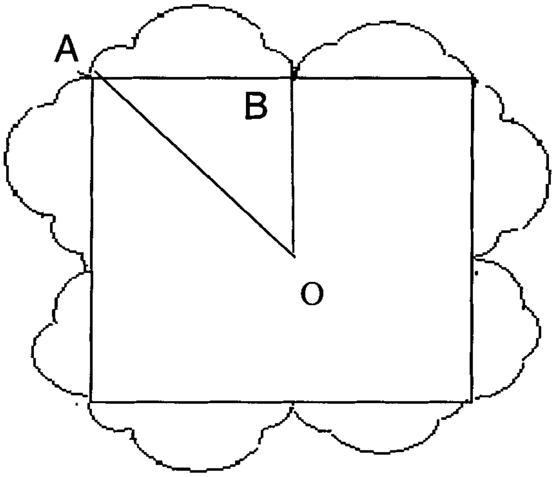

Figure 4.10: Wulff construction of the polar plot of crystal surface free energy

If we look again at the growth position *P* in Figure 4.6, the crystallization temperature (T_4) of PSN–PT in Batch 2 is below T_1. Accordingly, the crystallization in

Batch 2 occurred at a lower saturation and a lower concentration of PSN–PT in the same temperature interval compared to the other batches. We believe that the dendrite growth was mainly caused by the concentration difference between the corner and the center of the growing cubic crystals [112]. The instability of growth occurs when the supersaturation at the corner is too high, and the difference in the supersaturation between the corner and the center becomes too large to keep a constant normal growth rate over the flat surface. The observed distorted (convex) form of solid/liquid interface shape suggests that the corners were growing under a much higher supersaturation than the center, as seen in Figure 4.8. By adding the necessary amount of solute, i.e. by increasing the equilibrium concentration of PSN–PT in the solution, a more uniform distribution of concentration would be established to suppress the dendrite growth [109, 113]. Based on this consideration, we increased the ratio of PSNT/Flux in Batches 4 and some more growth batches of PSN or PSN–PT we performed later, which has resulted in a significant improvement both in the morphology and the quality of the grown PSN–PT crystals. No cellular or dendrite growth phenomenon was observed in these batches. Figure 4.11 shows selected crystals that exhibit pseudo-cubic morphology, indicating that an appropriate saturation was achieved at the solid/liquid interface and remained almost constant during the growth. In Figure 4.6, the solidification temperature (T_2) at position P for Batch 4 is located slightly in front of the temperature gradient, which, as expected, formed an appropriate saturation for a stable growth.

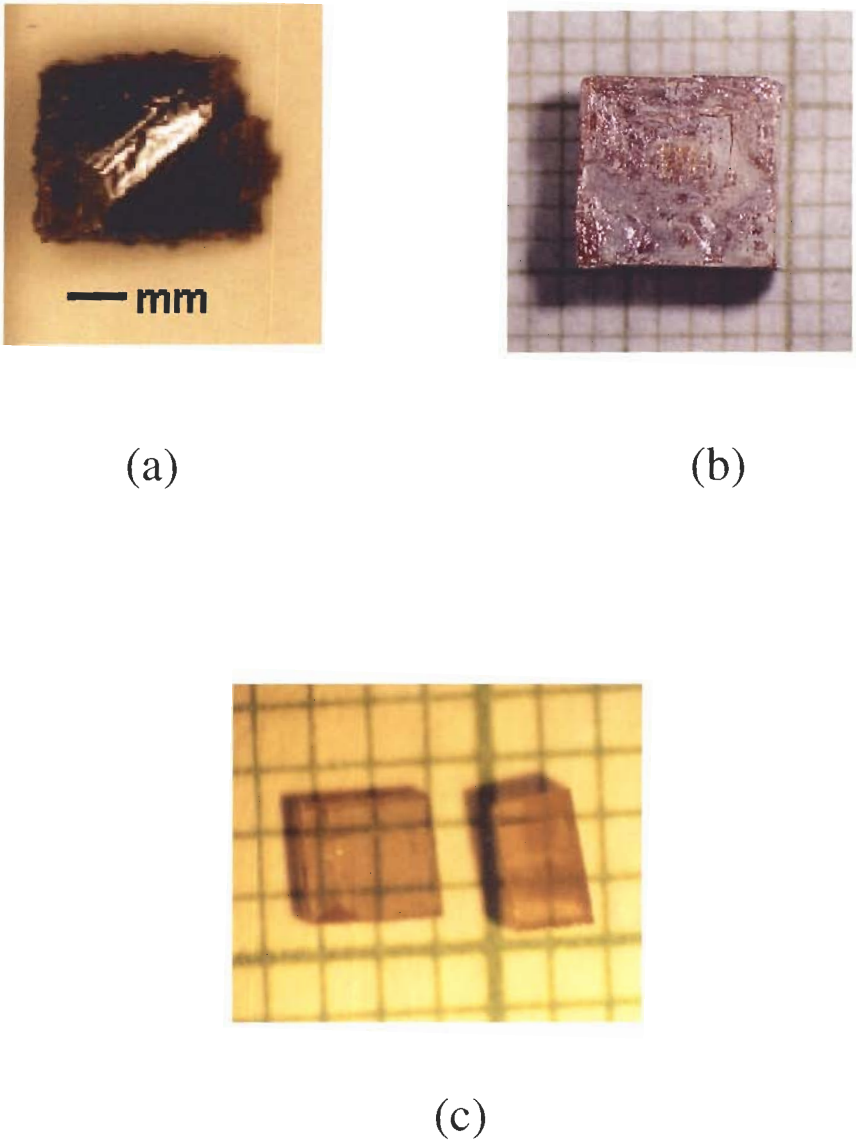

(a)

(b)

(c)

Figure 4.11:(a) and (b) Selected as-grown crystals of the PSN–PT, showing a regular morphology; (c) (001)-crystal plates cut from the bulk crystal.

4.3.3 Conclusions

The single crystals of perovskite $Pb(Sc_{1/2}Nb_{1/2})O_3$ and $(1-x)Pb(Sc_{1/2}Nb_{1/2})O_3-xPbTiO_3$ solid solution were grown by an improved flux method. The effects of the chemical compositions, such as the ratios of PSNT/Flux and PbO/B_2O_3, on the growth results were studied in terms of the growth thermodynamics and kinetics. They were found to strongly affect the morphology and quality of the grown crystals. The mechanisms of crystal formation were deduced from the growth kinetics. By appropriately adjusting the chemical compositions towards the optimum growth parameters, i.e. PSNT/Flux ≈ 25/75 and flux composition of $PbO/B_2O_3 \approx 70/30$, stable growth was achieved, leading to the formation of high quality PSN–PT crystals. We expect that the systematic study of the growth of PSN–PT single crystals will provide useful information for understanding the growth mechanisms of high quality piezo-/ferroelectric crystals, with excellent piezoelectric properties. The influence of growth conditions on the composition and the properties of the grown crystals will be studied in the following sections.

4.4 Electric Properties of $(1-x)Pb(Sc_{1/2}Nb_{1/2})O_3 - xPbTiO_3$ Single Crystals

4.4.1 Preparation of PSN–PT Crystals

For the dielectric, piezo- and ferroelectric measurements, crystal plates were cut with large surfaces parallel to the $(001)_{cub}$ plane. The $(001)_{cub}$ faces were mirror polished using a series of diamond pastes down to 3 μm, and sputtered with gold layers. Two gold wires were attached to each side of the $(001)_{cub}$ faces as connections to the electrodes using silver paste. The $(001)_{cub}$ platelet used for the measurements of the dielectric permittivity, hysteresis loops and strain loops is shown in Figure 4.12(a).The longitudinal electromechanical coupling factor k_{33} was determined by the measurements of the resonance (f_r) and antiresonance (f_a) frequencies for a <001>-oriented PSN–PT crystal rod. The dimensions of the rod are about 0.66x0.69x1.84 mm^3. It was pre-poled along the <100>$_{cub}$ direction by applying an electric field at 20 kV/cm at a temperature above 150 ^oC, and then cooled down to room temperature with electric field kept on. The rod crystal sample is shown in Figure 4.12(b).

The dielectric permittivity as a function of temperature at various frequencies (range from 10 to 100 kHz) was measured from 300 °C down to 10 ^oC at 2-3 ^oC intervals by means of an Alpha high-resolution dielectric/impedance analyzer (NovoControl). The stabilization of temperature was within 0.1 ^oC with an error of ±0.025 ^oC.

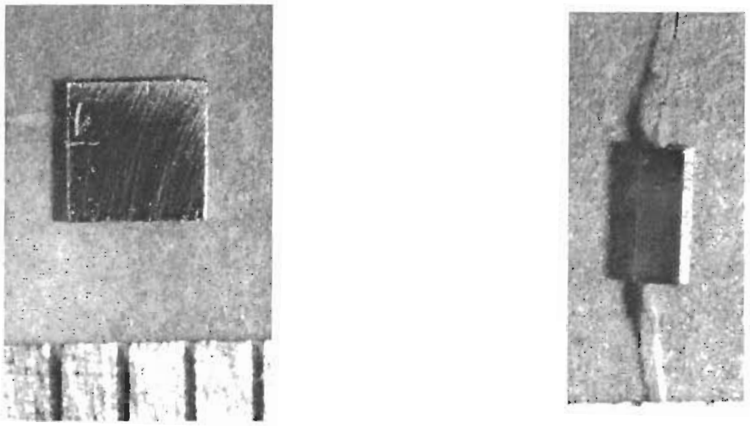

(a) (b)

Figure 4.12:a) PSN–PT (001)$_{cub}$ platelet covered with Au-layers on the both sides of (001)$_{cub.}$ faces as electrodes (scale in mm); b) <001>-oriented PSN–PT rod sample.

4.4.2 Results and Discussion

Figure 4.13 shows the temperature dependence of the real permittivity (ε′, or dielectric constant) at various frequencies of the (001)$_{cub}$ PSN–PT crystal platelet with nominal composition at $x = 0.425$. The dielectric constant shows a sharp peak at T_{max} = 213 °C, corresponding to the ferroelectric Curie temperature T_C, with a very high maximum value of 60,000. No frequency dispersion is found near the T_{max}, suggesting a normal ferroelectric behaviour and the good quality of the crystal. The temperature and frequency dependences of the dielectric permittivity are found to depend on the nominal compositions and the growth conditions. T_{max} varied from 207 to 227 °C for the PSN–PT crystals of nominal composition of $x = 0.425$. The detailed discussions about the effects of growth conditions on the dielectric permittivity behaviour will be presented in **Chapter 6**.

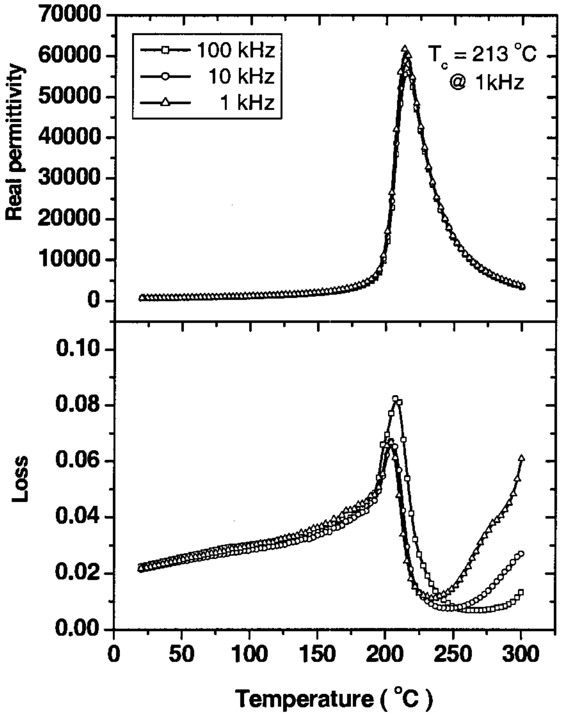

Figure 4.13:Dielectric permittivity of a (001)-oriented (1-x)Pb($Sc_{1/2}Nb_{1/2}$)O_3 – xPbTiO_3 single crystal with nominal composition $x = 0.425$.

The ferroelectric behaviour of the (001)-oriented PSN–PT sample is revealed by the well-developed polarization-electric field hysteresis loops measured at room temperature and shown in Figure 4.14. The saturation of the polarization is achieved at an electric field of ±10 kV/cm. Such a hysteresis loop with almost vertical lines indicates the sharp switching of macrodomain states in this crystal. Only slight depolarization occurs upon the removal of the electric field. The remnant polarization reaches $P_r \approx 25\ \mu C/cm^2$ under a bipolar drive of $E = \pm 12$ kV/cm with a coercive electric field of $E_C \approx 4$ kV/cm.

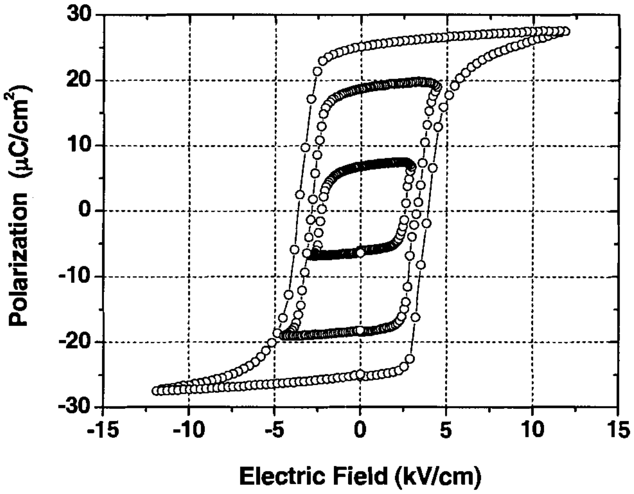

Figure 4.14:Polarization vs. electric field (P-E) loops for a (001)-oriented (1-x)Pb($Sc_{1/2}Nb_{1/2}$)O_3 – xPbTiO$_3$ (x = 0.425) single crystal.

Figure 4.15 shows the strain-electric field relation for the same <001>-oriented PSN-PT sample under a bipolar drive. A peak-to-peak strain value of 0.07% has been reached at $E \approx \pm 18$ kV/cm. The resonance (f_r) and antiresonance (f_a) frequencies for crystal at room temperature are found to be 767.7 and 1159.5 kHz at room temperature, respectively, as shown in Figure 4.16. A longitudinal electromechanical coupling factor k_{33} = 78% was obtained (see **Chapter 2,** Section 2.3 for details).

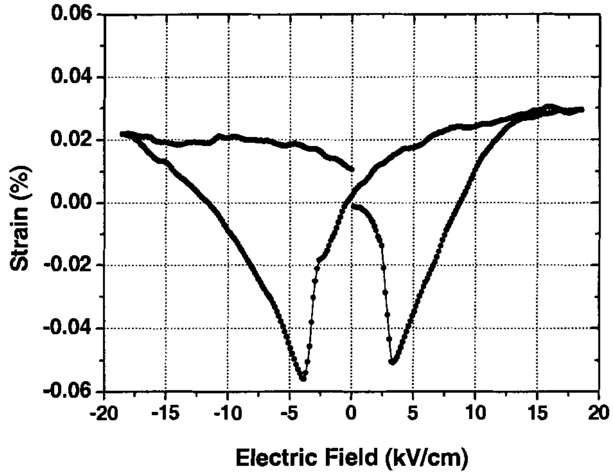

Figure 4.15:The bipolar strain vs. electric field for the <001>-oriented (1-x)Pb($Sc_{1/2}Nb_{1/2}$)O_3 – xPbTiO_3 (x = 0.425) single crystal.

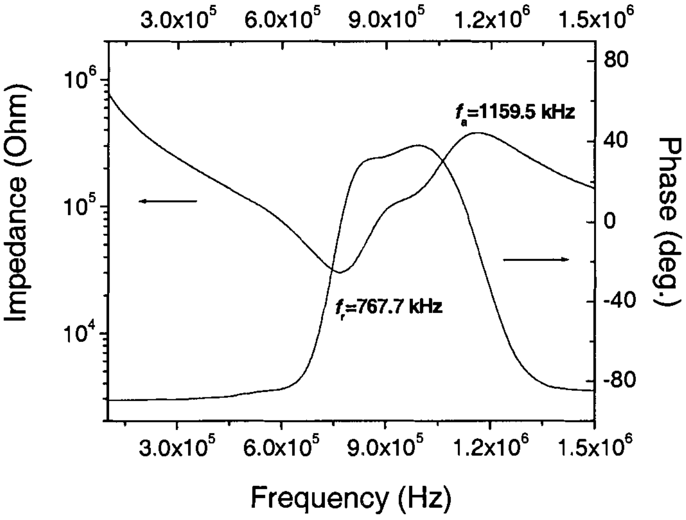

Figure 4.16:Impedance and phase as a function of frequency for a (001)-oriented (1–x)Pb($Sc_{1/2}Nb_{1/2}$)O_3 –xPbTiO_3 (x = 0.425) single crystal.

4.4.3 Conclusions

The (1-x)Pb($Sc_{1/2}Nb_{1/2}$)O_3 – xPbTiO_3 single crystals grown by the high temperature solution method show the typical ferroelectric behaviours, as revealed by the measurements of dielectric, ferroelectric and piezoelectric properties. However, the T_{max} (or T_C) for the PSN–PT single crystals with a nominal composition of $x = 0.425$ obtained from dielectric permittivity is lower than the T_C value expected for the same composition of the ceramics (see **Chapter 3**). According to the phase diagram established in Figure 3.13, the corresponding compositions for a T_C in the range of 207–227 °C should be $0.26 < x < 0.33$. This indicates that composition segregation occurred during the crystallization of the solid solution compound. This problem has also been encountered in the growth of PMN–PT crystals, as well as in many solid solution systems. The high temperature phase diagram of PMN–PT solid solution was recently established by Jean Gao in our Laboratory [114] and indicates that the separation of the solidus and liquidus lines can explain this segregation problem. Since the melting point of PSN (>1425 °C) is higher than $PbTiO_3$, we can expect a qualitatively similar phase segregation phenomenon to appear, giving rise to the same trend, i.e. the composition of grown PSN–PT crystals should contain a lower concentration of $PbTiO_3$ than the nominal composition of $x = 0.425$. We have also noticed that although the bipolar strain value and the longitudinal electromechanical coupling factor k_{33} are comparable with those of PZT ceramics (see **Chapter 9** for details), they are lower than those reported in PMN–PT and PZN–PT single crystals of the MPB composition. This rather mediocre piezoelectric performance of the PSN–PT crystals can be mainly attributed to the fact that the actual composition of grown crystals departed from the charged MPB one, as explained above.

The comparison of the piezoelectric properties of the PSN-PT single crystal with those of PZT ceramics, PZN-PT and PMN-PT single crystals will be discussed in **Chapter 9.**

Chapter 5:
Spontaneous Transformation from Relaxor to Ferroelectric Macro-domain State in $Pb(Sc_{1/2}Nb_{1/2})O_3$ Single Crystals

In this chapter, the phase transitions of $Pb(Sc_{1/2}Nb_{1/2})O_3$ single crystals have been studied by means of dielectric spectroscopy, differential scanning calorimetry (DSC) and domain observations.

5.1 Abstract

The studies of $Pb(Sc_{1/2}Nb_{1/2})O_3$ (PSN) and $(1-x)Pb(Sc_{1/2}Nb_{1/2})O_3 - xPbTiO_3$ (PSN-PT) single crystals revealed that the chemical and physical properties of the materials are affected by the growth conditions. The PSN crystals that grew at temperatures below 1200 °C show a spontaneous phase transition, upon cooling, from the paraelectric to a relaxor, then to a normal ferroelectric state. The domain observation of the same PSN sample confirmed the existence of macro domain state with possible rhombohedral symmetry at room temperature. However, the PSN crystal grown at higher temperatures (above 1200 °C) exhibits a much broader dielectric peak, and the transition from relaxor to normal ferroelectric is suppressed.

5.2 Introduction

To provide useful information for understanding the mechanisms of relaxor ferroelectric behaviour, the role of the chemical order/disorder of the B-site cations in the diffuse phase transition of relaxor perovskites has been studied in many compounds. Setter and Cross [17] first studied this phenomenon in $Pb(Sc_{1/2}Ta_{1/2})O_3$ (PST) single crystals with different degrees of ordering on the B-site controlled by suitable thermal annealing. It was found that the dielectric properties of the disordered PST crystals exhibit typical relaxor ferroelectric properties while the ordered crystals of the same composition show a classical sharp transition like a normal ferroelectric. Viehland *et al.* [18] studied the complex susceptibility of PST for the samples with varying degrees of long-range chemical ordering and proposed that the polarization fluctuations condensed into a ferroelectric state in highly ordered samples, while freezing into a glass-like state in partially ordered samples. The same behaviour was also studied in other compounds, such as $Pb(Sc_{1/2}Nb_{1/2})O_3$ [15, 115], and $Pb(In_{1/2}Nb_{1/2})O_3$ and $Pb(Yb_{1/2}Nb_{1/2})O_3$ [20].

It was found that for the lead-based complex perovskites, the order/disorder depends both on the valence and ionic radii differences of the two cations on the B-sites. Ye [11] summarized three scenarios for the possible structures: 1) the chemical differences between B′ and B″ are large enough for the cations to order so as to form a superstructure; 2) the chemical differences between B′ and B″ are close to the critical limit for B-site disorder/order occupancy so that it is possible to modify the degree of ordering by appropriate thermal annealing, quenching or crystal growth conditions; 3) the complex compounds $Pb(B'_{1/3}B''_{2/3})O_3$ with smaller chemical differences usually exhibit a long–range disordered occupancy.

$Pb(Sc_{1/2}Nb_{1/2})O_3$ (PSN) is a unique $A(B'B'')O_3$ complex perovskite compound with 1:1 ratio for B′:B″. The chemical differences between B′ and B″, e.g. differences in the charge and ionic radius of Sc^{3+} (r = 0.745Å) and Nb^{5+} (r = 0.64 Å), are close to the critical limit for B-site disorder/order occupancy. Consequently, the degrees of ordering of the B-site cations can be varied by the thermal treatments or crystal growth conditions. This phenomenon was initially investigated by Stenger [14] and Setter and Cross [16]. Stenger found that the order-disorder transition in PSN takes place at 1210 °C and PSN has a rhombohedral symmetry at room temperature with the unit cell parameters, a_0 = 4.080(1) Å and α = 89.89(1) ° [14]. The ordered structure was revealed by the appearance of the (111) and (311) reflections in the X-ray diffraction spectrum due to a superlattice structure. In the ordered form of PSN, the scandium and niobium ions alternate in adjacent B-sites, forming two interpenetrating sublattices and giving rise to an effective doubling of the primitive unit cell. Therefore, the X-ray diffraction pattern for the ordered PSN is characterized by the appearance of superlattice reflections corresponding to half-integer spacing of the disordered structure. The structure of the ordered perovskite $Pb(Sc_{1/2}Nb_{1/2})O_3$ is sketched in Figure 5.1.

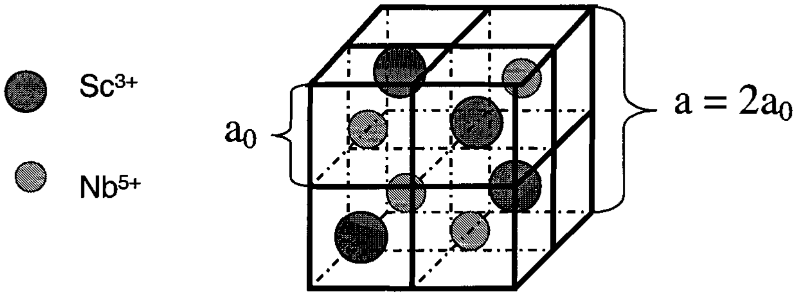

Figure 5.1: Sketched structure of ordered perovskite $Pb(Sc_{1/2}Nb_{1/2})O_3$ (Pb^{2+} and O^{2-} ions are omitted).

The study of the disordered $Pb(Sc_{1/2}Ta_{1/2})O_3$ and $Pb(Sc_{1/2}Nb_{1/2})O_3$ ceramics by Chu *et al.* [78] by means of permittivity measurements has demonstrated that upon zero-field cooling, a spontaneous transformation from a relaxor state to a ferroelectric state takes place when the lead vacancies are suppressed. This behaviour is different from that of other relaxors like PMN and PZN, in which such a transition can be observed in their dielectric properties only under the application of an electric field. The macroscopic ferroelectric domains were confirmed by the measurements of polarization hysteresis loop and by transmission electron microscopy (TEM). On the other hand, the introduction of a certain amount of Pb-vacancies leads to the broadening of the dielectric peak with frequency dispersion down to low temperature, typical of relaxor behaviour.

The spontaneous relaxor to ferroelectric phase transition in $Pb(Sc_{1/2}Nb_{1/2})O_3$ was only studied in the ceramic form, probably due to the lack of high quality $Pb(Sc_{1/2}Nb_{1/2})O_3$ single crystals (PSN has a high melting point of 1425 °C). As mentioned above, different growth conditions may affect the ordered/disordered state in PSN. Therefore, it is interesting to investigate the chemical and physical properties of PSN single crystals prepared by different growth conditions. Further more, single crystals allow the domain observation, which is useful for the investigation of the ferroelectric domain state. In this work, PSN single crystals have been prepared under different growth conditions, namely different chemical environments and growth temperatures. Single crystals with a highly ordered state or a highly disordered state have been grown. The phase transitions associated with different ordered or disordered states have been studied by means of differential scanning calorimetry (DSC), dielectric spectroscopy and domain examination.

5.3 Experimental

The experimental procedure for the growth of PSN single crystals has been described in **Chapter 4**. The PSN single crystals were prepared under two different chemical environments and growth temperature ranges. The growth conditions and the specification of PSN single crystals studied are summarized in Table 5.1.

Table 5.1: Growth condition and specification of PSN single crystals.

Growth Batch	PSN-A	PSN-B
Composition	$Pb(Sc_{1/2}Nb_{1/2})O_3$	$Pb(Sc_{1/2}Nb_{1/2})O_3$
Growth Method	Solution	Solution
PbO : B_2O_3 (mol%)	80:20	70:30
Flux : PSNT (mol%)	80:20	75:25
Growth Temperature (°C)	1180 – 1100	1260 – 1080
Slow Cooling Time (hour)	80	128
Crystal Color	Yellow	Yellow
Size (mm)	~ 2.5	~ 3

The ordered/disordered structures were studied by conventional X-ray powder diffraction (XRD) (Philips), for which the crystals were crushed and ground into fine powder to eliminate any preferential orientations. The domain structure of the PSN single crystals was examined by a polarization light microscope (Olympus BX60). The sample for domain observations was cut with large surfaces parallel to the $(100)_{cub}$ plane and mirror polished using a series of diamond pastes down to 3 μm. After domain observations, the same sample was used for the measurements of the dielectric permittivity as a function of temperature at various frequencies by means of an Alpha High-Resolution Dielectric/Impedance Analyzer (NovoControl). The heat flow of PSN single crystals (bulk samples of ~75 mg) was measured as a function of temperature using a differential scanning calorimeter (DSC6200, Seiko Exstar)

5.3.1 XRD Spectra

Figure 5.2 shows the XRD patterns of PSN–A and PSN–B. Both spectra reveal a pure perovskite phase. The PSN-B crystal shows the superlattice reflections of (111) and (311) at two-theta of 18.88 ° and 36.5 °, respectively, indicating an ordered perovskite structure, while the PSN–A crystal shows no superlattice peaks, indicating a disordered structure. The order parameter S can be calculated by dividing the ratio of the experimentally observed superlattice reflection intensity, in this case (111), over the fundamental reflection intensity from a parallel plane, (222), by the corresponding ratio for a perfectly ordered sample, that is [14, 16]:

$$S^2 = \left(\frac{I_{111}}{I_{222}}\right)_{exp.} \Big/ \left(\frac{I_{111}}{I_{222}}\right)_{S=1} \qquad (5.1)$$

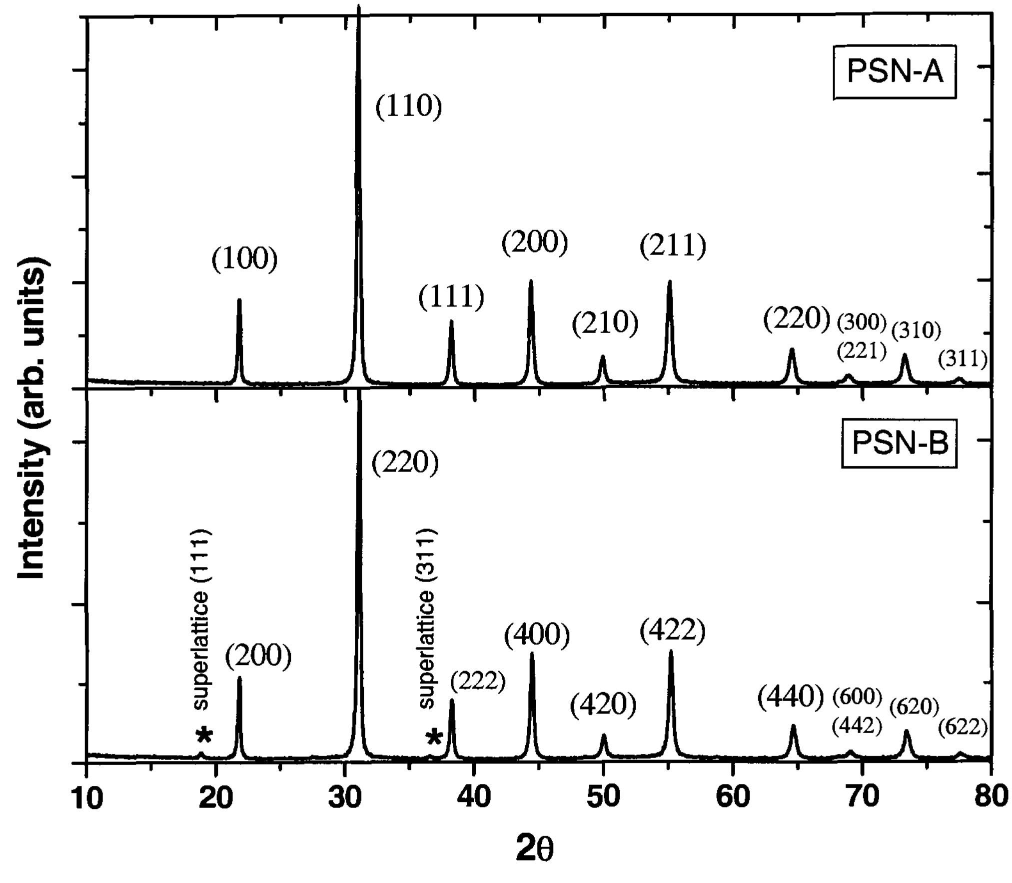

Figure 5.2: Powder X-ray diffraction patterns of $Pb(Sc_{1/2}Nb_{1/2})O_3$ single crystals (PSN-A and PSN-B).

Stenger and Burgraaf [14] assumed that through a long annealing process (i.e., annealed at 940 °C for more than 3000 hours) the PSN ceramic sample completely transforms it into the ordered state. Upon this assumption, the ratio of I_{111}/I_{222} for a perfectly ordered PSN ceramic was calculated to be 0.12. This value is higher than the theoretical value of 0.103 for a complete order. They considered that this discrepancy is due to the fact that both the (111) and (222) reflections were measured with the same receiving slits, which may give the reflection at the higher diffraction angle an intensity that is relatively too low. Interestingly, the ratio of I_{111}/I_{222} measured for the PSN–B crystal is about 0.16, i.e. even higher than that of the ceramics. We suspect that the ordering structure in the ceramic is not as perfect as that in the single crystals, probably due to the other effects, such as the size of grains, the grain boundary and a relatively lower density. This high order parameter S indicates a highly ordered structure for the PSN–B single crystal.

5.3.2 Dielectric Permittivity Measurements

Figure 5.3 displays the temperature dependences of the real and imaginary parts of dielectric permittivity for the PSN–A and PSN–B crystals measured at the frequencies of 0.1, 1, 10, 100 kHz. Upon cooling, a maximum permittivity was observed at temperature $T_{max,}$ which is 104 °C for the real part and 99 °C for the imaginary part (at 1 kHz) for PSN–A, and 37 °C for the real part and 28 °C for the imaginary part for PSN–B. Both samples show the frequency dispersion with T_{max} shifting to a high temperature as frequency increases, suggesting the typical relaxor ferroelectric behaviour. In the PSN–A crystal, the maximum value of the dielectric constant (ε_{max}) reaches 50,000 (at 100 Hz). A remarkable sharp drop of the permittivity can be observed in PSN–A in both real and imaginary parts at the same temperature T_C = 97 °C accompanied by a strong attenuation of the frequency dispersion. The permittivity peak of PSN–B is, however, much broadened and it does not undergo a sharp change. In addition, the magnitudes of permittivity peak are much smaller compared with PSN–A.

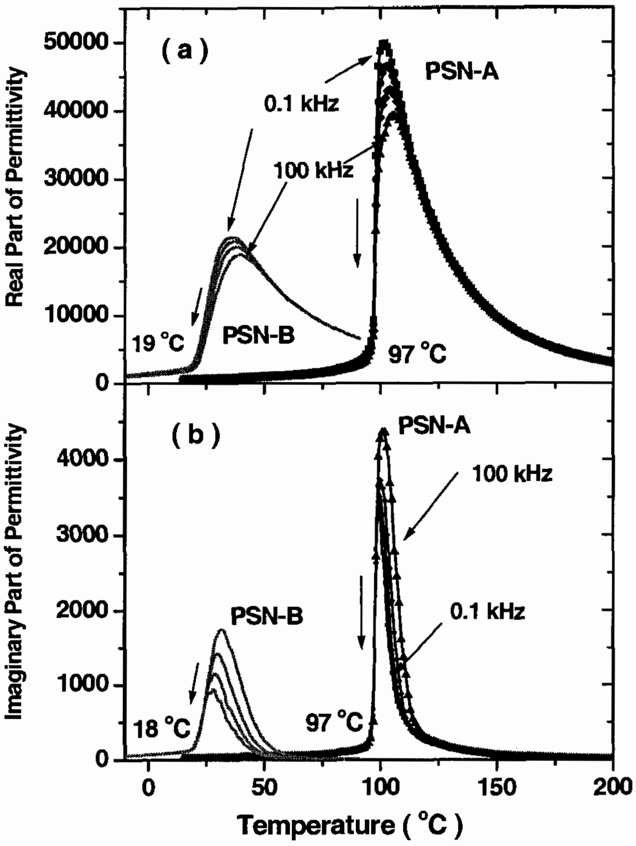

Figure 5.3: Real (a) and imaginary (b) parts of permittivity of $Pb(Sc_{1/2}Nb_{1/2})O_3$ single crystals (PSN–A and PSN–B), as a function of temperature (upon cooling) at the frequencies of 0.1, 1, 10, and 100 kHz.

5.3.3 Calorimetric Analysis

Differential Scanning Calorimetry (DSC) analysis was carried out on both PSN–A and PSN–B crystals and the results are shown in Figure 5.4. PSN–A exhibits a sharp anomaly at 98 °C in the variation of heat flow as a function of temperature, in good agreement with the temperature T_C at which the sharp decreases of dielectric permittivity occurs. For PSN–B, however, the anomaly peak is much broadened and the corresponding onset temperature is slightly lower than T_C found in the dielectric measurements.

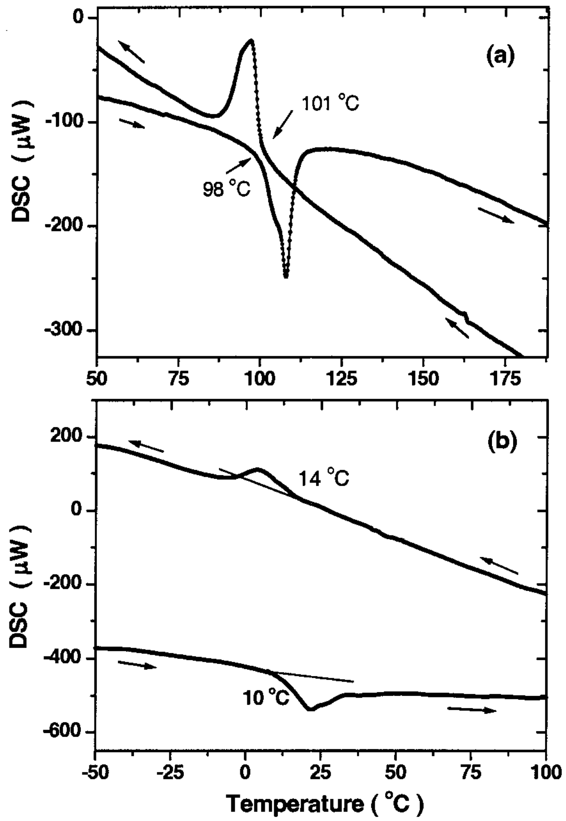

Figure 5.4: Differential scanning calorimetry (DSC) measurements of Pb(Sc$_{1/2}$Nb$_{1/2}$)O$_3$ single crystals, (a): PSN–A; (b): PSN–B, upon heating and cooling.

5.3.4 Domain Observations

The domain structure and its evolution as a function of temperature in both PSN–A and PSN–B single crystals have been observed and examined by PLM between -180 °C and 250 °C. Figure 5.5 shows the domain structure and phase transition of the PSN–A single crystal. The domain structure at room temperature (Figure 5.5a) is composed of fine birefringent domains, indicating a macro domain state for the (001) plate of PSN–A. In Figure 5.5b, the sample was rotated in such a way that the <001>$_{\text{cub.}}$

direction forms an angle of 45 ° with the directions of the crossed polarizers. It can be seen that under this configuration, most areas of the crystal are in extinction, indicating a rhombohedral symmetry at room temperature. A sharp phase transition takes place upon heating at T_C around 111 °C with the domain walls moving rapidly from the centre to the crystal edges, as shown in Figure 5.5c. After the transition ($T > T_C$), the crystal shows a full extinction at any angles under crossed polarizers (not shown), in agreement with the cubic symmetry. The birefringent domains reappeared upon cooling through T_C. Figure 5.5d shows the domain pattern at room temperature, which is slightly different from the one before heating.

Similar domain structure and phase transition were observed in the PSN–B crystal, as shown in Figure 5.6. The macro domain state with the rhombohedral symmetry was observed for PSN–B at room temperature. The phase transition into the cubic phase already started at room temperature. However, some kinds of behaviour different from PSN–A are revealed by domain analysis: 1) At room temperature, PSN–B already shows full extinction in some areas, indicating the presence of the cubic (C) phase together with the rhombohedral (R) phase. The crystal transforms completely into the R-phase at about 10 °C upon cooling. 2) The phase transition in PSN–B is very diffuse and spread out in a temperature interval of 10 to 57 °C, which seems to be associated with fluctuations in local structures and chemical compositions. 3) Almost the same domain pattern recalls when cooling down to room temperature, suggesting that the domain configuration is affected by the local environment, e.g. local defects and Pb-vacancies (see **Section 5.2.7** for discussion).

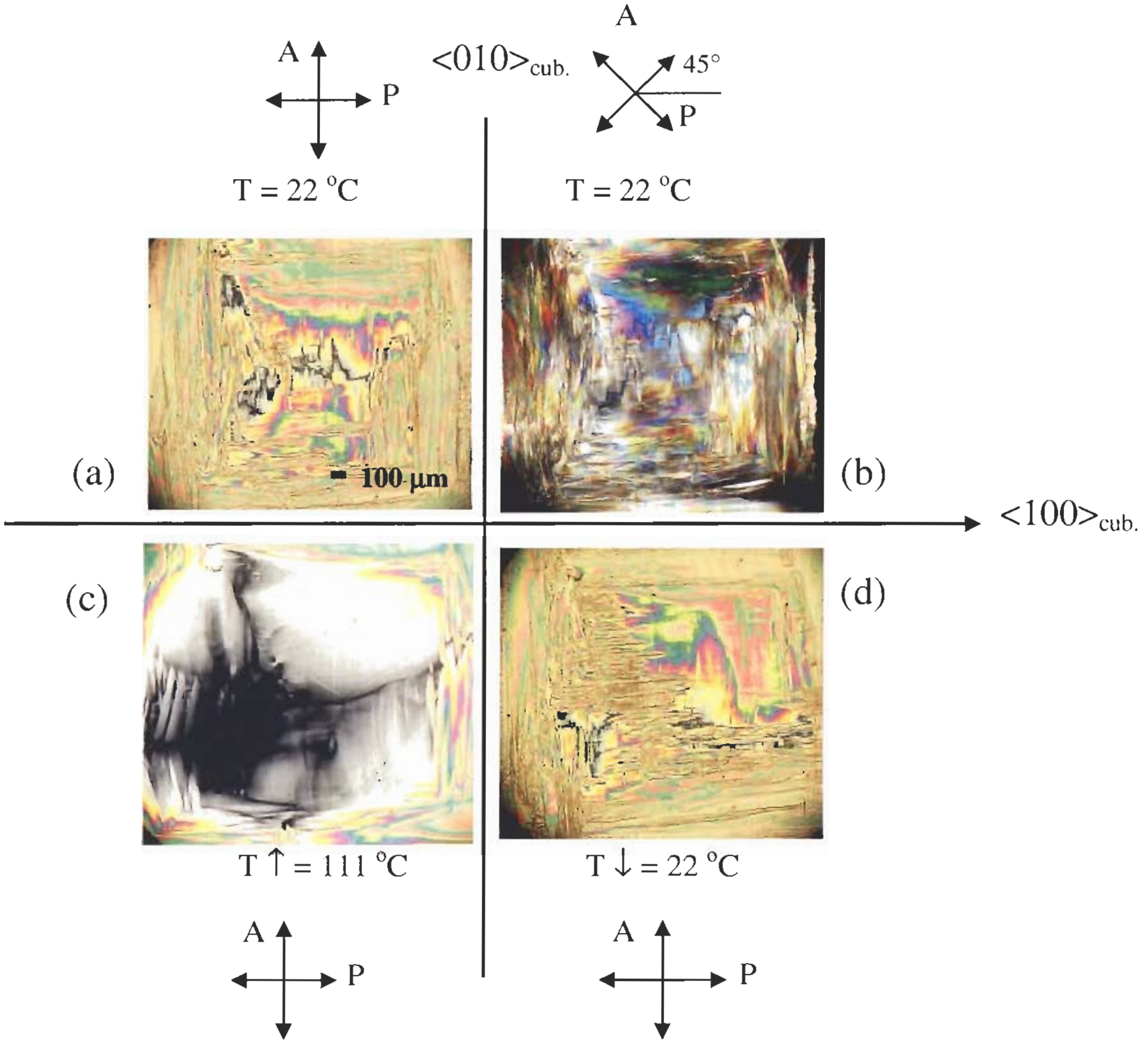

Figure 5.5:Domain structure and phase transition of the $(001)_{cub.}$ PSN–A single crystals under polarization light microscopy. (a) and (b): at room temperature before heating; (c) at phase transition temperature upon heating; (d) at room temperature upon cooling.

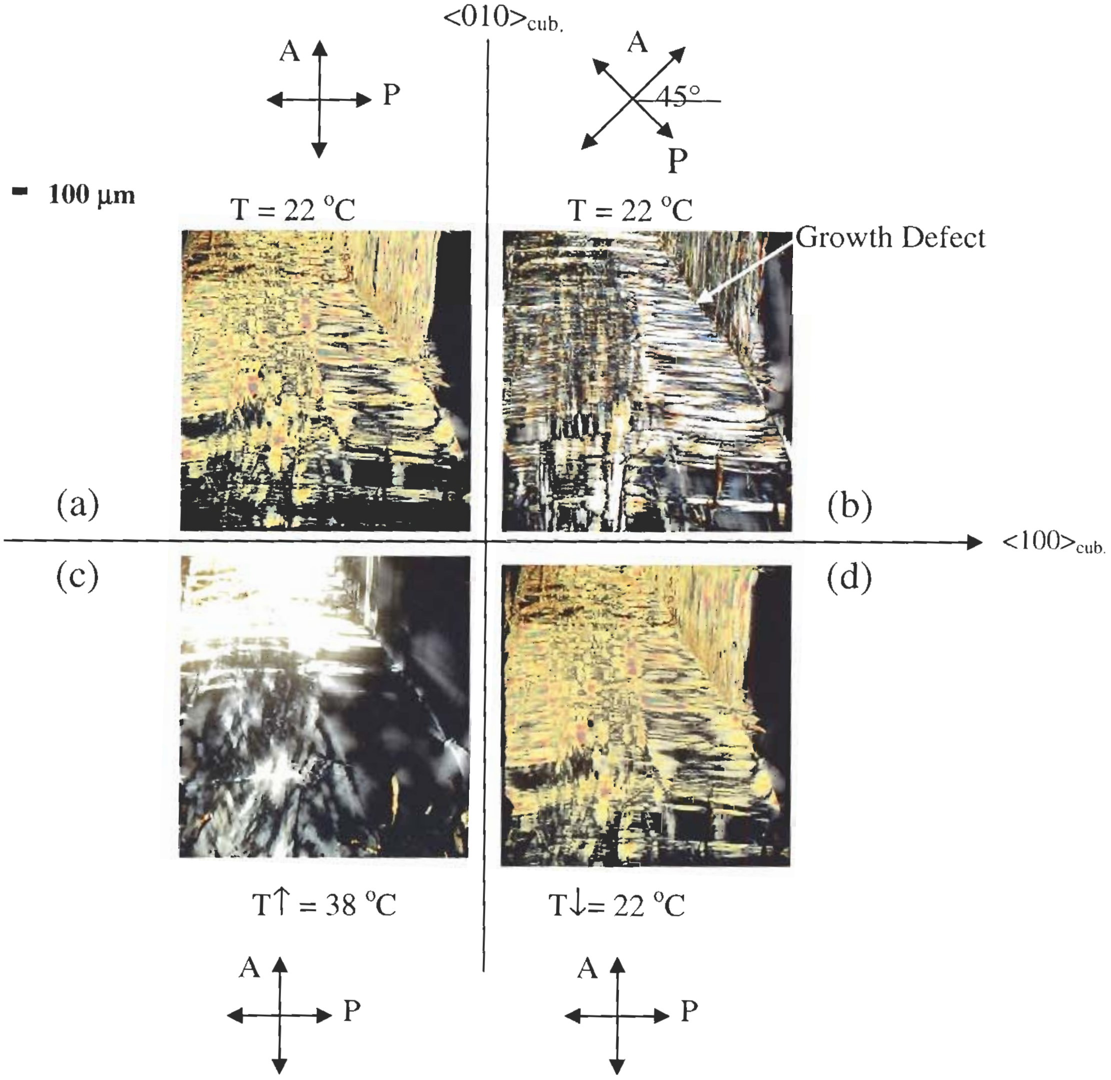

Figure 5.6: Domain structure and phase transition of the $(001)_{cub}$ PSN–B single crystal under polarization light microscopy. (a) and (b): at room temperature before heating; (c): at phase transition temperature upon heating; (d) at room temperature upon cooling.

5.4 Discussion

The above results show that different growth conditions (Table 5.1) exert significant effects on the degrees of ordering, the dielectric permittivity, the thermal properties, and the domain structure and the phase transition of the grown PSN crystals. It is believed that in the growth process of complex perovskite $Pb(B'_{1/2}B''_{1/2})O_3$ crystals, the disordered structure is formed first [20]. In other words, both the PSN–A and PSN–B crystals were grown initially in the form of disordered state. The PSN–B crystals were grown starting from temperatures above the order-disorder transitions temperature (T_o). As the crystallization proceeds with temperature decreasing slowly (about 1-5 °C/h) through the T_o, the crystals have enough time to transform from a non-equilibrium disordered state to an equilibrium ordered state through the cation diffusion process. From this point of view, it is understandable that the PSN–B crystals exhibited an ordered structure. Usually, the ordered PSN is associated with a sharp phase transition in dielectric permittivity, as observed in the PST crystals [17, 18]. However, this is not the case in the PSN–B crystals, in which a diffused phase transition was revealed by dielectric, DSC and domain studies.

On the other hand, the phase transition temperature was reported to be 78 °C for highly ordered PSN ceramics and 109 °C for disordered PSN ceramics by dielectric measurements [15]. Thus, the phase transition temperature of the PSN–B crystal is lower than that expected for ordered PSN. The possible explanation for these discrepancies is the existence of a certain amount of lead/oxygen vacancies and some other defects in the PSN-B crystals. The high growth temperature, long crystallization process and high portion of B_2O_3 in the flux are believed to promote the formation lead/oxygen vacancies.

The effects of Pb vacancies on the dielectric properties of PST and PSN ceramics were studied by Chu *et al.* [116, 117]. It was found that a certain amount of Pb vacancies can suppress the formation of macro ferroelectric domains and bring the materials into a typical relaxor state. Another effect of Pb vacancies is to lower the phase transition temperature. It was reported that 1.7 at. % of Pb vacancies in the disordered PSN ceramics shifts the phase transition temperature of the disordered stoichiometric PSN ceramics by about 15 °C. Moreover, the phase transition phenomena studied in both PSN–A and PSN–B single crystals under high hydrostatic pressure [118] indicate that at high pressures both the PSN–A and PSN–B single crystals behave as a pure relaxor, completely extinguishing the ferroelectric phase. Both the phase transition temperature and the magnitude of dielectric peak decrease with increasing pressure, broadening the temperature range of the relaxor state. The mechanism of this effect is still under investigation. Nevertheless, the defect formation caused by hydrostatic pressure is believed to induce the relaxor state at the expenses of the ferroelectric phase. The domain structure of the PSN–B crystals indicates that the phase transition first starts around the corner where the growth defect was formed (Figure 5.6b). The full recovering of domain pattern upon cooling (Figure 5.6d) suggests that the development of domains structure is governed by local defects, resulting in similar domain configurations. In a model discussing local structural distortion with special concern of $Pb(Sc_{1/2}Nb_{1/2})O_3$, Bokov [119] also concluded that the broadening of the phase transition is caused by vacancies, interstitial atoms, dislocations and other extended defects. Therefore, the broadening of dielectric peak with strong frequency dispersion observed in the ordered PSN–B crystal can be attributed to the lead/oxygen vacancies and related defects.

In contrast, the PSN–A crystals exhibit the typical character of a disordered structure, similar to that reported for the disordered PSN ceramics with a stoichiometric Pb content [116]. The dielectric permittivity shows clear frequency dispersions at T_{max}, typical of relaxor behaviour. The sharp decrease in dielectric permittivity immediately below T_{max} corresponds to the spontaneous relaxor to ferroelectric phase transition. It is noticed that the temperature difference (ΔT) between the peak temperature (T_{max}) and the phase transition temperature (T_C) is more than two times smaller in the PSN-A crystal ($\Delta T \approx 6$ °C) than in the disordered PSN ($\Delta T = 15$ °C) ceramics. We believe that the smaller ΔT results from the high quality and high stoichiometric Pb content of the PSN–A crystal with a high degree of disorder. The relatively low growth temperature (<1200 °C) suppressed the possible ordering process through ion diffusion. As a result, the PSN–A crystal retain in a disordered state. The sharp peak in DSC measurement and the rhombohedral domain structure observed at room temperature strongly support the conclusion on the spontaneous transformation from the relaxor state to the macroscopic ferroelectric phase in the PSN–A single crystals.

5.5 Relaxor Behaviour of the Disordered $Pb(Sc_{1/2}Nb_{1/2})O_3$ Single Crystals

The dispersive dielectric relaxation prior to the spontaneous phase transition (upon cooling) in the PSN–A single crystal characterizes the relaxor behaviour. In classical relaxors, strong frequency dispersion is observed on the low-temperature slope of the dielectric maximum. At T_{max}, at which the dielectric maximum occurs, an empirical relationship, i.e. Vogel-Fulcher (V-F) relationship [120, 121], can be used to analyze the frequency dependence of the temperature of the dielectric maximum in analogy to the magnetic relaxation in spin-glass systems [23]. The Vogel-Fulcher relationship can be expressed as:

$$f = f_0 \exp[-E_a/(T_{max}-T_f)] \quad , \tag{5.2}$$

where f_0, E_a, and T_f are the fitting parameters, f is the measurement frequency and T_{max} is the temperature of the dielectric permittivity maximum. T_f was initially described as a static freezing temperature, at which the system freezes into a frustrated state. However, the study of the spontaneous relaxor to ferroelectric transition in $Pb(Sc_{1/2}Ta_{1/2})O_3$ ceramics [19] revealed that T_f is very close to the T_C, at which the sharp decrease in permittivity occurs. It was concluded that in the case of PST, T_f does not necessarily the mean a freezing point, rather an indication of the onset of the relaxor to ferroelectric phase transition, i.e., $T_f = T_C$. The same phenomenon was also studied in $Pb(Sc_{1/2}Nb_{1/2})O_3$ ceramics [78].

In normal ferroelectrics, the Curie-Weiss law is known to describe the high temperature slope of the permittivity peak. In relaxors, however, a deviation from the Curie-Weiss law is observed at the temperature up to the several hundreds degrees above the T_{max}. It was recently found by Bokov and Ye [30] that in $0.75PbMg_{1/3}Nb_{2/3}O_3$ – $0.25PbTiO_3$ relaxor ceramics a single shape parameter, δ, is good enough to describe the permittivity in a wide temperature range above T_{max} using a quadratic law, i.e.:

$$\frac{\varepsilon_A}{\varepsilon} = 1 + \frac{(T - T_A)^2}{2\delta_A^2} \quad , \tag{5.3}$$

where T_A ($< T_{max}$) and ε_A ($> \varepsilon_{max}$) are the parameters defining the temperature position of the peak and the extrapolated value of ε at $T = T_A$, respectively, and they should be independent of the frequency of measurements. The parameter δ_A, being practically independent of frequency, can be considered as a convenient measure for the degree of diffuseness of the permittivity peaks in relaxors. It was demonstrated [31] that the data for a large number of materials with different broadness of $\varepsilon(T)$ maximum can be collapsed perfectly onto a single scaling line with this quadratic law.

In this section, we demonstrate that the dielectric permittivity of the disordered $Pb(Sc_{1/2}Nb_{1/2})O_3$ single crystals satisfies the Vogel-Fulcher relationship at T_{max} and the quadratic law in a certain temperature interval at $T > T_{max}$.

5.5.1 Vogel Fulcher Analysis

Figure 5.7 displays the Vogel-Fulcher fitting of the real part of permittivity for the disordered $Pb(Sc_{1/2}Nb_{1/2})O_3$ (PSN-A) single crystal. As we can see, in the frequency range of 1.86×10^5 to 36.4 Hz, the data can be well fitted into the Vogel-Fulcher relationship with the parameters of $f_0 = 1.27 \times 10^9$ Hz, $E_a = 0.0065$ eV and $T_f = 371.8$ K, respectively. However, the same parameters cannot fit the data in the low frequency range (26 – 0.36 Hz). It is suspected that the deviation from Vogel-Fulcher relationship in the low frequency range is due to the closeness of T_{max} at low frequency to the T_C. It is also noticed that T_f is approximately the same as T_C (~ 370 K), corresponding to the temperature at which the sharp drop of permittivity occurs. Table 5.2 lists the Vogel-Fulcher fitting parameters for the real part of permittivity of $Pb(Sc_{1/2}Nb_{1/2})O_3$ (PSN–A) crystal, which are compared with the data of $Pb(Sc_{1/2}Nb_{1/2})O_3$ ceramic [116]. The differences of fitting parameters between PSN crystal and ceramics are not large. They can be due to the different degrees of compositional order. This result is in good agreement with the conclusion made from the temperature difference (*ΔT*) between the peak temperature (T_{max}) and the phase transition temperature (T_C) of the dielectric permittivity between the PSN crystal and ceramics (**Section 5.2.7**). The Vogel-Fulcher fitting could not be performed for the imaginary part of permittivity, probably due to the proximity of T_{max} and T_C.

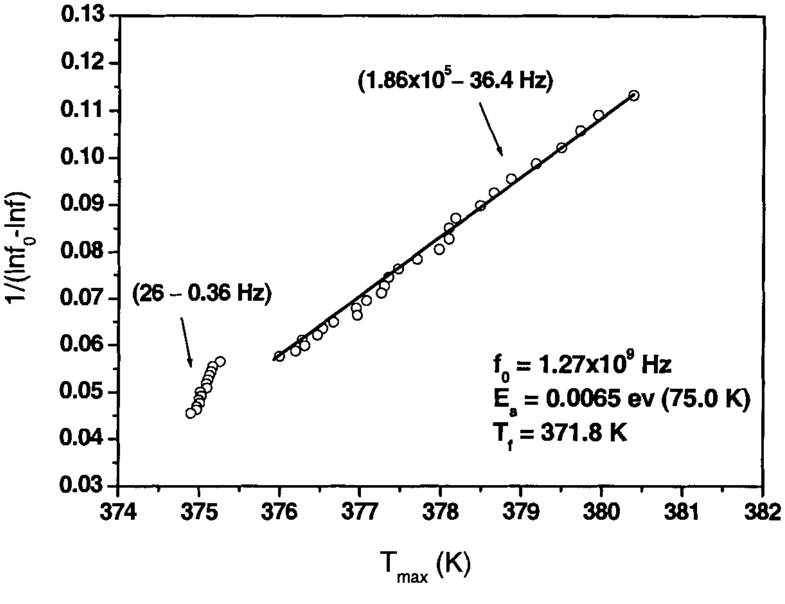

Figure 5.7: Vogel-Fulcher fitting of the real part of permittivity of $Pb(Sc_{1/2}Nb_{1/2})O_3$ (PSN–A) crystal

Table 5.2: Comparison of the Vogel-Fulcher fitting parameters for the real part of permittivity of the $Pb(Sc_{1/2}Nb_{1/2})O_3$ (PSN–A) crystal (this work) and of the $Pb(Sc_{1/2}Nb_{1/2})O_3$ ceramics (*Ref.* [116])

Parameters	PSN-Crystal	PSN ceramics
f_0 (Hz)	1.27 x 10^9	4.4 x 10^9
E_a (eV)	0.0065	0.014
T_f(k)	371.8	376

5.5.2 Quadratic Law Analysis

As in many relaxor ferroelectric materials [30, 31], the dielectric permittivity as a function of temperature in the high temperature range of the disordered $Pb(Sc_{1/2}Nb_{1/2})O_3$ crystal have been analyzed by the quadratic law of Eq. (5.3) with the fitting parameters of $\varepsilon_A = 4.2 \text{ x } 10^4$, $T_A = 370.4$ K, and $\delta_A = 21.6$ K. Figure 5.8 illustrates the quality of fitting for the selected frequencies, $f = 1$, 10, and 100 kHz. The fact that the plot of $\log_{10}[(\varepsilon_A/\varepsilon) - 1]$ versus $\log_{10}(T - T_A)$ lies perfectly on a single straight line confirms the validity of Eq. (5.3) with the same parameter δ_A for all the frequencies. As we can see in Figure 5.8, the quadratic law is valid in the temperature range of 388 – 528 K. The deviation from the linear behaviour below the lower temperature limit may be due to the different contributions, e.g. universal relaxor contribution, to the dielectric relaxation as temperature approaches T_{max} [30]. No deviation has been observed in the high temperature end, implying that the quadratic law (Eq. 5.3) is valid in an even wider temperature range. No clear signs indicate the validity of Curie-Weiss law in the temperature range up to 528 K, which is 150 °C above the T_{max}. This confirms the pure relaxor behaviour in the highly disordered $Pb(Sc_{1/2}Nb_{1/2})O_3$ single crystal.

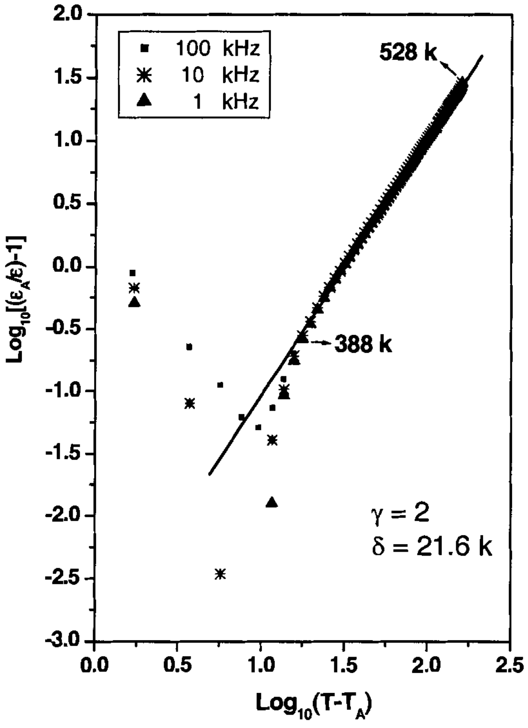

Figure 5.8: Quadratic law fitting of the real part of permittivity for the disordered $Pb(Sc_{1/2}Nb_{1/2})O_3$ (PSN–A) crystal.

5.6 Conclusions

The studies of $Pb(Sc_{1/2}Nb_{1/2})O_3$ (PSN) single crystals revealed that the chemical ordered/disordered structure and physical properties of the materials are affected by the growth conditions. The PSN crystal that was grown below 1200 °C shows a disordered B-sites structure, while the PSN crystal grown at higher temperatures (above 1200 °C) exhibits a highly ordered B-sites structure revealed by the appearance of the superlattice structure in XRD spectrum.

The study of the phase transitions by dielectric spectroscopy and domain structure analysis have revealed that the spontaneous transition from the relaxor state to the ferroelectric macrodomain state takes place (upon cooling) both in the ordered and disordered $Pb(Sc_{1/2}Nb_{1/2})O_3$ crystals. The relaxor characters still persist in disordered PSN single crystal at and above T_{max}, as demonstrated by the Vogel-Fulcher relationship and the quadratic law. The dielectric permittivity of the disordered $Pb(Sc_{1/2}Nb_{1/2})O_3$ single crystal exhibits typical relaxor characters, i.e., the frequency dispersion of dielectric permittivity follows the Vogel – Fulcher relationship in a certain frequency range, and the high-temperature slope of the permittivity peak follows the quadratic law in a wide temperature range. An interesting observation is that the T_C, T_f and T_A are approximately the same. This supports the conclusion of Ref. [19] that the T_f is not necessarily a freezing temperature of the relaxor system; rather it is the temperature at which the relaxor to ferroelectric phase transition takes place. The diffuseness parameter δ_A from the quadratic law fitting is smaller than that in the prototypical relaxor ferroelectric PMN and PZN [31], reflecting the nature of the sharp phase transition in the disordered $Pb(Sc_{1/2}Nb_{1/2})O_3$ single crystal. This issue will be further discussed in **Chapter 9** (Section 9.4).

Chapter 6:
Phase Symmetry and Phase Sequences of the (1-x)Pb($Sc_{1/2}Nb_{1/2}$)O_3 – xPbTiO_3 Single Crystal with Composition near or within Morphotropic Phase Boundary

Section 6.4 of this chapter is a revised version of the paper published in **Materials Science and Engineering B** by **Y. -H. Bing, and Z. -G. Ye**, (*Mater. Sci. Eng. B*) 2005 (in press). The use of this article is permitted by the publisher of Elsevier, Science Direct (Home websites: http://www.elsevier.com)

In this chapter, the effects of growth condition on (1-x)Pb($Sc_{1/2}Nb_{1/2}$)O_3–xPbTiO_3 single crystals have been studied by means of dielectric properties and domain observations. The phase symmetry and phase transition sequences have been discussed in (1-x)Pb($Sc_{1/2}Nb_{1/2}$)O_3 – xPbTiO_3 single crystals with composition within morphotropic phase boundary based on the analysis of X-ray diffraction data and dielectric permittivity measurements.

6.1 Abstract

The studies of the (1-x)Pb($Sc_{1/2}Nb_{1/2}$)O_3 – xPbTiO_3 (PSN–PT) single crystals reveal that the chemical and physical properties of the materials are affected by the growth conditions. By the measurements of the dielectric constant as a function of temperature (upon cooling), it is found that crystals grown from the same charged stoichiometric composition (x=0.425), but under different flux environments (i.e. the composition of flux and the flux to PSN–PT ratios are varied), show anomalies (phase

transitions) at different temperatures. This phenomenon is attributed to the complex local chemical structure of the PSN-PT solid solution single crystals with random occupancy of three different cations (Sc^{3+}, Nb^{5+}, and Ti^{4+}) on the B-site. The domain structure and phase transition in PSN-PT crystals are also studied.

6.2 Introduction

The most important family of relaxors is the complex perovskites $A(B'B'')O_3$, in which the B-site is randomly occupied by the two different cations B′ and B″. When a relaxor $A(B'B'')O_3$ combines with $PbTiO_3$, a normal ferroelectric, to form the solid solution, a more complicated situation appears in terms of local chemical structure. With the increase of Ti^{4+}-concentration, a morphotropic phase boundary (MPB) generally appears. The materials with compositions close to the MPB usually give rise to enhanced piezo- and ferroelectric properties and an even more complex chemical and physical behaviour.

Compared with $Pb(Sc_{1/2}Nb_{1/2})O_3$, the solid solution of $(1-x)Pb(Sc_{1/2}Nb_{1/2})O_3-xPbTiO_3$ (PSN-PT) presents a more intricate situation due to the introduction of an additional cation (Ti^{4+}) on the B-site. As discussed in **Chapter 3**, when the concentration of Ti^{4+} increases, an MPB is reached at $0.35 \leq x < 0.50$ with $240\ ^{\circ}C \leq T_C < 290\ ^{\circ}C$. It is expected that the different distributions of cations play an important role for the properties of the MPB materials, such as domain structure, phase transition and dielectric permittivity. In this section, we investigate the domain structure and dielectric properties of PSN-PT single crystals prepared under different growth conditions.

6.3 Experimental Procedures

PSN-PT single crystals were grown by the high temperature solution method using (PbO + δB_2O_3) as flux. The different batches of (1-x)PSN–xPT crystals were grown with the same charged stoichiometric composition ($x = 0.425$), but under different growth conditions, namely, the ratios of PSNT to Flux and PbO to B_2O_3 are slightly different. Detailed descriptions of the growth of PSN–PT single crystals have been given in **Chapter 4** (Section 4.1).

The ordered/disordered structures were studied by X-ray powder diffraction. The domain structure of the PSN–PT single crystals was investigated by polarized light microscopy (Olympus BX60) at room temperature. The same sample for the domain studies was used for the dielectric measurements afterwards. The dielectric permittivities were measured as a function of temperature at various frequencies by means of an Alpha High Resolution Dielectric/Impedance Analyzer (NovoControl),

6.4 Effects of Growth Conditions on the Domain Structure and Dielectric Properties of $(1\text{-}x)Pb(Sc_{1/2}Nb_{1/2})O_3 - xPbTiO_3$ Single Crystals

Table 6.1 summarizes the various conditions used for the growth of PSN–PT [or PSNT] crystals in three batches. We also grew the PSN-PT single crystals by a modified Bridgman method and compared the properties with the PSN-PT crystals grown by high temperature solution method. The powder X-ray spectra indicate a clean perovskite structure for all the three PSN–PT samples. No peak of an ordered structure was detected.

Table 6.1: Growth conditions for the $(1\text{-}x)\mathrm{Pb}(\mathrm{Sc}_{1/2}\mathrm{Nb}_{1/2})\mathrm{O}_3 - x\mathrm{PbTiO}_3$ single crystals (x= 0.425)

Growth Batch	PSNT-A	PSNT-B	PSNT-C
Growth Method	Solution	Solution	Modified Bridgman
PbO : B_2O_3 (mol%)	70:30	80:20	80:20
Flux : PSNT (mol%)	75:25	75:25	80:20
Growth Temperature (°C)	1180	1160	1140
Excess PbO : PSNT (%wt.)	1.5:1	1.7:1	2.27:1
Crystal Colour	Brown	Yellow	Yellow
Crystal size (mm)	5	5	10

Figure 6.1 shows the temperature dependence of the dielectric constant for PSNT–A, PSNT–B and PSNT–C measured upon cooling at frequencies of 0.01, 1 and 100 kHz. As one can see, the peaks of dielectric constant for the three different samples appear at different temperatures 227 °C for PSNT–A, 213 °C for PSNT–B and 207 °C for PSNT–C (at 1 kHz) with frequency dispersion. PSNT–A shows the highest T_{max} and its dielectric constant peaks are broadened. As the temperature decreases below T_{max}, the dielectric constant drops continuously without abrupt slope change. Compared with PSNT-A, the permittivity peak occurs at lower temperatures in PSNT-B and PSNT-C while the magnitude of the dielectric maxima increase, reaching 67,500 (at 1 kHz). Upon further cooling, the dielectric constant drops more sharply, especially for PSNT-C, and a

sudden slope change is observed at 195 °C for PSNT-B and 190 °C for PSNT–C, respectively. Around these temperatures, the frequency dispersion of dielectric constants is significantly attenuated.

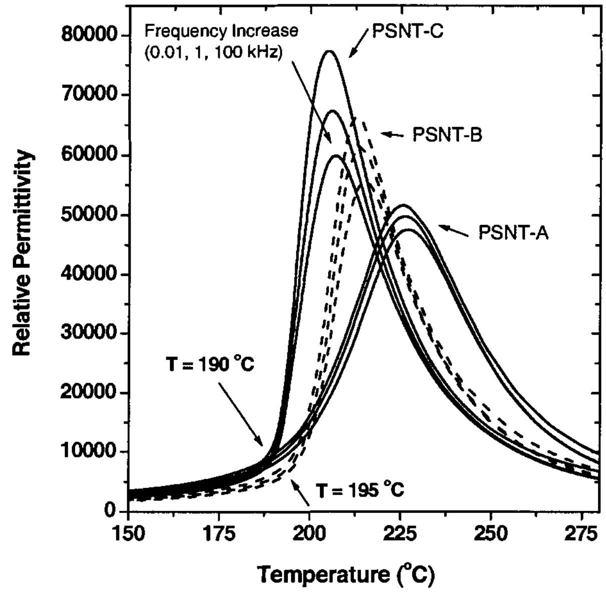

Figure 6.1: Variation of the real part of permittivity as a function of temperature at frequencies of 0.01, 1 and 100 kHz for different (001)-oriented (1-x)Pb($Sc_{1/2}Nb_{1/2}$)O_3 – x$PbTiO_3$ (x = 0.425) single crystals, PSNT–A, PSNT–B and PSNT–C (see Table 6.1).

According to the revised MPB phase diagram of (1-x)PSN–xPT ceramics in Figure 3.13 (**Chapter 3**), the dielectric maximum for the composition of 57.5PSN–42.5PT is expected to appear around T_C = 270±5 °C, corresponding to the ferroelectric/paraelectric phase transition. However, all the three crystal samples show a T_{max} (in the range of 207–227 °C) lower than the T_C, which corresponds to the composition of $0.26 < x < 0.33$. The decrease in T_{max} in the PSN–PT crystal studied can be attributed to three possible reasons: 1) the deviation of composition from the nominal (weighed) composition (x = 0.425) to a lower content of PT, which occurred during the crystal growth due to phase segregation, 2) the effect of different degrees of order/disorder in the structure; 3) possible growth defects (including lead/oxygen vacancies).

As discussed in **Section 5.2.7,** PSN with a high degree of order shows a lower T_{max} [15] and disordered PSN with a certain amount of lead vacancies displays the typical relaxor behaviour with a lower T_{max} as well [116]. In contrast, the disordered PSN with a stoichiometric composition shows a higher T_{max} and a spontaneous transformation from the relaxor state to the macroscopic ferroelectric phase, giving rise to a sharp decrease of the dielectric constant upon cooling [116].

In the case of the PSNT–B and PSNT–C, the frequency dispersion around T_{max} reveals the typical relaxor behaviour, and the sharp decrease of dielectric constant indicates the spontaneous phase transition from the relaxor state to the ferroelectric phase, the same as seen in the disordered PSN. This phenomenon implies that PSNT–B and PSNT–C exhibit the similar features to the stoichiometric and disordered PSN. In other words, the PSNT–B and PSNT–C crystals, with the presence of Ti^{4+}, show a highly disordered structure, which is consistent with the X-ray spectra. In addition, the PSNT–B and PSNT–C crystals are expected to have a low level of lead/oxygen vacancies since they were grown from a flux containing a high ratio of PbO-excess and at a relatively lower temperature (Table 6.1). The lower T_{max} obtained in PSNT–B and PSNT–C could result from a lower Ti-concentration due to phase segregation commonly occurred in the growth of solid solution crystals (see Section 4.2.2, **Chapter 4**).

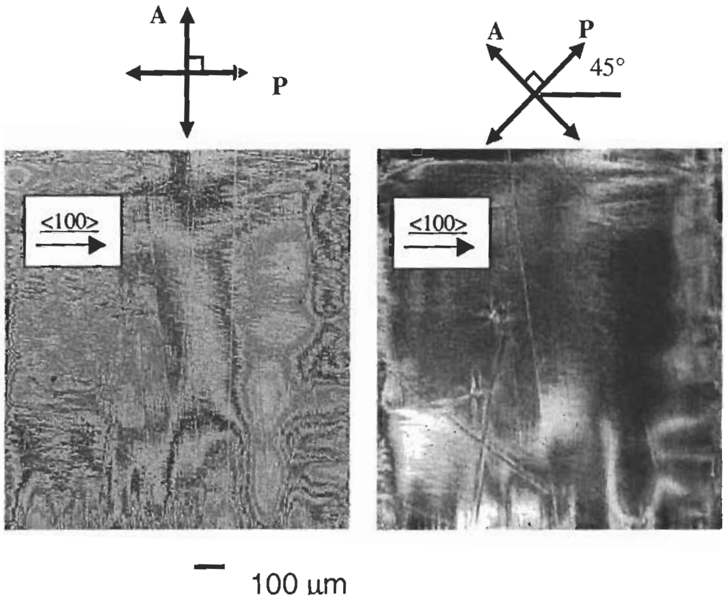

(a) (b)

Figure 6.2: Domain structure of a (1-x)$Pb(Sc_{1/2}Nb_{1/2})O_3 - xPbTiO_3$ (x = 0.425) single crystal (PSNT–C) observed at room temperature under polarized light microscopy:
a) crossed polarizers // <001>-directions, and b) crossed polarizers // <110>-directions.

The long-range ferroelectric state has also been evidenced by the observation of domain structure in the PSNT–C crystals by polarized light microscopy, as shown in Figure 6.2. Figure 6.2(a) reveals that the crystal exhibits birefringent domains with a fine structure, indicating the existence of macro domain states in it. In Figure 6.2(b), the sample was rotated in such a way that the $<001>_{cub}$ direction forms an angle of 45° with the directions of the crossed polarizers. It can be seen that under this configuration, most areas are in full extinction, indicating a rhombohedral symmetry at room temperature.

For PSNT-A, the broadening of the dielectric peak with a lower magnitude suggests that the crystal may have a lower quality, which probably arises from lead/oxygen vacancies. In the growth of PSNT–A crystals, the amount of excess PbO was lower and the growth temperature was higher compared with PSNT–B and PSNT–C, which could favour the formation of the vacancies. The brown colour that the PSNT-A crystal exhibits is an indication of a high concentration of point defects due to Pb^{2+}/O^{2-} vacancies as found in $PbTiO_3$ crystals [122]. As a result of the vacancies, the spontaneous transition from the relaxor state to the macroscopic ferroelectric state is suppressed. The higher T_{max} in PSNT-A indicates that the crystal possesses a higher Ti-content, but the titanium seems to be distributed inhomogenously over the crystals, giving rise to a broadened dielectric peak.

6.5 Phase Symmetry and Phase Sequence of the $(1\text{-}x)Pb(Sc_{1/2}Nb_{1/2})O_3 - xPbTiO_3$ Single Crystals of MPB Composition

As discussed in **Section 6.4**, the actual composition of grown $(1-x)Pb(Sc_{1/2}Nb_{1/2})O_3 - xPbTiO_3$ single crystals usually differs from the nominal charged composition. The revised MPB phase diagram of PSN–PT solid solution in Figure 3.13 reveals a linear relationship between T_C and composition x. So the corresponding composition for PSNT–A, –B, and –C is found to be in the range of $0.26 < x < 0.33$. Therefore, the composition of grown single crystals shifts about 13±4% away from the nominal charged composition ($x = 0.425$). By adding an additional PT content of (~13%) into the growth chemicals, together with the optimized growth conditions described in **Chapter 4**, PSN–PT crystals with compositions within the MPB region were synthesized by the high temperature solution method.

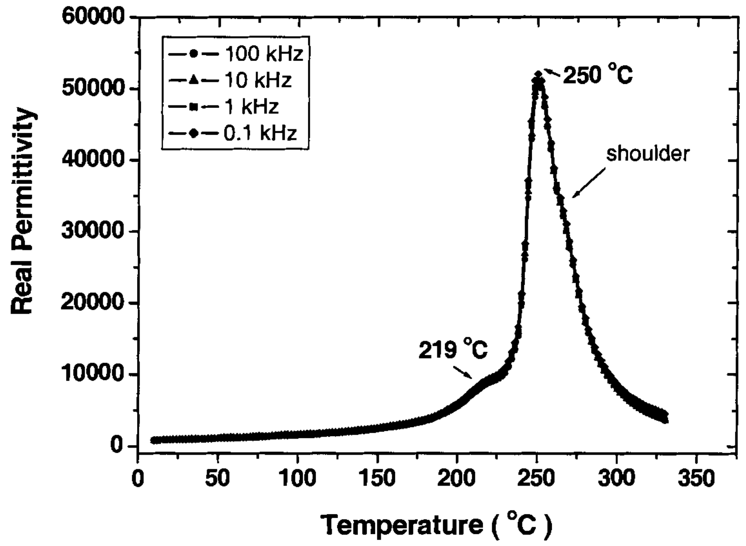

Figure 6.3: Variation of the real part of permittivity of $(1\text{-}x)\mathrm{Pb}(\mathrm{Sc}_{1/2}\mathrm{Nb}_{1/2})\mathrm{O}_3 - x\mathrm{PbTiO}_3$ single crystals with composition within the MPB, as function of temperature, measured upon cooling.

The dielectric permittivity measured upon cooling is shown in Figure 6.3. It reveals two anomalies at T_C = 250 °C and T_{MPB} =219 °C, respectively, typical of MPB behaviour of ferroelectric solid solution. According to the MPB phase diagram in Figure 3.13, the composition of this PSN–PT crystal is located at x = 0.37, hereafter denoted as 0.63PSN–0.37PT. A maximum of dielectric constant as high as 50,000 was obtained with a loss value less than 0.02 (at 1 kHz). The phase transition at T_C appears as a sharp peak without frequency dispersion. This suggests that as the Ti-content increases to 37%, the crystal behaves like a normal ferroelectric with a non-dispersive and sharp phase transition. A slight "shoulder-like" anomaly was observed at about 265 °C for all frequencies, which could be due to the nucleation of precursor domains.

In order to analyze the phase symmetry of 0.63PSN–0.37PT crystals, X-ray profiles of the pseudocubic $(111)_c$ and $(200)_c$ reflections were analyzed using the

Lorentzian fitting procedure described in **Section 3.4.1**. The results are shown in Figure 6.4(a). Both $(111)_c$ and $(200)_c$ reflections can be well fitted with three peaks. For comparison, Figure 6.4(b) displays the fitting results for the same reflections of the 0.63PSN–0.37PT ceramics. It can be seen that the structural feature of the 0.63PSN–0.37PT crystal is similar to that of the 0.63PSN–0.37PT ceramics, with the same phase components but slightly different intensity ratios probably due to the different grain size and orientations. This confirms that composition of the PSN–PT crystal is close to x = 0.37. The analysis of the $(111)_c$ and $(200)_c$ reflections indicates that a monoclinic phase is presented as a major phase in the 0.63PSN–0.37PT crystal, which is consistent with the results of the 0.63PSN–0.37PT ceramics (see **Section 3.4.3**).

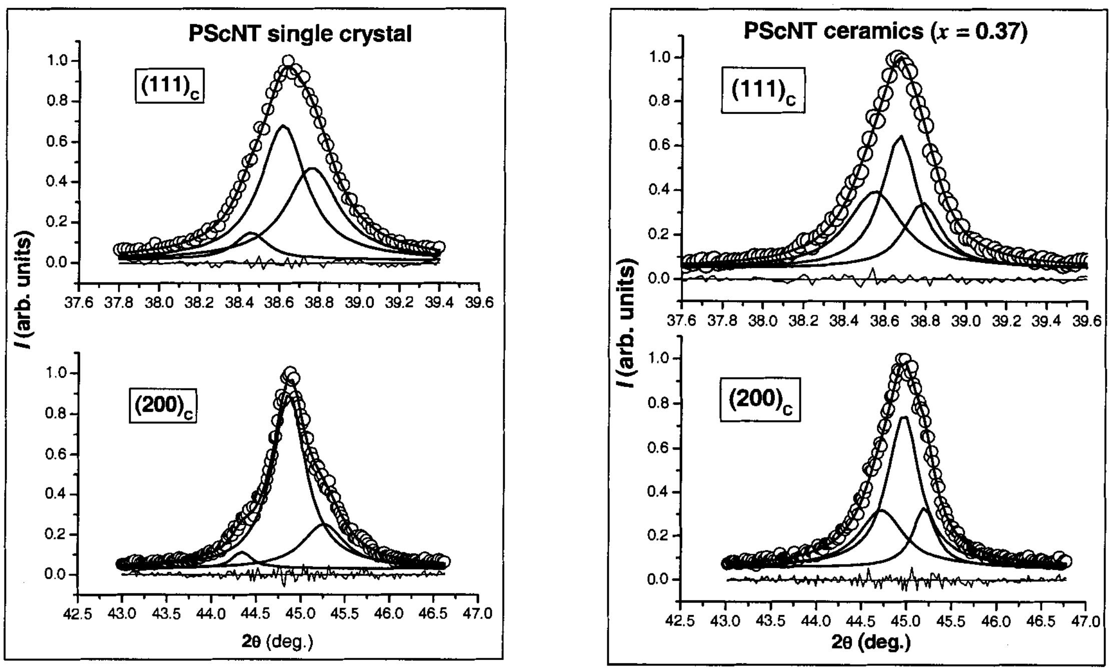

(a) (b)

Figure 6.4: Analysis of the X-ray profiles of $0.63Pb(Sc_{1/2}Nb_{1/2})O_3 - 0.37PbTiO_3$ single crystals and ceramics (open circles: experiment data; solid lines: fitting results)

6.6 Conclusions

Single crystals of (1-*x*)PSN–*x*PT were grown by the high temperature solution method with different ratios of excess PbO from the 57.5$Pb(Sc_{1/2}Nb_{1/2})O_3$ – 42.5$PbTiO_3$ nominal charge. It is found that the growth conditions have significant effects on the chemical (composition, ordered/disordered structure and vacancies) and physical (dielectric constant, domain structure and phase transitions) properties of the grown crystals. The crystals with a high degree of disorder and a low level of lead/oxygen vacancies show a spontaneous phase transition from the relaxor state to the normal ferroelectric state, the same as revealed in pure disordered PSN. The domain structure of the same crystals shows birefringent domains with fine structure at room temperature, confirming the formation of macro domain state of rhombohedral symmetry. Because of the growth defects and composition inhomogeneity, the crystals grown from a lower concentration of PbO-flux and a higher temperature exhibit a broadened dielectric peak and the transition from nano-polar relaxor state to long-range ferroelectric state is suppressed.

For (1-*x*)PSN–*x*PT single crystals with composition near or within the MPB, the frequency dependence of the dielectric permittivity is similar to that of normal ferroelectrics due to the increase of the normal ferroelectric ordering induced by the increasing Ti^{4+} ion. The macro domain state is observed in the (1-*x*)$Pb(Sc_{1/2}Nb_{1/2})O_3$ – *x*$PbTiO_3$ ($0.26< x < 0.33$) single crystals, indicating the rhombohedral symmetry at room temperature. As the Ti-content further increases, the crystals reach the MPB compositions. The dielectric permittivity as a function of temperature of the 0.63PSN–0.37PT crystal clearly indicates two phase transitions, showing the typical characteristics of a ferroelectric solid solution with the MPB region. The phase analysis by XRD reveals the presence of the monoclinic in the 0.63PSN-0.37PT crystal, which coexists with the tetragonal phase. This results is consistent with the morphotropic phase diagram reported in **Chapter 3** for the $(1-x)Pb(Sc_{1/2}Nb_{1/2})O_3 - xPbTiO_3$ ceramics.

Chapter 7:
A New Family of Piezoelectric Single Crystals:
(1-x)$PbSnO_3 - x PbTiO_3$

7.1 Abstract

Single crystals of the (1-x)$PbSnO_3 - x PbTiO_3$ (PbSnTi) solid solution system have been successfully grown for the first time by a high temperature solution method using ($PbO+\delta B_2O_3$) as flux. Crystals with a length of 8mm have been obtained. X-ray diffraction confirms the pure perovskite structure. The dielectric, ferroelectric and piezoelectric properties of transparent (001) crystallize platelets of $0.40PbSnO_3$–$0.60PbTiO_3$ are characterized. The temperature dependence of the dielectric permittivity (upon cooling) reveals a Curie temperature of 206 °C, with a second anomaly at 190 °C associated with a phase transition between two ferroelectric phases, a typical behaviour of the morphotropic phase boundary solid solution systems. The room temperature ferroelectric and piezoelectric properties are summarized with the following parameters: remnant polarization $P_r = 23\pm1$ μC/cm^2, coercive electric field $E_C = 2.8\pm0.2$ kV/cm, electromechanical coupling factor $k_{33} = 73\pm1\%$, and piezoelectric coefficient $d_{33} = 370\pm10$ pC/N.

7.2 Introduction

Lead-based perovskite solid solutions, especially the class that contains $PbTiO_3$, a ferroelectric material, as one of the two components, are of great interest for piezoelectric applications. In the $PbZrO_3 - PbTiO_3$ (PZT) system, the ceramics with compositions near the so-called morphotropic phase boundary (MPB) exhibit an enhanced piezoelectric response [34] and have become the most utilized materials in electromechanical transducers, sensors and actuators [123]. Recently, an ultrahigh piezoelectric effect with a piezoelectric coefficient d_{33} and a strain level almost 10 times larger than the conventional PZT ceramics have been discovered. This was found for single crystals of the relaxor-based $Pb(Mg_{1/3}Nb_{2/3})O_3 - PbTiO_3$ (PMN–PT) and $Pb(Zn_{1/3}Nb_{2/3})O_3 - PbTiO_3$ (PZN–PT) solid solutions [46]. This outstanding performance was achieved in single crystals at room temperature using suitable domain engineering along the $<001>_{cub}$-orientation. A great deal of research [59, 61, 63, 124] has been carried out in the last few years, which has greatly advanced the materials technology of PMN–PT and PZN–PT single crystals and demonstrated the device potentials.

However, the PMN–PT and PZN–PT single crystals exhibit relatively low Curie temperature (T_C = 140-170 °C) and an even lower morphotropic phase boundary temperature (T_{MPB} = 80 – 110 °C) due to a strongly curved MPB [44]. The materials with the lower Curie temperature possibly show a high temperature dependence of dielectric response and nonstable domain engineering state due to possible depolarization, which will degrade the performance of piezoelectric devices. This inherent drawback limits the use of PMN–PT and PZN–PT. Therefore, materials with good temperature stability over a larger range are essential for practical applications. Recently, more attentions have been paid to search for piezocrystals with high Curie temperature and excellent piezoelectric performance. In this context, the system of $BiScO_3$–$PbTiO_3$ [66],

$Pb(In_{1/2}Nb_{1/2})O_3$–$PbTiO_3$ [125], and $Pb(Sc_{1/2}Nb_{1/2})O_3$–$PbTiO_3$ [95] have been studied by different groups.

Early studies of ceramic (1-x)$PbSnO_3$ – $x$$PbTiO_3$ (PbSnTi) solid solutions were carried out by Nomura *et al.* [80], Smolenskii *et al.* [81] and Jaffe *et al.* [82]. A preliminary phase diagram reported by Jaffe *et al.* suggested a possible boundary around x = 0.50, separating the ferroelectric tetragonal phase and another phase of unknown symmetry. The dielectric measurements reported in Ref. [81] showed the enhanced dielectric constant occurring at x = 0.50 with $T_C \approx 290$ °C. The Curie temperature (290 °C) of PbSnTi with composition x = 0.50 is much higher than the T_C of PMN–33%PT (166 °C) and PZN–4.5%PT (155 °C) with compositions around the MPB. The features above subject the criterions that the solid solution systems display the properties of morphotropic phase boundary with high Curie temperature (**Chapter 1,** section 1.5) and are mainly motivations of this work.

In this work, we have grown the (1-x)$PbSnO_3$ – $x$$PbTiO_3$ single crystals by a high temperature solution method. The dielectric, ferroelectric and piezoelectric properties of the PbSnTi single crystals are reported.

7.3 Growth of (1-x)$PbSnO_3$ – $x$$PbTiO_3$ Single Crystals

From the (1-x)$PbSnO_3$ – $x$$PbTiO_3$ (PbSnTi) phase diagram in Figure 1.11(a), we can see that the perovskite PbSnTi solid solution can only be stabilized with the presence of a certain amount of PT (>30% in Figure 1.11(b)) and the possible MPB is suggested to be around x = 0.50 [82]. Therefore, we grew the (1-x)$PbSnO_3$ – $x$$PbTiO_3$ single crystals with nominal composition x = 0.60 by a high temperature solution method using

($PbO+B_2O_3$) as flux. The same considerations as used in the growth of (1-x)$Pb(Sc_{1/2}Nb_{1/2})O_3$ – $xPbTiO_3$ crystals (**Chapter 4**) were applied here. The starting materials of high-purity (>99.99%) of PbO, SnO_2 and TiO_2 were weighed according to the chemical reaction:

$$PbO+xTiO_2+(1-x)SnO_2 \rightarrow (1-x)PbSnO_3 - xPbTiO_3 \quad , \qquad (6.1)$$

with the composition of $x = 0.60$, and then mixed with the flux of $PbO+B_2O_3$. Table 7.1 lists the amount of the raw materials used in the growth of $0.40PbSnO_3$ – $0.60PbTiO_3$ single crystals for 100 gram of mixture.

Table 7.1: Amount of the raw materials used in the growth of $0.40PbSnO_3$ – $0.60PbTiO_3$ single crystals for 100 gram of mixture

Component	Weight (gram)
PbO	89.1884
B_2O_3	1.6503
SnO_2	5.1028
TiO_2	4.0585
Total	100.0000

The mixture was ground for more than one hour, and loaded into a Pt crucible (35 ml), and then premelted at temperature around 900 °C. The crucible was then placed in an alumina crucible, which was sealed to an alumina lid with Al_2O_3 cements to prevent the evaporation of PbO, as shown in Figure 4.1 (**Chapter 4**) [59]. The loaded crucible was then put into a muffle furnace and heated to 1180 °C and soaked for 5 hrs. It was then slowly cooled down at a gradually increasing rate of 0.5 °C/h to 3 °C/h. The typical was leached out with hot aqueous mixture of the acetic acid (1.7M) and nitric acid (0.5M).

The as-grown crystals show maximum dimensions of 8 mm, as shown in Figure 7.1(a). The platelets obtained after polishing appear transparent with a yellow or light brown colour, as shown in Figure 7.1(b). Figure 7.1(c) shows an as-grown crystal that exhibits the $(100)/(111)_{cub}$ growth facets. X-ray powder diffraction (XRD) of crushed crystals reveals a pure perovskite structure, as shown in Figure 7.2.

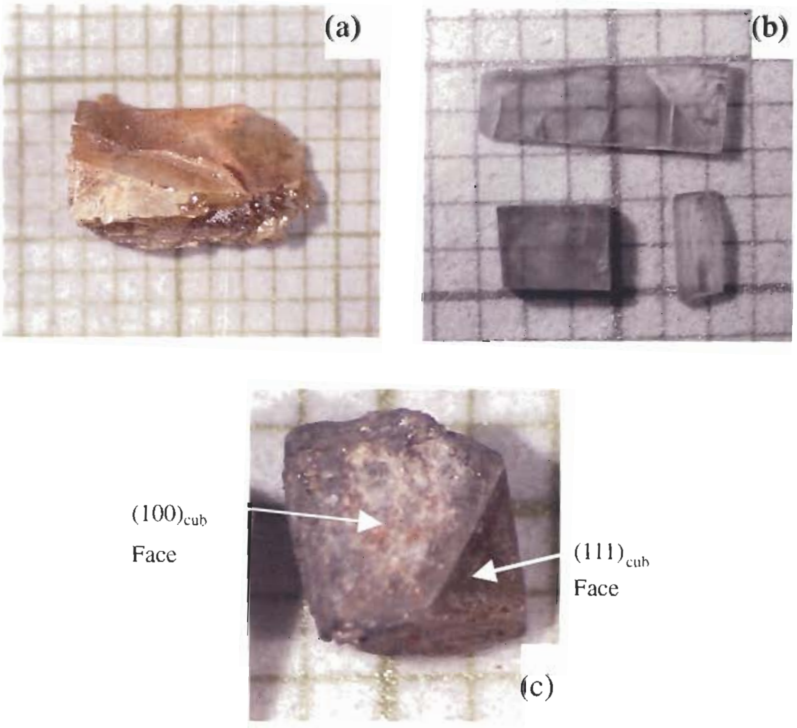

Figure 7.1: Photograph of $0.40PbSnO_3 - 0.60PbTiO_3$ single crystals a) an as-grown crystal; b) crystal platelets after polishing (scale = 1mm); c) an as-grown crystal showing the growth facets.

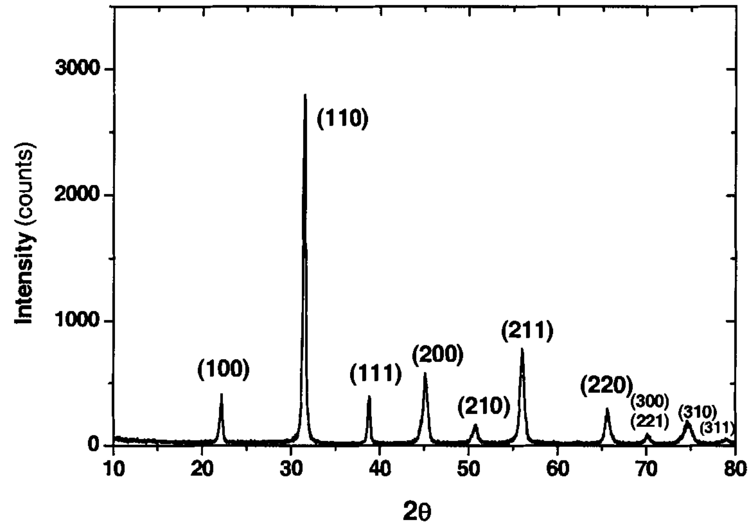

Figure 7.2: X-ray spectrum of $0.40PbSnO_3 - 0.60PbTiO_3$ single crystals.

7.4 Characterization of $(1\text{-}x)PbSnO_3 - xPbTiO_3$ Single Crystals

For the measurements of dielectric, ferroelectric and piezoelectric properties, platelets of $0.40PbSnO_3$ – $0.60PbTiO_3$ (hereafter designated as PbSnTi60) were cut parallel to the crystallographic (001) plane, polished and sputtered with gold layers as electrode. The ferroelectric property was characterized by the measurements of polarization as a function of electric field using an RT66A Standard Ferroelectric Testing System (Radiant Tech.). Figure 7.3 shows the hysteresis loops, indicating the ferroelectricity in PbSnTi single crystals. The hysteresis loop saturates at E = ±18±1 kV/cm and a remnant polarization of $P_r = 23\pm1$ μC/cm^2 is detected. The coercive field E_C is 2.8±0.2 kV/cm. The high ferroelectric performance of the PbSnTi single crystals is comparable to the PMN-PT and PZN–PT piezocrystals. Note that the hysteresis loops reported in Ref. [80] on the PbSnTi ceramics were poorly developed and not saturated. Moreover, the magnitude of the maximum polarization of PbSnTi ceramic reported therein was less than 1 μC/cm^2 at a field of ± 10 kV/cm. In comparison, the maximum polarization measured in this work on the PbSnTi single crystal (Figure 7.3) reaches 25±1 μC/cm^2, which is more than 20 times larger than the value reported for the ceramics. In the PbSnTi ceramics, it is possible that high temperature sintering resulted in the appearance of SnO_2 and the formation of pyrochlore phase, thus degrading the ferroelectric properties with poorly developed hysteresis. The well-developed hysteresis loops displayed in the PbSnTi crystals with abrupt switching of the polarization at the coercive field implies a rapid response of the domain reorientations under a relatively low electric field drive, indicating a good quality of the crystals.

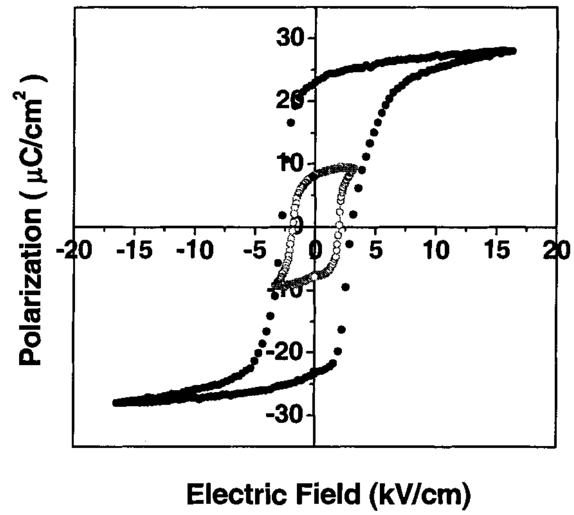

Figure 7.3: Polarization vs. bipolar electric field (P-E) loops for <001>-oriented $0.40PbSnO_3 - 0.60PbTiO_3$ single crystal, showing ferroelectricity.

The strain vs. electric field was determined by an MTI-2000 Fotonic Sensor (Mech. Tech. Inc.). The PbSnTi crystal shows a strain level of 0.07% under a unipolar driven field of 18 kV/cm, as shown in Figure 7.4. A piezoelectric coefficient d_{33} = 370±10 pC/N was calculated from the slope of unipolar strain vs. electric field.

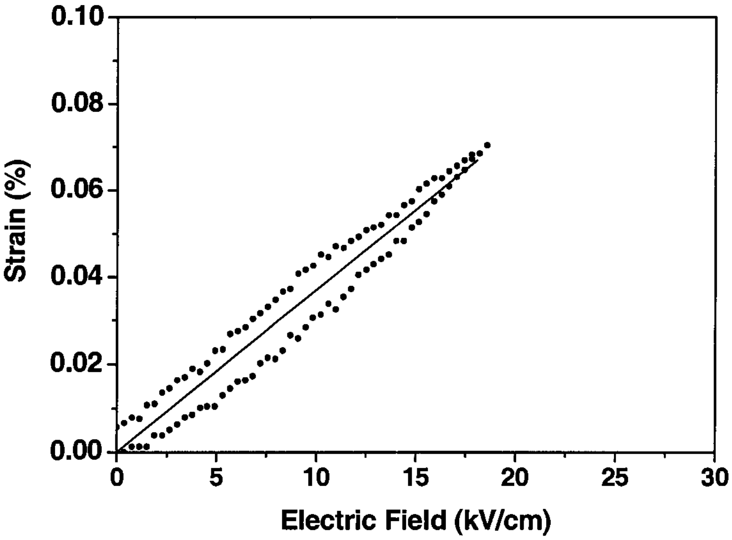

Figure 7.4: Unipolar strain vs. electric field for <001>-oriented 0.40PbSnO$_3$ – 0.60PbTiO$_3$ single crystal.

The longitudinal electromechanical coupling factor k_{33} was determined by the measurements of the resonance (f_r) and antiresonance (f_a) frequencies for a <001>-oriented PbSnTi60 crystal rod with dimensions of 0.68x0.73x1.58 mm^3. The sample was preliminarily poled at room temperature under a filed of 15 kV/cm. Afterward, the piezoelectric resonance measurement was carried out on a Solartron 1260 Impedance Analyzer combined with a Solartron 1296 Dielectric Interface. Figure 7.5 displays the impedance and phase angle curves in the frequency range of the resonance and antiresonance. The values of f_r and f_a were found to be 853.2 kHz and 1177.7 kHz, respectively. k_{33} and the piezoelectric coefficients d_{33} were calculated according to Eqs. (2.5–2.8) (**Chapter 2**) [86]. The calculated k_{33} is 73±1% and d_{33} is 350±10 pC/N, which is consistent with the value calculated from the unipolar strain measurement.

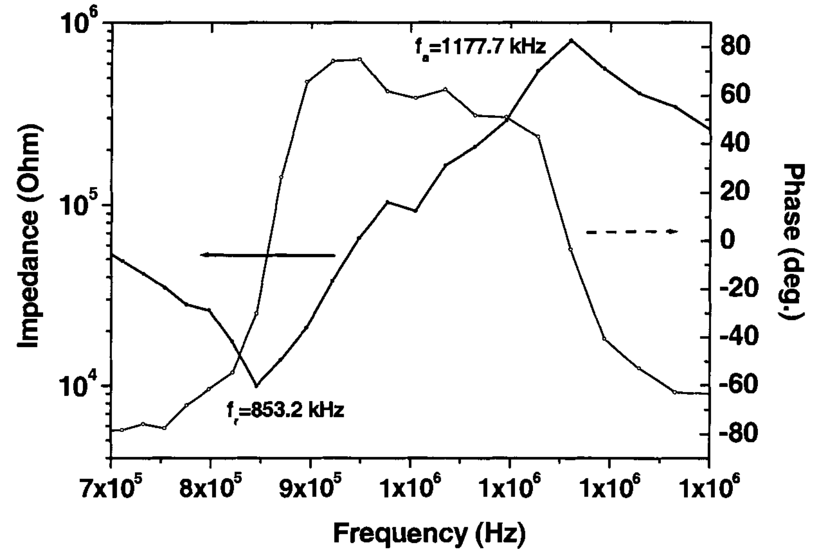

Figure 7.5: Resonance and antiresonance frequencies measurements from impedance and phase angle for <001>-oriented 0.40PbSnO$_3$ – 0.60PbTiO$_3$ single crystal.

The dielectric permittivity of the PbSnTi60 crystal as a function of temperature at various frequencies was measured between room temperature and 330 °C upon cooling by means of an Alpha High Resolution Dielectric/Impedance Analyzer (NovoControl). The temperature dependencies of the real permittivity ε' and the loss at frequencies of 0.1, 1, 10, 100 kHz are presented in Figure 7.6. The dielectric maximum is observed at 206 °C as a sharp peak, with the maximum values reaching above 80,000 at all the frequencies measured. A second dielectric anomaly is observed at 190 °C with a more broadened peak. By analogy to the initial PZT phase diagram [34], this anomaly indicates the phase transition between two ferroelectric phases, very likely from a tetragonal to a rhombohedral phase. Thus, the anomaly temperature is named $T_{r\text{-}t}$, which is equivalent to the T_{MPB} found in PSN–PT system. The dielectric permittivity is nearly temperature independent from room temperature up to 100 °C, indicating a good thermal stability.

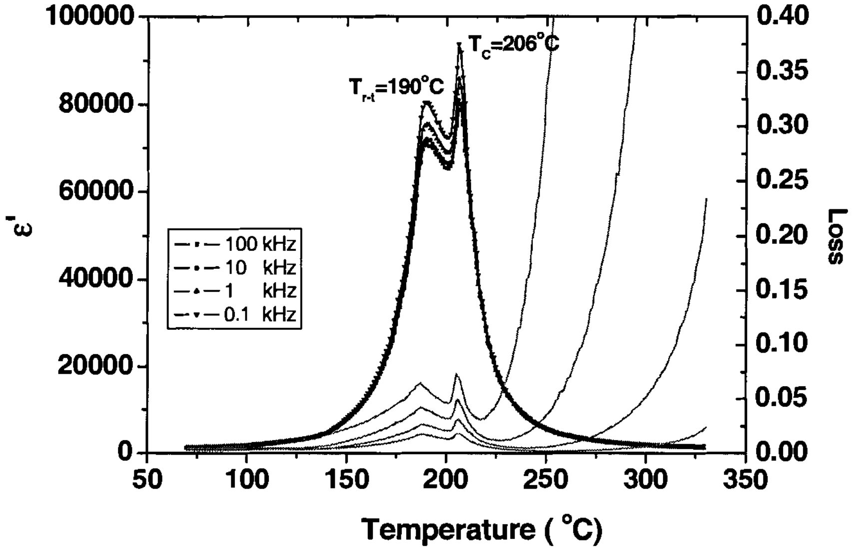

Figure 7.6: Dielectric constant and losses of <001>-oriented 0.40PbSnO$_3$ – 0.60PbTiO$_3$ single crystal measured as a function of temperature at frequencies of 0.1, 1, 10, 100 kHz.

The dielectric losses (tanδ) also show clearly two peaks, corresponding to those in the real part of permittivity. The loss at room temperature is about 0.4%, and it increases rapidly above T_C, because of the increasing conductivity. The buildup of the conductivity is believed to arise from the presence of some lead/oxygen vacancies formed during the crystal growth at high temperatures. The light brown colour of the crystals also suggests the existence of possible vacancies [122]. The frequency dispersion of the permittivity maximum, usually observed in the lead-based relaxor ferroelectric crystals, is not seen in the permittivity spectra of the PbSnTi crystals. Since PbSnO$_3$ does not exist as a stable compound, its dielectric property is unknown. Nonetheless, from the above results we can draw the conclusion that the PbSnTi crystals (upon cooling) first undergo a structural transition from the cubic paraelectric phase to a ferroelectric tetragonal phase, as evidenced by the sharp dielectric peak at $T_C = 206$ °C. This sharp transition behaves more like a normal ferroelectric transition, featuring the behaviour of $PbTiO_3$. This tetragonal intermediate phase exists between T_C and T_{r-t}, and upon further cooling transforms at T_{r-t} = 190 °C into another ferroelectric phase of rhombohedral symmetry. The permittivity peak at T_{r-t}, although broader than the peak at T_C, is much sharper than in other materials, for example, PMN-PT [45] and $BiScO_3 - PbTiO_3$ [66], in which only a shoulder-like peak was observed in their permittivity spectra. For the 0.70PMN-0.30PT single crystals, Shrout *et al.* [45] reported that the anomaly of the dielectric constant at T_{r-t} was sharpened accompanying with the increases of the magnitude of dielectric constant upon heating after poling, which was attributed to a transition from macro domain to micro domain state. The sharp peak detected in the PbSnTi crystal (unpoled) suggests a dramatic change in domain size at the tetragonal to rhombohedral transition.

According to the original phase diagram [Figure 1.11(a)], the T_C for the $0.40PbSnO_3 - 0.60PbTiO_3$ should be at 300 °C. We noticed that the T_C = 206 °C of the PbSnTi60 crystal is, however, significant lower than that. It is even lower than the T_C (290 °C) of the $0.5PbSnO_3$-$0.5PbTiO_3$ ceramics reported in Ref. [81]. The reason for this discrepancy is still under investigation. From the point view of crystal growth, the shift of composition away from the charged nominal composition commonly occurs in the grown crystals of almost all the solid solution systems due to the difference in segregation coefficient between the different ions. A lower Ti-content in the grown PbSnTi crystal, as suggested by the lower T_C, indicates that the segregated liquidus/solidus curves go down as x increases. Further investigations on both the high-temperature and low-temperature phase diagram of the $PbSnO_3 - PbTiO_3$ system are highly desirable to shed light on the phase segregation coefficient, the chemical compositions and the phase transitions.

7.5 Conclusions

The single crystals of (1-x)$PbSnO_3$ – $x$$PbTiO_3$ solid solution have been successfully grown for the first time by the high-temperature solution method. A disordered simple perovskite structure was confirmed by the XRD spectrum probably due to the ionic radii of Sn^{4+} (0.67 Å) and Ti^{4+}(0.64 Å) are very close to each other, the Sn^{4+} and Ti^{4+} ions occupy randomly on the B-sites of octahedron.

Table 7.2: Dielectric, ferroelectric and piezoelectric properties of <001>-oriented $0.40PbSnO_3 – 0.60PbTiO_3$ single crystals compared with those of the 0.70PMN – 0.30PT crystals [66] and PZT ceramics [1].

Composition	PbSnTi60 crystal	PMNT30 crystal^a	Type II* PZT ceramic
T_C (°C)	206	138	340
$T_{r\text{-}t}$ (°C)	190	98	
ε(RT)	1440	5000	2050
$tan\ \delta$	0.004	0.005	0.018
P_r (μC/cm^2)	23	26	
E_C (kV/cm)	2.8	2.3	
k_{33}	73%	89%	73%
d_{33} (pC/N)	370	1600	400

$^{a)}$<001>-oriented single crystal.

*see Appendix I for descriptions.

The grown crystals have been characterized by dielectric, ferroelectric and piezoelectric measurements. The temperature and frequency dependencies of the dielectric permittivity of the PbSnTi60 single crystals show a Curie temperature of T_C = 206 °C and a $T_{r\text{-}t}$ = 190 °C, indicating a typical MPB behaviour, similar to the solid solution systems of PZT, PMN-PT, PZN-PT and PSN-PT. The PbSnTi single crystals exhibit remnant polarization of 23 μC/cm^2 and strain level up to 0.07% at a unipolar electric field of 18 kV/cm. The piezoelectric coefficient d_{33} = 350 – 370 pC/N and the coupling factor k_{33} = 73%.

The values for the dielectric, ferroelectric and piezoelectric properties of the <001>-oriented PbSnTi60 crystal are tabulated in Table 7.2, together with the data for 0.70PMN – 0.30PT crystals [66] and PZT ceramics [1] for comparison. It can be seen that the dielectric (ε' and tanδ) and piezoelectric (k_{33}, d_{33}) properties of the PbSnTi60 crystal are comparable with the PZT ceramics. The properties are lower than in the 0.70PMN – 0.30PT (MPB) crystals, but T_C, and especially $T_{r\text{-}t}$, of the PbSnTi crystals are much higher than those of the PMN–PT crystals. This suggests that, upon optimization of the MPB composition and properties, the PbSnTi single crystals can form a new resource of high piezoelectric crystals with high T_C and high $T_{r\text{-}t}$, potentially useful for a wide range of electromechanical transducer applications.

Chapter 8:
Structural Phase Transition and Dielectric Relaxation in $Pb(Zn_{1/3}Nb_{2/3})O_3$ Single Crystals

The following chapter is a revised version of the paper published in ***J. Phys.: Condens. Matter.***, by **Y-H. Bing, A. A. Bokov, Z.-G. Ye, B. Noheda and G. Shirane**, ["Structural Phase Transition and Dielectric Relaxation in $Pb(Zn_{1/3}Nb_{2/3})O_3$ Single Crystals", Volume 17, Number 15, pp. 2493-2507, 20 April (2005)]. The reproduction of this paper is permitted by IOP Publishing Limited. The Publisher's Internet address: www.iop.org/journals/jpcm.

8.1 Abstract

The structure and the dielectric properties of $Pb(Zn_{1/3}Nb_{2/3})O_3$ (PZN) crystal have been investigated by means of high-resolution synchrotron x-ray diffraction (with an X-ray energy of 32 keV) and dielectric spectroscopy (in the frequency range of 100 Hz – 1 MHz). At high temperatures, the PZN crystal exhibits a cubic symmetry and polar nanoregions inherent to relaxor ferroelectrics are present, as evidenced by the single (222) Bragg peak and by the noticeable tails at the base of the peak. At low temperatures, in addition to the well-known rhombohedral phase, another low-symmetry, probably ferroelectric, phase is found. The two phases coexist in the form of mesoscopic domains. The para- to ferroelectric phase transition is diffused and observed between 325 and 390 K, where the concentration of the low-temperature phases gradually increases and the cubic phase disappears upon cooling. However, no dielectric anomalies can be detected in the temperature range of the diffuse phase transition. The temperature dependence of the dielectric constant shows a maximum at higher temperature (T_{max} = 417 – 429 K,

depending on frequency) with the typical relaxor dispersion at $T < T_{max}$ and the frequency dependence of T_{max} fitted to the Vogel-Fulcher relation. Application of an electric field upon cooling from the cubic phase or poling the crystal in the ferroelectric phase gives rise to a sharp anomaly of the dielectric constant at $T \approx 390$ K and diminishes greatly the dispersion at lower temperatures, but the dielectric relaxation process around T_{max} remains qualitatively unchanged.

8.2 Introduction

$Pb(Zn_{1/3}Nb_{2/3})O_3$ (PZN) and $Pb(Mg_{1/3}Nb_{2/3})O_3$ (PMN) are two prototypical relaxor ferroelectric materials with complex perovskite structure, in which the off-valent Zn^{2+} (or Mg^{2+}) and Nb^{5+} ions occupying the B-sites are primarily disordered [126]. Research on relaxor ferroelectrics and related materials has undergone an accelerated growth in the last few years both in fundamental understanding of the structure and physical properties and in practical applications. This is partly due to the excellent piezoelectric properties discovered in the single crystals of the solid solutions between PZN (or PMN) and ferroelectric $PbTiO_3$, which point to the next generation of electromechanical transducer applications [46, 127]. Recent neutron scattering studies have identified a ferroelectric soft mode in PMN at 1100 K that becomes overdamped below the Burns temperature $T_d \approx 620$ K (i.e. the temperature at which polar nanoregions, PNRs, begin to appear), suggesting a direct connection between the soft mode and the PNRs [128]. More interestingly, at lower temperature the soft mode in PMN reappears close to $T_C = 213$ K [129], the temperature at which the electric field-induced polarization vanishes spontaneously upon zero field heating [104], and a peak in the temperature dependence of the hypersonic damping appears [130]. To interpret the measured intensities of the diffuse scattering in PMN in accordance with the concept of the ferroelectric soft mode, Hirota *et al.* [131] have proposed and demonstrated the validity of a phase-shifted condensed soft mode model of the PNRs. This model suggests the displacement of PNRs along their polar directions relative to the surrounding cubic matrix (H-shift). Therefore, the phonon dynamics clearly indicates the ferroelectric nature of the relaxor PMN, although the average structure of the system remains cubic and optically isotropic.

Application of an electric field along the <111> direction can induce a long-range (single domain) ferroelectric phase in PMN, with the development of a polar rhombohedral *R*3m phase associated with switchable polarization and birefringent macro domains [104, 132, 133].

By means of dielectric spectroscopy, Bokov and Ye [25, 26, 27] have discovered a "universal" relaxor dispersion in PMN and related materials, and showed that it is an important common property of relaxor ferroelectrics. The universal relaxor polarization is described by a microscopic model of 'soft' polar nanoregions with unit cells that can freely choose several different directions, while the direction of the total moment of the nanoregion remains the same [27]. Such an approach makes it possible to apply a standard spherical model to relaxor ferroelectrics, which predicts the experimentally observed quadratic divergence of the universal part of the susceptibility above the critical temperature. This model is complementary to the so-called spherical random bond – random field model proposed by Blinc *et al.* [28, 29] to explain the NMR data and the non-linearity of the total dielectric susceptibility in relaxors.

In comparison with PMN, the crystal structure and polar order of PZN appear to be quite different. Earlier work reported that a phase transition from cubic to a rhombohedral phase took place upon cooling, which was associated with the maximum of the dielectric constant occurring at T_{max} around 410 K [134, 135, 136]. At room temperature weakly birefringent domains with extinction directions along $<110>_{cub}$ were observed on a $(001)_{cub}$–cut PZN platelet, which seems to confirm the rhombohedral symmetry. The value of birefringence decreases gradually upon heating but more sharply around 390 K before vanishing at $T \geq 413$ K [137]. Recently, Lebon *et al.* [138] reported that the cubic-to-rhombohedral phase transition in PZN is diffuse and spreads over the temperature range between 385 and 325 K with a full establishment of the rhombohedral phase below 325 K. This phase consists of domains of mesoscopic (60-70 nm) size. Application of a dc field along <111> transforms the polydomain state into a rhombohedral quasi-monodomain state. High-energy X-ray diffraction studies on PZN crystals by Xu *et al.* [139] revealed Bragg peaks resembling a tetragonal (or pseudo-cubic) symmetry (X-phase) for the bulk crystal, the nature of which is yet to be clarified. On the other hand, neutron scattering results showed the onset of diffuse scattering at the Burns temperature, and a softening of the optical mode at the critical temperature, analogous to PMN [140].

Despite recent intense work, the nature of phase transitions and dielectric relaxation in relaxors has not been thoroughly understood. In this work, we have studied the structural transformation in PZN crystals by synchrotron X-ray diffraction and by analyzing the dielectric properties as a function of temperature and frequency at zero-field and under a dc field.

8.3 Experiment

PZN single crystals were grown by spontaneous nucleation from high temperature solution according to the method and conditions previously developed in our lab, as described in Ref. [62]. A crystal plate of a triangle shape (4 mm in edge and 330 μm thick) was cut with large surfaces parallel to the $(111)_{cub}$ plane. The $(111)_{cub}$ faces were mirror polished using a series of diamond pastes down to 3 μm. For the dielectric measurements, the sample was sputtered with gold layers on the $(111)_{cub}$ faces in a central area of 1.5x1.5 mm^2. Two gold wires were attached to the electrodes using silver paste. For the poling of the sample, an electric field of 20 kV/cm was applied at room temperature and kept on for a half-hour. The crystal was then short-circuited to remove possible space charges injected.

X-ray diffraction experiments were carried out on the unpoled crystal using the X22A beamline (32 keV, $\lambda = 0.38 \pm 0.01$ Å, with a penetration depth of 30 μm at normal incidence) from the National Synchrotron Light Source (NSLS) at the Brookhaven National Laboratories. The beamline is equipped with a four-circle Huber diffractometer, with Si (220) and Si (111) analyzer-crystals mounted in the diffraction path. The diffraction data were collected in a temperature range between 420 K and 25 K upon cooling. The accuracy of the temperature measurement was within ± 5 K and the temperature stability within ± 2 K. The θ–2θ scans were performed over selected angular ranges centered about the (200), (220) and, in particular, (222) cubic reflections. The Lorentzian, and the Gaussian functions were applied for the X-ray analysis.

Dielectric spectroscopic measurements were performed by means of a computer-controlled system consisting of a Solartron–1260 Impedance Analyzer and a Solartron–

1296 Dielectric Interface, at various frequencies (100 Hz - 1 MHz) in the temperature interval between 310 K and 620 K. The measurements were carried out under various conditions: 1) Zero-field-cooling (ZFC); 2) Field-cooling (FC) for unpoled crystals by applying a dc bias field; 3) Zero-field-heating (ZFH) for prepoled crystal.

8.4 Results and Analysis

8.4.1 Structural Transformation

Because the small distortion in PZN structure, high resolution synchrotron X-ray diffraction is needed to determine more accurately symmetry components and ratios. Preliminary synchrotron X-ray diffraction experiments were undertaken on a pressed PZN powder sample obtained by crushing small single crystals at X22A in the Bragg-Brentano geometry. The data collected for several characteristic reflections show a single peak for $(200)_{cub}$, a double peak for $(220)_{cub}$ and a double peak for $(222)_{cub}$ reflections, which indicate a non-cubic and very likely a rhombohedral symmetry.

In the $(111)_{cub}$ crystal, the diffraction data around the $(222)_{cub}$ Bragg reflection were carefully measured as a function of temperature. The results obtained at some selected temperatures are shown in Figure 8.1 (all diffraction data are intensity normalized by the maximum of the peak value of the $(222)_{cub}$ reflection at each temperature, *i.e.* I / I_{max}). The peak at 415 K appears sharp and symmetric with an instrument resolution-limited width, indicating the cubic structure (in accordance with all the previously published results) and the excellent quality of the crystal. On the other hand, the bottom of the peak is slightly broadened, more pronounced at the lower angle side. To visualize this fact better, the profile is shown separately in semi-logarithmic scale in Figure. 8.2(a). This kind of base-broadening of X-ray and neutron diffraction peaks in PMN-based relaxors is usually related to the correlations in the displacements of atoms, originating from the polar nanoregions (PNRs). [79, 141,].

In PZN this effect was also reported in the high-temperature phase, but only for the neutron scattering [140]. The full profile can be well fitted by the sum of Gaussian (solid line at the central of peak [Figure 8.2 (a)]) and Lorentzian (broken line that overlapped with the peak profile at the tail [Figure 8.2 (a)]) functions. It is stated that the electron density in the vicinity of the peak maximum is approximately Gaussian [83]. Thus it is understandable that the central Bragg peak of X-ray diffraction is Gaussian type. However, when the tails are very pronounced, it is not sufficient to fit these lines with a unique Gaussian profile. The diffuse scattering on the tails can be related to the presence of PNRs. Because the PNRs display a local polar structure (short range order) that is different from the cubic matrix long range order, the lattice mismatching between the PNRs and the surroundings can cause the diffuse scattering. This scattering is partially coherent with that of the cubic host lattice on one hand, and is strongly deviated from the cubic symmetry on the other hand [142]. The diffuse scattering characteristic of the PNRs is best fit by a Lorentzian distribution of X-ray diffraction, as evidenced on the fitting profile of the tails. Note that these two functions are centered at slightly different θ values, and the fitting is disturbed at the angles far from the center.

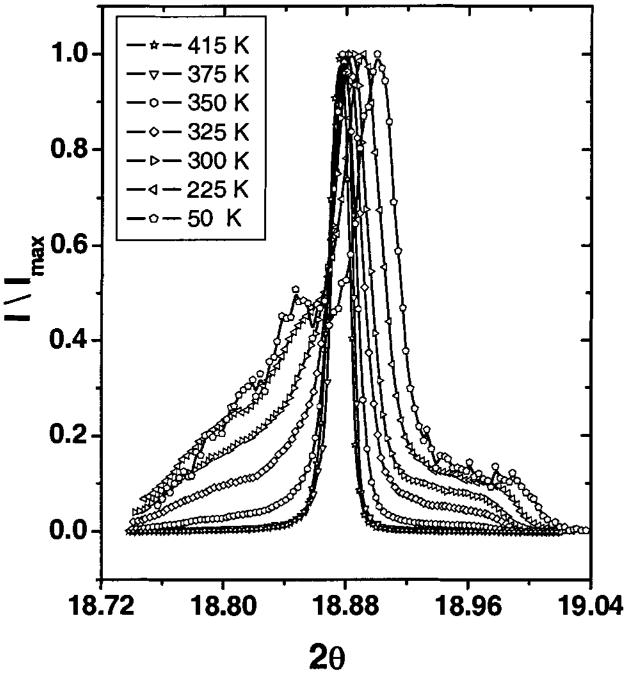

Figure 8.1: Diffraction pattern around the $(222)_{cub}$ peak for PZN crystal at selected temperatures between 50 K and 415 K (with intensity normalized by I / $I_{max.}$).

The spectrum at 375 K is almost identical to that of 415 K. But at lower temperatures the distinctive shoulders begin to appear from both sides of the peak. Upon further cooling, these shoulders become more and more significant. At low temperatures two peaks expected for the rhombohedral phase are clearly visible, but surprisingly, besides these two peaks, the significant shoulders still remain. This means that an additional phase (or phases) not noticed in the previous investigations exist in PZN crystal alongside with the rhombohedral phase.

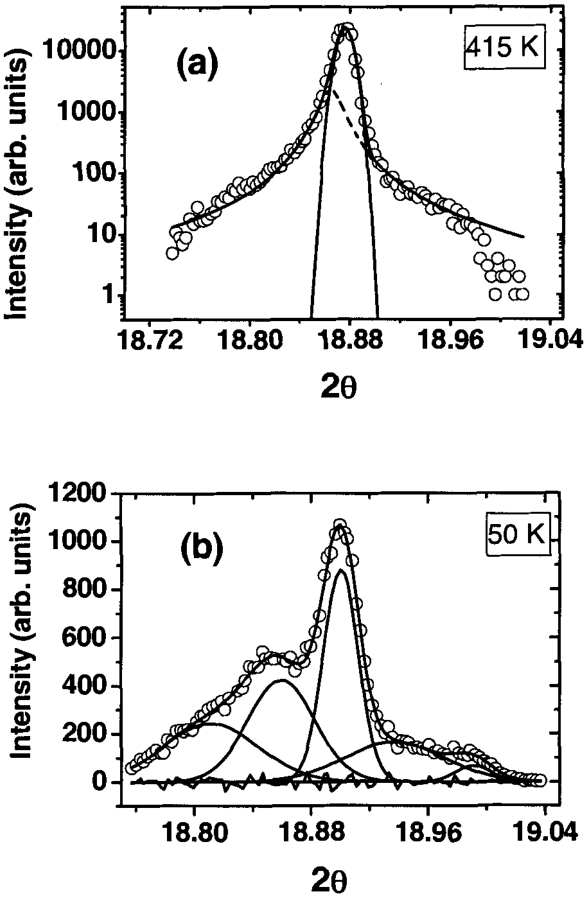

Figure 8.2: Fitting of the diffraction pattern around the $(222)_{cub}$ peak for PZN crystal at: (a) 415 K and (b) 50 K. Circles represent experiment data; Gaussians and Lorentzian used for fitting are represented by solid and broken lines, respectively.

In the temperature interval of 50 - 325 K the full line profile can be well fitted as a sum of five overlapping Gaussian function. Figure 8.2(b) demonstrates the fit at 50 K as an example. Two central contributions (i.e. those that give rise to the maximums on the diffraction profile) can be assigned to the rhombohedral phase [$(222)_R$ and $(\bar{2}22)_R$ reflections correspond to low-angle and high-angle maximums, respectively]. The remaining three contributions are related to the other phase of lower (probably a monoclinic or triclinic) symmetry.

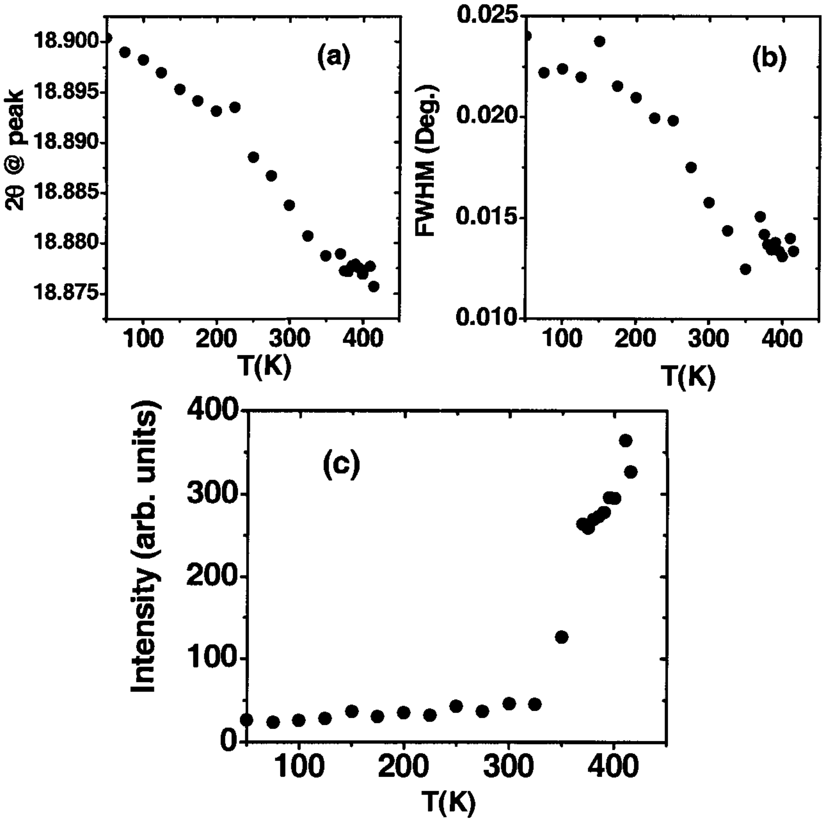

Figure 8.3: Variations of (a) two-theta (2θ) values, (b) full-width-at-half-maximum (FWHM), and (c) integrated intensity of the major $(222)_{cub}$ peak as a function of temperature for PZN crystal.

The summarized intensity of the peaks related to the low symmetry phase (calculated as the sum of intensities of the corresponding fitted peaks) accounts for about 40% of the total intensity of all peaks, which means that this low-symmetry phase exists at a significant concentration. However, the magnitudes of the peaks of this phase are comparatively small for two reasons: i) the intensity is distributed over more than three peaks, and ii) the peaks are wider, e.g. at 50 K the values of the full width at half maximum (FWHM) are about 0.07 ° for the two most intense peaks of the low symmetry phase, which is much larger than the $(\bar{2}22)_R$ peak (0.024 °) and the $(222)_R$ peak (0.046 °).

The small magnitude of those peaks explains why they can be reliably detected only with the help of synchrotron X-ray diffraction having both the intensity and resolution much higher than the conventional X-ray technique.

Note that the central peak, which is single at high temperatures, remains the dominant peak throughout the cooling down to 50 K. Figure 8.3 shows the variations of the position (in 2θ), FWHM and intensity of this peak as a function of temperature. It can be seen that the FWHM and the angle of peak position increase upon cooling, first very slowly, but much more quickly starting from about 350 K. A sharp drop of peak intensity is also observed between 325 and 370 K, i.e. in the temperature range where the shoulders around the major peak become very pronounced. The line profile cannot be unambiguously fitted in this temperature range. All these features provide evidence for a phase transition. Our results are consistent with the recent study of the (333) and (005) lines of PZN [138], in that the phase transition is diffuse, i.e. in the temperature interval of 325-390 K the cubic phase transforms progressively into the domains of the ferroelectric phase so that the different phases coexist in this interval. Indeed, as mentioned above, the distinguishable shoulders around the central peak, signifying the presence of the low-symmetry phase (or phases) were observed already at 385 K. With decreasing temperature these shoulders gradually grow because of the increase of the concentration of the low-symmetry phase. Due to the fact that the lattice plane spacing in the $[111]_{cub}$ direction is very close in the cubic and rhombohedral phases (*i.e.* the unit cell changes during the transition in such a way that its dimension in one of the $<111>_{cub}$ direction remains unchanged) [138], the rhombohedral $(\bar{2}22)_R$ and cubic $(222)_C$ reflections are superimposed and cannot be resolved, that is why only a single peak composed of these two contributions can be observed in this temperature range. Because of the decrease of the concentration of the cubic phase on cooling, the intensity of this peak decreases (Figure 8.3c) and below about 325 K remains almost temperature-independent, which means that the diffuse phase transition is completed.

Figure 8.4 presents the temperature dependencies of the lattice parameters *a* and α and the unit cell volume calculated for the cubic and rhombohedral phases in the PZN crystal. The anomaly around 350 K clearly indicates the phase transition. The value of α in the low-temperature R3m phase agrees satisfactorily with that reported for this phase in Ref. [138] and is approximately the same value as in the rhombohedral phase of normal perovskite ferroelectrics. Interestingly, the variation of the rhombohedral lattice constant *a* below the transition temperature (Figure. 8.4) shows the same trend as that of the PMN [79, 143], reflecting the relaxor behavior of PZN even in the low temperature phase(s). The width of the diffraction peaks below the phase transition temperature is much larger than in the high-temperature cubic phase. Figure 8.3(b) illustrates the FWHM for the major peak. The widths of other peaks are even larger. This effect is usually explained by the small size of ferroelectric domains. The other, probably more important, reason for this in PZN is the internal elastic microstrains caused by the coexistence of different ferroelectric phases. The spontaneous deformations of the parts of the crystal containing different phases are different, which leads to internal stresses and strains. Spontaneous deformation usually increases with decreasing temperature, which is confirmed in our case by the increase of the rhombohedral angle in Figure 8.4. As a result, the FWHM also increases with decreasing temperature (Figure 8.3).

Additional line broadening can also arise from a dispersion in lattice parameters, which depends on the distance from the crystal surface [139].

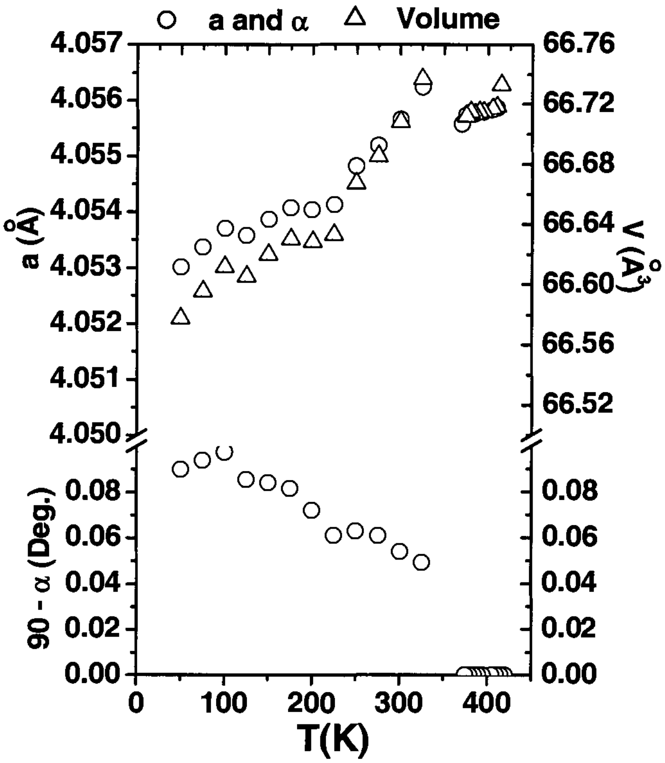

Figure 8.4: Variations of lattice parameters, *a* and α, and the unit cell volume, as a function of temperature for the rhombohedral and cubic phases of PZN crystal

Using the Scherrer equation, the size of ferroelectric domains was estimated from the difference between the squares of the instrumental FHWM and the FHWM observed at 300 K (i.e. at a comparatively high temperature, where the broadening related to internal strains is not very large). For the rhombohedral phase we derive a size of ~70 nm and ~200 nm from $(222)_R$ and $(\bar{2}22)_R$ peaks, respectively. This means that the domain size in one of the directions (perpendicular to the spontaneous polarization vector) is larger than in the other directions, i.e. the domains have an anisotropic form. Note that in Ref. [138]

all the dimensions of the rhombohedral domains in PZN were estimated to be the same size (60-70 nm). This discrepancy can be explained by a longer X-ray wavelength used in that work leading to a smaller penetration depth (the structure of PZN is known to depend on the distance from crystal surface [139]). The domain size of the new phase is estimated to be in the range of 40 – 80 nm, depending on the direction.

8.4.2 Dielectric Properties

Figures 8.5(a) and 8.5(b) show the variations of the real part of the dielectric permittivity ε' and the dissipation factor $\tan\delta$ as a function of temperature at various frequencies, measured upon zero electric field cooling (ZFC) for the $(111)_{cub}$ PZN crystal. The strong frequency dispersion of the dielectric constant with temperature of the maximum, T_{max} increasing at higher frequencies, indicates the typical relaxor ferroelectric behavior. The temperature T_{max} varies from 417 K at 100 Hz to 429 K at 1 MHz. As in other relaxors, the frequency f dependence of T_{max} can be fitted with the Vogel-Fulcher relation:

$$f = f_0 \exp[-E_a/(T_{max}-T_0)] \quad , \qquad (8.1)$$

where f_0, E_a, and T_0 are the parameters, as shown in Figure 8.5(c). The same fit, but with a different set of parameters can be applied to the frequency and temperature dependence of the imaginary permittivity maximum (shown Figure 8.5(c)). The best-fit results are presented in Table 8.1. It is worth noting that below T_{max} no evidence of the structural phase transition, which was detected between 390 and 325 K in the above mentioned X-ray diffraction experiments, can be observed in the dielectric properties.

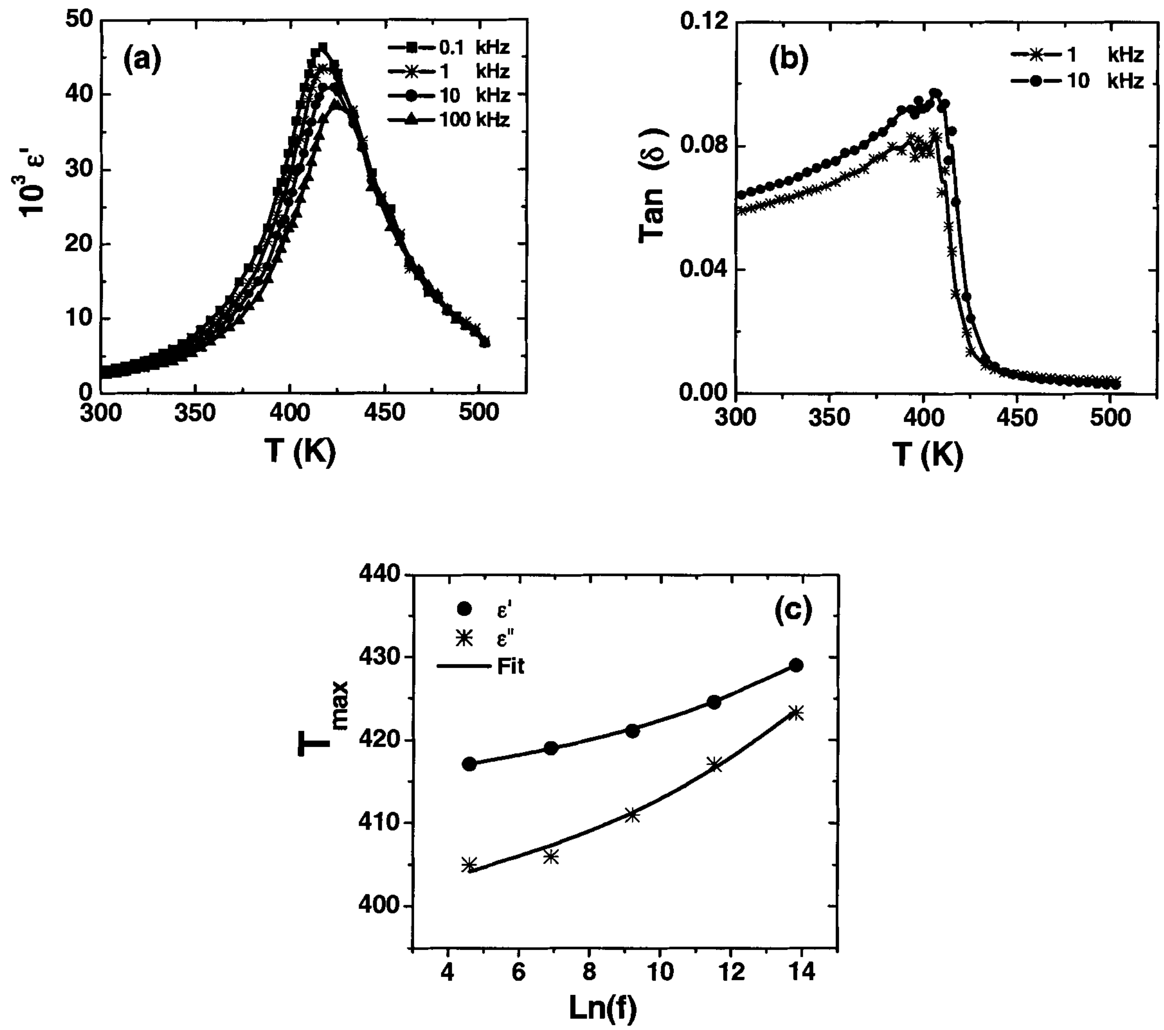

Figure 8.5: Variations of, (a): the real part of dielectric permittivity, and (b): the dissipation factor, as a function of temperature for PZN crystal upon cooling at zero-field (ZFC) measured at different frequencies. (c): Frequency dependencies of the temperature (T_{max}) of maximum permittivity (circle for real part and stars for imaginary part) and the fitting (solid line) to the Vogel-Fulcher relation.

Table 8.1: Fitting parameters of the Vogel –Fulcher relation for the temperatures of maximum real and imaginary permittivities obtained under different conditions

	ZFC		FC		ZFH after poling	
	ε′	ε″	ε′	ε″	ε′	ε″
f_0 (Hz)	$3x10^{10}$	$8x10^{10}$	$5x10^{10}$	$2x10^8$	$3x10^9$	$5x10^{11}$
E_a (K)	263	488	332	165	206	526
T_0 (K)	403	380	393	392	401	377

Figure 8.6(a) shows the temperature dependence of the real permittivity of the unpoled crystal measured at various frequencies upon cooling under a dc bias field of 1.2 kV/cm (FC). The strong dispersion due to relaxor relaxation around T_{max} remains. However, at T_C = 390 K, the dielectric constant undergoes a discontinuous change in slope with the values at different frequencies merging together and dropping sharply. Below T_C the frequency dispersion is attenuated dramatically. The dielectric relaxation around T_{max} can also be fitted with the Vogel-Fulcher relation for both the real and imaginary parts of permittivity [in Figure 8.6(b)], with the fitting parameters given in Table 8.1.

Figure 8.7(a) presents the temperature and frequency dependencies of the dielectric constant of the PZN crystal prepoled at room temperature (at 20 kV/cm), which were measured upon zero-field-heating (ZFH after poling). In the low temperature range, the permittivity is almost non-dispersive. Upon further heating, a sharp peak of dielectric constant occurs at T_C = 388 K. Above T_C, the strong dielectric dispersion, characteristic of relaxor relaxation, reappears, suggesting that the PZN crystal reenters the relaxor state. The transition temperature T_C does not depend on frequency, as opposed to the behavior of T_{max}. The frequency dependence of the latter can also be well fitted into the Vogel-Fulcher law [Figure 8.7(b)] with the fitting constants provided in Table 8.1.

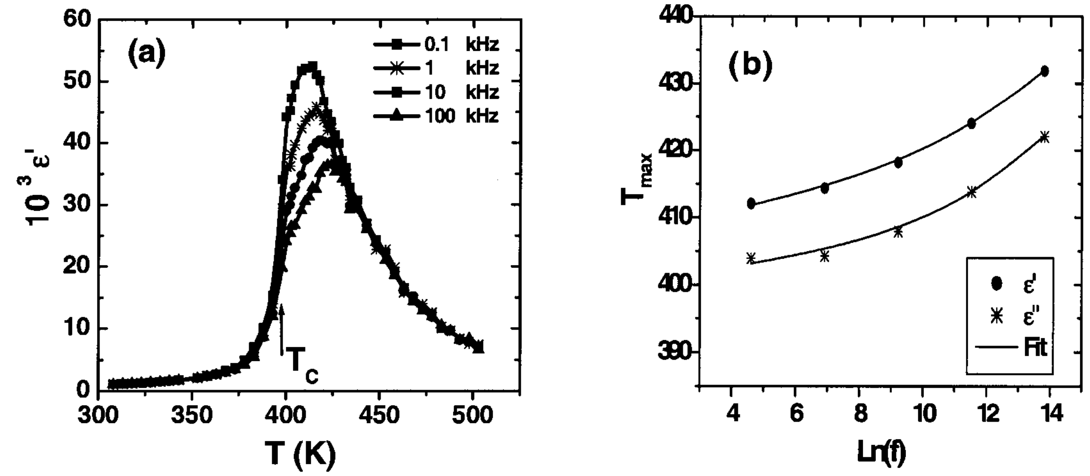

Figure 8.6: Variation of the real part of dielectric permittivity measured at different frequencies as a function of temperature for PZN crystal upon: (a) cooling under a field of 1.2 kV/cm, and (b) the Vogel-Fulcher relation.

It is interesting to note that i) above T_C the electric field almost has no effect on the dielectric relaxation behavior around T_{max}, which can be fitted into the Vogel-Fulcher relation with fitting parameters only slightly different from those of ZFC, ii) the sharp anomalies of the dielectric constant upon ZFH after poling and upon FC are observed at approximately the same temperature as T_C = 390 K, where the diffuse phase transition begins upon ZFC, as revealed by synchrotron X-ray diffraction experiments.

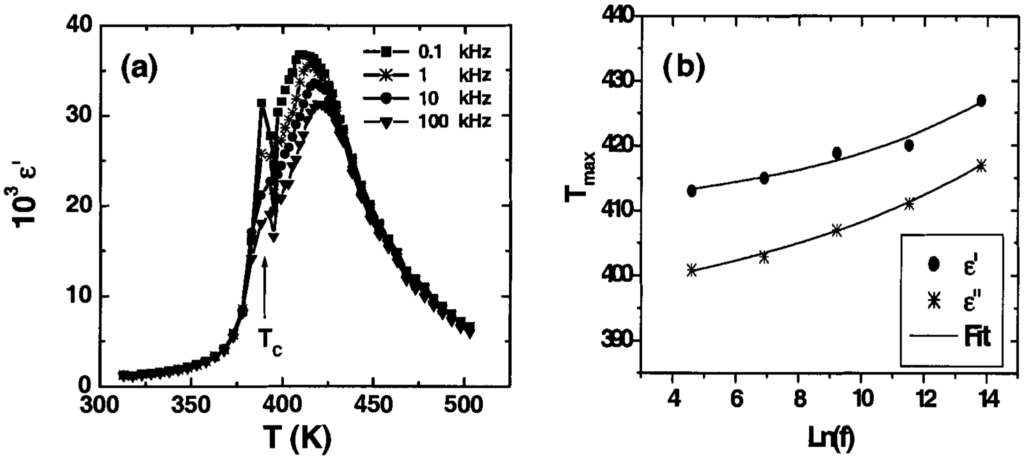

Figure 8.7: Variation of the real part of dielectric permittivity measured at different frequencies as a function of temperature for PZN crystal upon: (a) heating after poling at room temperature and (b) the Vogel-Fulcher relation.

8.5 Discussion

Let us discuss the structure of the PZN crystals studied in this work by comparing them with the well-documented prototypical relaxor ferroelectric PMN (see e.g. Ref. [126]). The structures of PMN and PZN at high temperatures (around T_{max} and above) are similar. It is usually believed that in PMN the structure is macroscopically cubic with the nanometric inclusions of polar order. In PZN the existence of PNRs have recently been deduced from neutron scattering experiments in Ref. [140] and confirmed in the present work by the observed broadening of the bases of the diffraction peak. On the other hand, the low-temperature structures of these two materials are quite different. In PMN the X-ray and neutron diffraction investigations do not indicate any macroscopic distortion of the cubic lattice. PZN, on the contrary, exhibits the reduction of symmetry below about 350 K where we observed the splitting of (222) lines. Two central contributions (peaks) can be attributed to the rhombohedral phase which was also observed in the previous investigations (e.g. in Ref. [138]). In addition, we have revealed the presence of another low-symmetry phase with a significant concentration which was not reported before [the present data do not allow us to determine the symmetry and the type (ferroelectric or antiferroelectric) of this low-symmetry phase; (such an investigation is underway. We also confirmed that the phase transition in PZN is diffuse, i.e. the high-temperature cubic phase and the low-temperature phases coexist in a temperature interval of several dozens of degrees.

Note that the studies of the PZN crystal using neutron and high-energy (67 keV) X-ray diffraction revealed a different low-temperature phase (the so-called X-phase) but not the rhombohedral one [139, 140, 144]. The X-phase exhibits a cubic unit cell. It was not observed in this work, nor was it in other works in which low-energy X-ray was used. This discrepancy can be explained [139] by the small penetration capability of low-energy radiation, so that it probes only the parts of the crystal not far from the surface ("skin"). The X-phase seems to be located in the bulk and can be detected only by high-energy radiation. As the phase content depends on the distance from the crystal surface (X-phase inside, "normal" phases at the surface), one can suspect that the rhombohedral phase and the additional low-symmetry phase discovered in this work are also separated in space. Further experiments are needed to determine if these two phases are mixed homogeneously or exist separately.

The important point to underline here is that, the PNR-related diffuse scattering giving rise to the tails around the sharp $(222)_{cub}$ Bragg peak at high temperatures has been observed in our X-ray diffraction experiments. This means that PNRs exist not only in the crystal bulk, transforming to the X-phase upon cooling, but also in the "skin" of the crystal which undergoes the transition into the phases with normal ferroelectric distortion. This may suggest that different local symmetry prevails in different PNRs so that they can develop upon cooling into the ferroelectric domains of different symmetry. As a result at least two phases are present in PZN at low temperatures.

8.6 Conclusions

We have shown in this study that the $Pb(Zn_{1/3}Nb_{2/3})O_3$ crystal is a unique example of relaxor in which, in contrast to the classical relaxor PMN, the spontaneous (i.e. without external electric field) ferroelectric phase transition occurs, but, in contrast to some other relaxors exhibiting sharp spontaneous transition to a ferroelectric phase [e.g. $Pb(Sc_{1/2}Nb_{1/2})O_3$], this transition is diffuse and observed only near the surface of the crystal. As detected by high-resolution synchrotron X-ray diffraction in the absence of an electric field, PZN crystals undergo a diffuse structural transformation from the high-temperature state, which is macroscopically cubic and contains polar nanoregions typical of relaxors, to the low-temperature state composed of the mesoscopic domains of the rhombohedral ferroelectric phase and a second phase with lower symmetry. On cooling the domains of these low-temperature phases begin to appear at T_C = 390 K and grow progressively at the expense of the cubic phase. Below T = 325 K the cubic phase is no longer observable. The so-called X-phase recently discovered in the central (bulk) parts of PZN crystal with the help of high-energy X-ray and neutron diffraction, was not observed in the present work because the X-ray energy used (32 keV) was not high enough to penetrate deeply into the crystal.

The dielectric properties show typical relaxor ferroelectric behavior with the broad and dispersive peak of dielectric constant at T_{max} = 415 K > T_C, which can be fitted into the Vogel-Fulcher relation, while no clear anomalies in dielectric properties can be associated with the structural phase transformation at ~T_C. Application of an electric field (1.2 kV/cm) upon cooling induces a comparatively sharp phase transition at T_C = 390 K with the establishment of the ferroelectric phase with macroscopic domains, as revealed by the anomaly in the temperature dependence of dielectric constant at T_C and the disappearance of significant dielectric dispersion below T_C. The state induced upon field-cooling collapses under ZFH at T_C in the form of a sharp phase transition with the breaking down of the macro polar domains back into the relaxor state. The relaxor behavior is fully recovered with typical relaxor dielectric relaxation around T_{max} = 415 K and the same fitting parameters to the Vogel-Fulcher relation.

The behaviour of the dielectric permittivity and phase transition of the PZN crystal will be discussed in **Chapter 9** in comparison with relaxor $Pb(Sc_{1/2}Nb_{1/2})O_3$ and $Pb(Mg_{1/3}Nb_{2/3})O_3$ in the light of the kinetic model of phase transitions in disordered crystals and the model of "soft nanoregions" in relaxors.

Chapter 9:
General Summary, Discussion and Conclusions

In this Chapter, we summarize the experimental results in the different parts of the work on the (1-x)$Pb(Sc_{1/2}Nb_{1/2})O_3$ – $x$$PbTiO_3$ and (1-x)$PbSnO_3$ – $x$$PbTiO_3$ solid solutions. Their piezoelectric properties are compared with the excellent piezoelectric systems, (1–x)$PbZrO_3$ – $x$$PbTiO_3$ (PZT), $Pb(Zn_{1/3}Nb_{2/3})O_3$ – $PbTiO_3$ (PZN–PT) and $Pb(Mg_{1/3}Nb_{2/3})O_3$ – $PbTiO_3$ (PMN–PT). The common features of the morphotropic phase boundary behaviour for these materials are described. In addition, the phase transition in relaxor $Pb(Sc_{1/2}Nb_{1/2})O_3$, $Pb(Zn_{1/3}Nb_{2/3})O_3$ and $Pb(Mg_{1/3}Nb_{2/3})O_3$ single crystals, as revealed by the dielectric spectroscopic and X-ray studies, are discussed in the light of a kinetic model of phase transitions in disordered systems.

Overall, this thesis work can be summarized into five parts:

i. Materials synthesis and development;

ii. Effects of growth conditions on the structural order/disorder, phase transition and domain structure;

iii. Structural characterization and morphotropic phase boundary behaviour;

iv. Dielectric, piezo- and ferro- electric properties of (1–x)$Pb(Sc_{1/2}Nb_{1/2})O_3$–$x$$PbTiO_3$ and (1-x)$PbSnO_3$ – $x$$PbTiO_3$;

v. Microscopic mechanism of phase transitions in relaxor $Pb(Sc_{1/2}Nb_{1/2})O_3$, $Pb(Zn_{1/3}Nb_{2/3})O_3$ and $Pb(Mg_{1/3}Nb_{2/3})O_3$ ferroelectrics.

9.1 Materials Synthesis and Development

9.1.1 Synthesis of the $(1-x)Pb(Sc_{1/2}Nb_{1/2})O_3 - xPbTiO_3$ Solid Solution in the Forms of Ceramics and Single Crystals.

Owing to its interesting properties, a relatively high Curie temperature (≥ 240 °C) and potential piezoelectric applications, solid solutions of $(1-x)Pb(Sc_{1/2}Nb_{1/2})O_3 - xPbTiO_3$ (PSN–PT) with compositions within the morphotropic phase boundary (MPB) region ($0.35 \leq x \leq 0.50$) have been synthesized in the pure perovskite phase by an improved two-step wolframite precursor method (**Chapter 3**).

Perovskite PSN-PT single crystals with composition near the MPB have been grown by an improved flux method. The growth conditions were optimized in terms of the chemical compositions and discussed in the light of thermodynamics and kinetics of crystal growth (**Chapter 4**). It is found that the morphology, the quality, and the chemical and physical properties of the grown crystals are affected by the growth conditions, such as the ratios of PSNT/Flux and PbO/B_2O_3. By adjusting the chemical and thermal parameters, optimum growth conditions have been found, which lead to the growth of PSN–PT single crystals of good quality. The investigations of the dielectric permittivity and the X-ray analysis on the grown PSN–PT single crystals show the typical character of the MPB behaviour for a relaxor–$PbTiO_3$ solid solution, namely with the presence of two anomalies observed in the dielectric permittivity measurements $\varepsilon(T)$, and a monoclinic symmetry revealed by X-ray diffraction.

9.1.2 Effects of Growth Conditions on the Chemical Order/Disorder, Phase Transition and Domain Structure

The studies of the $Pb(Sc_{1/2}Nb_{1/2})O_3$ (PSN) (**Chapter 5**) and $(1-x)Pb(Sc_{1/2}Nb_{1/2})O_3 - xPbTiO_3$ (PSN–PT) (**Chapter 6**) single crystals revealed that the chemical and physical properties of the materials are affected by the growth conditions. PSN crystals that grew at temperatures 1000 – 1180 °C (Table 5.1) are chemically disordered and show a spontaneous phase transition, upon cooling, first from the paraelectric to a relaxor, then to a normal ferroelectric state. The domain observation of the PSN sample confirmed the existence of domain states with probably rhombohedral symmetry at room temperature. However, PSN crystals grown at higher temperatures (above 1200 °C) show the chemically ordered structure but exhibit a much broader $\varepsilon(T)$ dielectric peak, and the transition from relaxor to normal ferroelectric is suppressed. The dielectric permittivity of the disordered $Pb(Sc_{1/2}Nb_{1/2})O_3$ single crystal exhibits typical relaxor characteristics (**Section 5.5**), i.e., the frequency dispersion of the dielectric permittivity follows the Vogel – Fulcher relationship in a certain frequency range, and the high-temperature slope of the permittivity peak follows a quadratic Lorentz law in a wide temperature range. An interesting observation is that the values of T_C, T_f and T_A are approximately the same. This supports the conclusion of Ref. [19] that T_f is not necessarily a freezing temperature of the relaxor system; rather it is the temperature at which the relaxor to ferroelectric phase transition takes place.

On the other hand, the PSN–PT single crystals of solid solution show a more complex behaviours caused by a higher degree of chemical disorder on the B-site randomly occupied by three cations (Sc^{3+}, Nb^{5+}, and Ti^{4+}), and by the formation of a morphotropic phase boundary (MPB) as the Ti^{4+} concentration is increased.

9.1.3 A New Family of Piezoelectric Single Crystals: (1-x)$PbSnO_3 - x PbTiO_3$

A new family of piezocrystals, (1-x)$PbSnO_3$ – $x$$PbTiO_3$ (PbSnTi), has been disclosed (**Chapter 7**). Single crystals of the PbSnTi solid solution system have been successfully grown for the first time by a high temperature solution method using ($PbO+B_2O_3$) as flux. X- ray diffraction confirms the perovskite structure.

9.2 Structural Characterization and Morphotropic Phase Boundary Behaviour

The study of the morphotropic phase boundary (MPB) phenomena constitutes an important part of this work. The MPB phase diagram of the $(1-x)Pb(Sc_{1/2}Nb_{1/2})O_3-xPbTiO_3$ solid solution system has been established by means of dielectric measurements and X-ray structural analysis (**Section 3.5**). It shows an MPB region, in which a complex phases mixture with the presence of a monoclinic phase (Figure 3.13). PSN–PT with composition within the MPB region (Figure 3.11) typically exhibits two phase transitions at T_C and T_{MPB}, as revealed by the dielectric anomalies. The substitution of the Ti^{4+} ion for the complex $(Sc_{1/2}Nb_{1/2})^{4+}$ ions, i.e. with increasing x, gives rise to an increase in T_C and decrease in T_{MPB}. The dielectric permittivity and the differential scanning calorimetry (DSC) (Figure 3.10) show a clear peak at T_C, at which the transition from the paraelectric to ferroelectric phase takes place. Two anomalies are detected in the spectra of dielectric constant as a function of temperature for (1-x)PSN–xPT with the compositions of $0.35 \leq x \leq 0.42$, while only one anomaly is observed for the compositions of x = 0.45 and 0.50. Analysis of the X-ray powder diffraction patterns reveals that for compositions $0.37 \le x \le 0.42$ the spectra cannot be resolved by a single phase model using Lorentzian functions, nor by a simple mixture of a tetragonal (T) and a rhombohedral (R) phase. Instead, a lower symmetry phase of monoclinic (M) symmetry is found to be present. A sequence of structural changes from the rhombohedral (R) phase ($x \le 0.35$), to the monoclinic M+δT ($0.35 < x < 0.45$), to the tetragonal T+δM ($0.45 \le x \le 0.50$) and then to the tetragonal (T) phase ($x > 0.50$) are proposed. Based on these results, a revised phase diagram of the PSN–PT solid solution has been established. It indicates the MPB region and a curved upper boundary.

Single crystals of $0.40PbSnO_3 - 0.60PbTiO_3$ also exhibit two phase transitions (Figure 7.6) at T_C and T_{MPB}, respectively, indicating the typical MPB behaviour (the detailed phase diagram is still under investigation). The temperature dependence of the permittivity indicates a Curie temperature of 206 °C, for compositions within the morphotropic phase boundary (MPB), which are much higher than the T_C of the PMN–PT or PZN–PT piezocrystals of MPB composition. A second dielectric anomaly is observed at T_{MPB} = 190 °C, which is also higher than that of PMN-PT and PZN-PT crystals.

If we compare the MPB phase diagram of $(1-x)Pb(Sc_{1/2}Nb_{1/2})O_3 - xPbTiO_3$ solid solution with PZT, PZN–PT and PMN–PT systems, we can see that the phase diagrams of all the above solid solutions show some common features, such as the curvature of the MPB upper limit boundary, and the presence of an intermediate lower symmetry phase acting as a bridge connecting the rhombohedral (R) and the tetragonal phases (T), etc. Interestingly, the dielectric and piezoelectric properties are enhanced in the materials of

MPB compositions. Therefore, the establishment of the phase diagram of the PSN-PT solid solution with the monoclinic symmetry lying in between R-phase and T-phase gives another example of an MPB system, useful for understanding the MPB behaviour and the very high electromechanical response in these materials. These results allow us to classify the PSN-PT and PbSnTi systems into the same class as the PZT, PMN–PT and PZN–PT systems, providing useful information for developing new piezoelectric crystals for wider temperature range applications.

9.3 Dielectric, Piezo- and Ferro- electric Properties of $(1-x)\mathrm{Pb}(\mathrm{Sc}_{1/2}\mathrm{Nb}_{1/2})\mathrm{O}_3 - x\mathrm{PbTiO}_3$ and $(1-x)\mathrm{PbSnO}_3 - x\mathrm{PbTiO}_3$

The dielectric and piezoelectric properties of the <001>-oriented $(1-x)\mathrm{Pb}(\mathrm{Sc}_{1/2}\mathrm{Nb}_{1/2})\mathrm{O}_3 - x\mathrm{PbTiO}_3$ (PSN–PT) (**Chapter 4**) and $(1-x)\mathrm{PbSnO}_3 - x\mathrm{PbTiO}_3$ (PbSnTi) (**Chapter 7**) single crystals have been characterized. Table 9.1 lists the measured values of the room temperature dielectric constant ε and loss, the Curie temperature T_C and MPB phase transition temperature T_{MPB}, the longitudinal electromechanical coupling factor k_{33} and the piezoelectric coefficient d_{33} at room temperature. The corresponding properties of the PZT ceramics, <001>-oriented PMN–PT and PZN–PT single crystals are also listed for comparison. It can be seen that the dielectric (ε' and $\tan\delta$) and piezoelectric (k_{33}, d_{33}) properties of the PSN–PT and PbSnTi crystals are comparable with those of the PZT ceramics. Even though their properties are lower than those of the PMN–PT and PZN–PT with MPB composition, the T_C, and especially T_{MPB}, of the PSN–PT and PbSnTi crystals are much higher than that in the PMN–PT and PZN–PT crystals. This suggests that, upon optimization of the MPB composition and properties, the PSN–PT and PbSnTi single crystals can be new resource of high piezoelectric crystals with high T_C and high T_{MPB}, potentially useful for a wide range of electromechanical transducer applications.

Table 9.1: Dielectric and piezoelectric properties of the <001>-oriented $(1-x)Pb(Sc_{1/2}Nb_{1/2})O_3-xPbTiO_3$ and $(1-x)PbSnO_3-xPbTiO_3$ single crystals compared with PZT ceramics and <001>-oriented PMN–PT and PZN–PT single crystals

Materials	ε' (RT)	loss	T_C (°C)	T_{MPB} (°C)	k_{33}	d_{33}, pC/N)	Applications
57PSN–43PT crystal[a)]	960	0.03	227	/	0.78	310	High – T_C transducers
49PSN–51PT crystal[a)]	970	0.02	250	219	0.73	330	High – T_C transducers
40PbSnO$_3$–60PT crystal[a)]	1440	0.004	206	190	0.73	370	High – T_C transducers
Type-II* PZT ceramic[b)]	2050	0.018	340	/	0.73	400	Accelerometer, Actuators, Flow meters, Hydrophones
Type-III* PZT ceramics[b)]	1000	0.003	300	/	0.64	225	Sonar projectors, Cleaners, Therapeutic, Ultrasound
Type VI* PZT ceramics[b)]	3900	0.025	210	/	0.79	690	Medical imaging, Transducers, Actuators, Hydrophones
PZN–4.5%PT crystals[b)]	5000	0.01	155	120*	0.92	2200	Medical imaging, Actuators, Sonar, Accelerometers
PMN–30%PT crystals[c)]	5000	0.005	138	98	0.89	1600	Medical imaging, Actuators, Sonar, Accelerometers

[a)] This work; [b)] Ref. [1]; [c)] Ref. [66]

*see Appendix I for descriptions.

9.4 The Microscopic Mechanism of Phase Transitions in Relaxor $Pb(Sc_{1/2}Nb_{1/2})O_3$, $Pb(Zn_{1/3}Nb_{2/3})O_3$ and $Pb(Mg_{1/3}Nb_{2/3})O_3$ Ferroelectrics

This section is revised from the paper published in ***J. Phys.: Condens. Matter.*** by **Y-H. Bing, A. A. Bokov, Z.-G. Ye, B. Noheda and G. Shirane**, ["Structural Phase Transition and Dielectric Relaxation in $Pb(Zn_{1/3}Nb_{2/3})O_3$ Single Crystals", Volume 17, Number 15, pp. 2493-2507, 20 April (2005)]. The reproduction of this paper is by permission of IOP Publishing Limited. Publisher's Internet address: www.iop.org/journals/jpcm.

From the studies of the dielectric properties and phase transitions of $Pb(Sc_{1/2}Nb_{1/2})O_3$ (PSN) (**Chapter 5**), and $Pb(Zn_{1/3}Nb_{2/3})O_3$ (PZN) (**Chapter 8**) single crystals, it is interesting to compare the behaviour of PSN with PZN and the well-documented prototypical relaxor ferroelectric PMN [126] and to discuss the behaviour of the phase transitions. As mentioned in **Chapter 5**, PSN exhibits a spontaneous relaxor to ferroelectric phase transition. The characteristic diffuse $\varepsilon(T)$ peak exhibiting the Vogel-Fulcher frequency dependence of T_{max} is accompanied by a dielectric anomaly at several degrees below T_{max}. This anomaly is related to the spontaneous (i. e. without external field) transition to the ferroelectric phase upon cooling and it can be very sharp. Below the phase transition temperature, a well-defined ferroelectric phase exists.

In PZN and PMN, however, the sharp phase transition from relaxor to ferroelectric phase in the temperature dependencies of permittivity and losses is initially absent at zero field, but can be induced by applying a strong enough electric field upon cooling.

In PMN the X-ray and neutron diffraction investigations do not indicate any macroscopic distortion of the cubic lattice down to very low temperature, far below the temperature of maximum permittivity (T_{max} = 265 K, at 1 kHz) [79]. The earlier studies [104, 45] revealed that, in PMN, a ferroelectric phase can be induced either by application of an electric field along $[111]_{cub}$, or by partial substitution of Ti^{4+} for the complex $(Mg_{1/3}Nb_{2/3})^{4+}$ ions. In both cases, the micropolar domains transform into macrodomains with cubic-to-rhombohedral symmetry breaking [53, 104]. Based on the experimental data obtained from high-resolution synchrotron X-ray diffraction, the structure analysis [79] in PMN–5%PT revealed that the substitution of Ti^{4+} at a PT concentration as low as 5% results in the development of a clean rhombohedral phase. A spontaneous relaxor to normal ferroelectric phase transition, similar to that in PSN, also can be observed in $Pb(Mg_{1/3}Nb_{2/3})O_3$ – $PbTiO_3$ solid solutions with high concentration of $PbTiO_3$ [25, 26, 27].

The structure and properties of the PZN crystals described in **Chapter 8**, show that the behavior of the PZN crystals sits in an intermediate position between the behavior of prototypical relaxor PMN and that of PSN crystals. The spontaneous transition to the ferroelectric phase is observed in PZN, but this transition is diffuse and thus it is not associated with the sharp dielectric anomalies. By application of an electric field (1.2 kV/cm), a sharp decrease in dielectric permittivity at T_C can be induced.

On the other hand, the temperature and frequency dependences of the dielectric permittivity look very similar in the PZN, PMN and in PSN crystals at $T > T_C$, with observed broad and high $\varepsilon(T)$ peak and strong dispersion causing the Vogel-Fulcher type shift of T_{max} with frequency. Moreover, in all the cases, the high-temperature slope of the diffuse permittivity peak can be scaled by a quadratic function [31].

It is shown in **Chapter 8** that the size of the ferroelectric domains in PZN is considerably smaller than the size of normal ferroelectric domains, but larger than the size of polar nanoregions (PNR) in PMN. It seems that the size of the ferroelectric domains in PSN is even larger than that in PZN crystal.

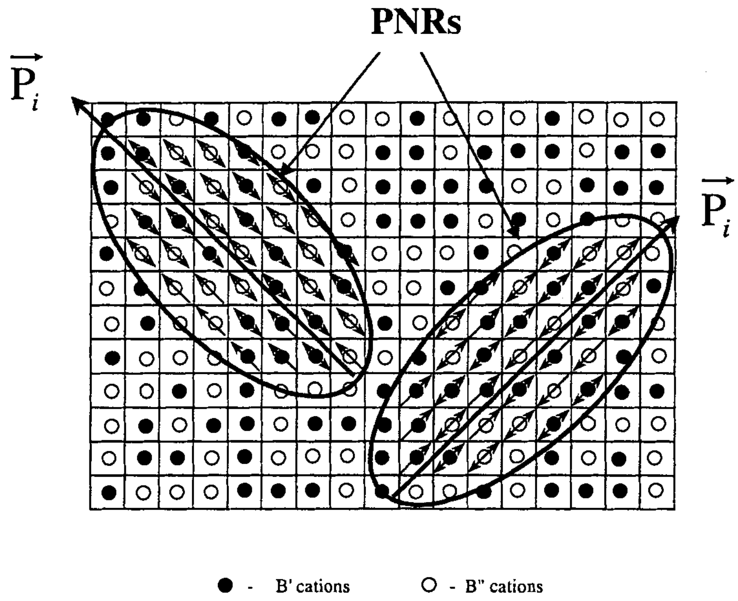

Figure 9.1: Schematic illustration of the proposed model of the interacting PNR's in the compositionally disordered $A(B'B'')O_3$ perovskite structure. A and O ions are not shown. Small arrows represent spontaneous dipole moments of "fixed" unit cells (one-end arrows) or "free" unit cells (Double-end arrows). Large arrows indicate the dipole moments *P* of individual PNRs. It is assumed in this example that the cell is ferroelectrically ordered (i.e., the direction of its moment is the same as the direction of P_i) if it has three or four B cations of the same type in the neighbouring cells and that the direction of the moment of a cell is opposite to P_i if it has no B cations of the same type in the neighbouring cells. Free cells have one or two B cations of the same type in the neighbouring cells [Ref. 27]*.

To interpret our results we apply the kinetic model of phase transitions, which is developed to describe the diffuse and sharp phase transitions in compositionally

---

* Reprinted with permission from authors, Physical Review B, Vol. 66, 064103, August 9, 2002 (Figure 9), p.7 as follows: Copyright 2002 by the American Physical Society. At the request of APS, the following link is provided [http://link.aps.org/abstract/PRB/v66/e064103], and this notice is published: Readers may view, browse, and/or download material for temporary copying purposes only, provided these uses are for noncommercial personal purposes. Except as provided by law, this material may not be further reproduced, distributed, transmitted, modified, adapted, performed, displayed, published, or sold in whole or part, without prior written permission from the publisher.

disordered crystals [145]. According to this model the PNRs begin to appear within the paraelectric phase at $T_d >> T_{0m}$ (T_{0m} is the average temperature of ferroelectric phase transition) as a result of local "phase transitions" caused by compositional inhomogeneities in the disordered crystal (the nature of these inhomogeneities and the peculiarities of polar order inside the PNRs are discussed in Refs. [146] and [27]). A schematic illustration of the model of the interacting PNR's in the compositionally disordered A(B′B″)O$_3$ perovskite structure, recently proposed by Bokov and Ye [27], is shown in Figure 9.1. The equilibrium size and number of PNRs gradually increase during cooling. At a certain lower temperature T_C the PNRs become metastable and their sudden thermally-activated growth is possible (similar to the isothermal growth of the nuclei of a new phase in the case of the normal first-order phase transition). The model parameter ρ_c (which is directly proportional to T_{0m} and inversely proportional to the diffuseness of the phase transition δ_A) determines the fraction of crystal bulk filled with PNRs at $T = T_C$. Table 9.2 lists the phase transition temperature T_{0m}, the diffuseness of the phase transition δ_A, and the kinetic model parameter ρ_c for PZN, PMN [31] and PSN (see **Chapter 5**).

Table 9.2: Phase transition temperature T_{0m}, the diffuseness of the phase transition δ_A, and the kinetic model parameter ρ_c for PZN, PMN and PSN, at f =100kHz.

Relaxors	T_{0m} (K)	δ_A (K)	$\rho_c \propto$
PMN$^{a)}$	276	41	6.7
PZN$^{a)}$	424	28	15
PSN$^{b)}$	379	22	17

$^{a)}$Ref. [31]; $^{b)}$ this work

If ρ_c is comparatively small, the concentration of PNRs at T_C is large and the thermally-activated growth of any PNR is limited by the neighboring PNRs. To form a large polar domain in some region, PNRs have to merge, i.e. the directions of their dipole moments have to change to be the same for all PNRs in this region. But the reorientation of all PNRs appears to be impossible because at least some of them are frozen. This freezing can be due to one of the following reasons: i) the temperature is too low to activate the PNRs so as to overcome the potential barrier between the states with different directions of PNR dipole moment, ii) a dipolar glass state is formed in which the directions of PNR moments are fixed by the frustrated interactions between them, iii) PNR moments are pinned by local random electric and/or elastic fields. Consequently the size and number of PNRs remain almost unchanged when the crystal passes through T_C. As a result, the long-range polar order characteristic of the ferroelectric state cannot develop and thereby no noticeable anomalies of structural parameters and dielectric (and other physical) properties can be observed. This scenario seems to be valid for PMN in which PNRs are commonly believed to exist at all temperatures below T_d and all three reasons for their freezing mentioned above can be expected.

In PZN the ρ_c parameter is larger than that in PMN due to a higher T_{0m} and a smaller phase transition diffuseness δ_A. A large ρ_c means that at T_C the concentration of PNRs is smaller (the distances between them are rather large) and they have room to grow to mesoscopic sizes large enough to be detected by X-ray and neutron diffraction experiments but smaller than the size of normal ferroelectric domains. The higher transition temperature in PZN probably facilitates the formation of the larger polar regions in another way. At a higher temperature the dipole moments of some PNRs can be reoriented by thermal motion. Consequently the growth of PNRs at T_C is accompanied by the reorientation of some of the neighboring PNRs so that several PNRs can merge to form larger ferroelectric domains (the merging decreases the energy related to the domain walls). Upon further cooling below T_C the process of domain formation goes on because of the increase in ferroelectric distortion and the transformation to the ferroelectric phase of the regions with reduced local Curie temperature. This process has been revealed in the X-ray diffraction experiments. The corresponding anomalies are observed not at a well-defined temperature, but smeared over a wide temperature interval.

PSN shows the smallest diffuseness parameter δ_A among the three relaxors, and consequently, the largest ρ_c parameter. As a result, the concentration of PNRs is small at T_C and they are free to grow into almost macroscopic ferroelectric domains.

The dielectric behaviour of relaxors is also determined by the kinetics of the formation and evolution of the PNRs and ferroelectric domains. This is because the dielectric response of relaxors in the temperature range around T_{max} arises mainly from the relaxation of PNRs and their boundaries, rather than from the non-relaxation ionic polarization related to the relative displacement of the positive and negative sublattices, as in the case of normal displacive ferroelectrics (see e.g. Ref. [147] for more detailed discussion). In the relaxors that do not undergo a transition into the ferroelectric phase upon cooling (e.g. in PMN) the temperature evolution of PNRs occurs without abrupt changes in their size and concentration and consequently there are no sharp anomalies in the temperature dependencies of permittivity. In the intermediate case of PZN, the transformation of PNRs into ferroelectric domains takes place gradually so that the dielectric permittivity changes without sharp anomalies. On the other hand, PSN, with a sharp spontaneous phase transition into the normal ferroelectric phase, shows an abrupt drop of dielectric constant at T_C due to the transformation of PNRs into macroscopic ferroelectric domains at this temperature. The long-range order ferroelectric domain state is stabilized after the phase transition and can be detected by microscopic domain observations.

The electric field applied on the PZN and PMN crystals upon cooling is able to reorient PNRs, so that all of them have the same (or almost the same) orientations of dipole moments and at T_C, where the process of intensive growth of PNRs begins, they can easily merge to form macroscopic ferroelectric domains. The number of relaxing elements (e.g. domain walls and boundaries between different phases) that are able to contribute to the dielectric constant decreases rapidly during this process, leading to the distinct dielectric anomaly at T_C. In PZN, below T_C, the dielectric dispersion is almost suppressed [Figure 8.6(a)]. Upon heating of the poled crystal, the phase transition occurs at T_C accompanied by the sharp dielectric peak [Figure 8.7(a)] indicating that the crystal transforms back to the same relaxor state with the presence of PNRs as it was in the zero-field experiments. As a result, the Vogel-Fulcher parameters remain almost unchanged (see Table 8.1). However, in contrast to the zero-field experiments, the orientations of PNRs are no longer random. Instead, the PNRs subsystem is poled (or partially poled) so that the magnitude of the permittivity is different (smaller).

9.5 General Conclusions

This work has contributed to the research and development of high piezo- and ferroelectric materials in the following aspects:

(1) Development of synthetic methods has allowed us to prepare the relaxor ferroelectric based solid solution materials of $(1\text{-}x)\text{Pb}(\text{Sc}_{1/2}\text{Nb}_{1/2})\text{O}_3 - x\text{PbTiO}_3$ both in the form of ceramics and single crystals. Solid solution system $(1\text{-}x)\text{PbSnO}_3 - x\text{PbTiO}_3$ with composition within the MPB region forms a new family of piezoelectric crystals.

(2) The studies of the structure and dielectric properties of the $\text{Pb}(\text{Sc}_{1/2}\text{Nb}_{1/2})\text{O}_3$ and PSN-PT single crystals show that the chemical (local order/disorder) and physical (phase transition, domain structure, dielectric relaxation) properties of the materials are greatly affected by the growth conditions. On the other hand, these results point out that by appropriately adjusting the growth parameters, it is possible to tune the structure and properties of the growth crystals in a large spectrum, from ordered to disordered, from relaxor to normal ferroelectric, from diffuse to sharp transition, from dispersive to non dispersive behaviour, and from polar nanodomains to macrodomains.

(3) The studies of the structure and phase transition have allowed us to establish the phase diagram of the PSN–PT solid solution system, which reveals a complex phase mixture with the presence of low symmetry (monoclinic) phase in the MPB composition range. These studies point to some common features of the MPB system, which are important for the understanding and engineering of the materials properties.

(4) The characterization of the dielectric, piezoelectric and ferroelectric properties of the materials synthesized shows that the properties of the PSN–PT and PbSnTi single crystals are comparable with the PZT ceramics. Although their

performance is lower than the currently developed PMN–PT and PZN–PT crystals, both PSN–PT and PbSnTi crystals show a T_C and more important, a T_{MPB}, higher than the PMN-PT and PZN–PT piezocrystals. Upon optimization of their chemical composition and properties, these two crystal systems are expected to show great potential for applications in high-temperature electromechanical transducers.

(5) The investigation and analysis of the phase transitions of three typical relaxor materials PMN, PZN and PSN, have shown that the macroscopic properties and the phase transitions of those relaxors are determined by the kinetics of the polar nanoregions inherently present due to compositional disorder. This provides some more insightful information for a better understanding of the microscopic mechanism of the complex relaxor ferroelectric behaviour, which remains a fascinating puzzle in solid state science.

Appendix I:
Denotation of US Navy Type (1-x)$PbZrO_3$ – $x$$PbTiO_3$ (PZT)

Source from Refs. [148, 149]**:**

- **Navy Type II PZT:**

  Lead Zirconate Titanate with high coupling coefficients. It is designed for applications that require high electromechanical activity and high dielectric constant. These are used primarily as recievors e.g. hydrophones, phono pickups, sound detectors, accelerometers, delay lines, flow detectors and flow meters.

- **Navy Type III PZT:**

  A modified Lead Zirconate Titanate composition and offers extremely low loss factor. It is specifically used as a driver that exhibits low losses under extreme driving conditions.

- **Navy Type VI PZT:**

  Lead Zirconate Titanate with high coupling coefficients. This ceramic is used as sensors that require extremely high dielectric constant and large displacements.

Appendix II:
Definition of Some Symbols Related to Piezoelectric Properties

Specific Definition of symbols [34, 85, 84, 114]:

- $\varepsilon_{33}^{T} = \varepsilon'\varepsilon_0$ ($\varepsilon_0 = 8.85 \times 10^{-12}$F/m): dielectric permittivity measured at a frequency far below the sample's piezoelectric resonance frequency. The first subscript indicates the direction of the dielectric displacement and the second indicated the direction of the electric field (at direction 3). Superscript T indicates the constant stress. Unit: Farad/meter.
- $d_{33} = D_3/T_3$: The ratio of the dielectric displacement (charge Q per unit area) produced by the piezoelectric effect and the stress applied at same direction. The first subscript indicated the direction of the dielectric displacement and the second indicated the direction of the stress. Unit: Coulomb/Newton.
- $k_{33} = \sqrt{\frac{E_e}{E_m}}$: The square root of the fraction of mechanical energy (E_m) converted to electrical energy (E_e) in each cycle, or vice versa. The first subscript indicates the direction of the electric field and the second indicates the direction of the mechanical stress.
- s_{33}^{E}: elastic compliance for stress in direction 3 (parallel to direction in which sample is polarized) and accompanying strain in direction 3, under constant electric filed (short circuit). Unit: Square meter/Newton.
- s_{33}^{D}: elastic compliance for stress in direction 3 (parallel to direction in which sample is polarized) and accompanying strain in direction 3, under constant electric displacement (open circuit). Unit: Square meter/Newton.

Appendix III:
The Detailed Results of X-ray Analysis Performed by Lorentzian Function

Lorentzian fit is to fit a curve to the active data plot, using the equation:

$$y = y_0 + \frac{2A}{\pi} \frac{w}{4(x - x_0)^2 + w^2}$$

where y_0: baseline offset; A: total area under the curve from the baseline; x_0: center of the peak; w: full width of the peak at half height.

The quantities of parameters that are listed in the results log:

R: correlation coefficient.

R^2: coefficient of determination.

ChiSquare: reduced chi^2 value of fit.

(Continue in next page)

(111) x = 0.35 (200)

```
Data: A35111_B
Model: Lorentz

Chi^2/DoF      = 0.0005
R^2     = 0.9953

y0      0.00817         ±0.00444
xc1     38.48356        ±0.00593
w1      0.27352         ±0.0122
A1      0.31542         ±0.02519
xc2     38.3204         ±0.0043
w2      0.20648         ±0.01143
A2      0.21133         ±0.02177
```

```
Data: A35200_B
Model: GaussAmp

Chi^2/DoF      = 0.00031
R^2     = 0.99631

y0      0.04687         ±0.00665
xc1     44.5464         ±0.01958
w1      0.49426         ±0.07161
A1      0.14072         ±0.02863
xc2     44.52993        ±0.00292
w2      0.21002         ±0.00485
A2      0.76965         ±0.03323
```

(111) x = 0.37 (200)

```
Data: A37p111_B
Model: Lorentz

Chi^2/DoF      = 0.00015
R^2     = 0.99796

y0      0.04985         ±0.00243
xc1     38.7863         ±0.01764
w1      0.22201         ±0.02554
A1      0.10281         ±0.05008
xc2     38.54734        ±0.02563
w2      0.32236         ±0.01975
A2      0.17465         ±0.06686
xc3     38.67019        ±0.00623
w3      0.211   ±0.04946
A3      0.19833         ±0.10727
```

```
Data: A37P200_B
Model: Lorentz

Chi^2/DoF      = 0.00025
R^2     = 0.99671

y0      0.05749         ±0.00266
xc1     45.20044        ±0.01497
w1      0.30924         ±0.05219
A1      0.13207         ±0.05686
xc2     44.96643        ±0.00935
w2      0.43387         ±0.06463
A2      0.47379         ±0.15365
xc3     44.71924        ±0.04831
w3      0.59373         ±0.04898
A3      0.24347         ±0.10224
```

(111) x = 0.38 (200)

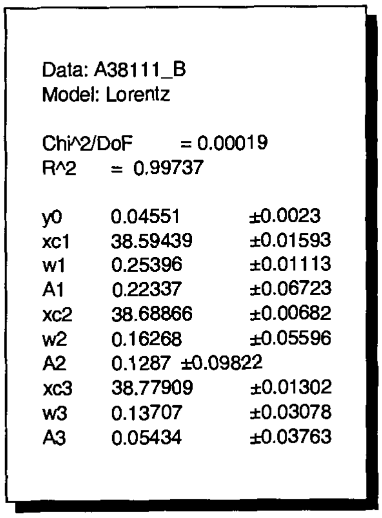

```
Data: A38111_B
Model: Lorentz

Chi^2/DoF      = 0.00019
R^2     = 0.99737

y0      0.04551         ±0.0023
xc1     38.59439        ±0.01593
w1      0.25396         ±0.01113
A1      0.22337         ±0.06723
xc2     38.68866        ±0.00682
w2      0.16268         ±0.05596
A2      0.1287 ±0.09822
xc3     38.77909        ±0.01302
w3      0.13707         ±0.03078
A3      0.05434         ±0.03763
```

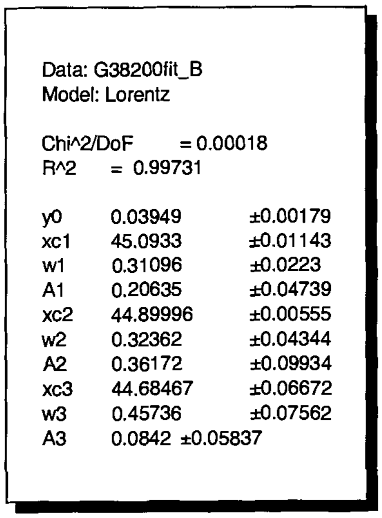

```
Data: G38200fit_B
Model: Lorentz

Chi^2/DoF      = 0.00018
R^2     = 0.99731

y0      0.03949         ±0.00179
xc1     45.0933         ±0.01143
w1      0.31096         ±0.0223
A1      0.20635         ±0.04739
xc2     44.89996        ±0.00555
w2      0.32362         ±0.04344
A2      0.36172         ±0.09934
xc3     44.68467        ±0.06672
w3      0.45736         ±0.07562
A3      0.0842 ±0.05837
```

(111) x = 0.39 (200)

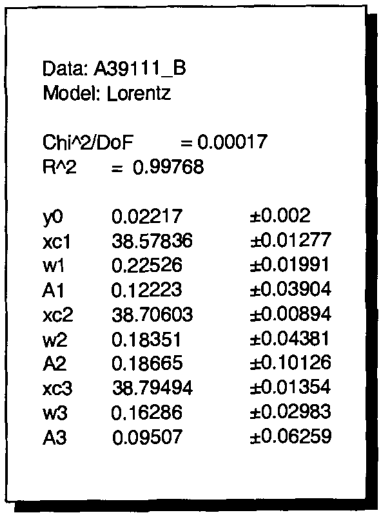

```
Data: A39111_B
Model: Lorentz

Chi^2/DoF      = 0.00017
R^2     = 0.99768

y0      0.02217         ±0.002
xc1     38.57836        ±0.01277
w1      0.22526         ±0.01991
A1      0.12223         ±0.03904
xc2     38.70603        ±0.00894
w2      0.18351         ±0.04381
A2      0.18665         ±0.10126
xc3     38.79494        ±0.01354
w3      0.16286         ±0.02983
A3      0.09507         ±0.06259
```

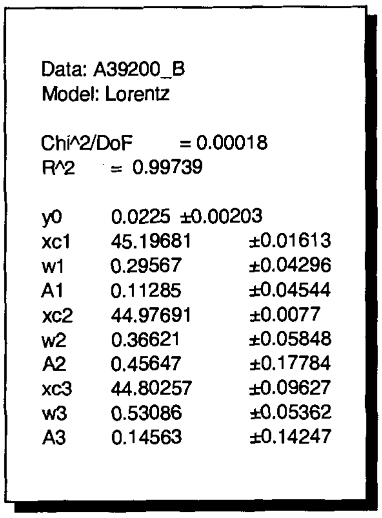

```
Data: A39200_B
Model: Lorentz

Chi^2/DoF      = 0.00018
R^2     = 0.99739

y0      0.0225 ±0.00203
xc1     45.19681        ±0.01613
w1      0.29567         ±0.04296
A1      0.11285         ±0.04544
xc2     44.97691        ±0.0077
w2      0.36621         ±0.05848
A2      0.45647         ±0.17784
xc3     44.80257        ±0.09627
w3      0.53086         ±0.05362
A3      0.14563         ±0.14247
```

(111) x = 0.41 (200)

```
Data: A41P111_B
Model: Lorentz

Chi^2/DoF      = 0.00028
R^2     = 0.99587

y0      0.06812        ±0.00248
xc1     38.77094       ±0.01698
w1      0.18935        ±0.01746
A1      0.16206        ±0.08941
xc2     38.68916       ±0.01315
w2      0.16065        ±0.10208
A2      0.09994        ±0.15127
xc3     38.5926        ±0.02199
w3      0.21204        ±0.02202
A3      0.12554        ±0.07003
```

```
Data: A41P200_B
Model: Lorentz

Chi^2/DoF      = 0.00018
R^2     = 0.9976

y0      0.05302        ±0.00205
xc1     44.88557       ±0.0273
w1      0.4545 ±0.01246
A1      0.42115        ±0.13192
xc2     45.19222       ±0.014
w2      0.26599        ±0.02799
A2      0.14099        ±0.04941
xc3     45.02322       ±0.01438
w3      0.29269        ±0.12075
A3      0.16406        ±0.16728
```

(111) x = 0.42 (200)

```
Data: A42111_B
Model: Lorentz

Chi^2/DoF      = 0.00011
R^2     = 0.99861

y0      0.02215        ±0.00174
xc1     38.61474       ±0.00789
w1      0.19745        ±0.01043
A1      0.1179 ±0.02023
xc2     38.80556       ±0.00679
w2      0.19184        ±0.00723
A2      0.17003        ±0.02783
xc3     38.7185        ±0.00391
w3      0.14279        ±0.02647
A3      0.10829        ±0.04222
```

```
Data: A42200_B
Model: Lorentz

Chi^2/DoF      = 0.0003
R^2     = 0.99596

y0      0.03142        ±0.00211
xc1     44.73351       ±0.0235
w1      0.48946        ±0.03619
A1      0.25185        ±0.0618
xc2     45.00254       ±0.00991
w2      0.40304        ±0.07298
A2      0.30274        ±0.101
xc3     45.2494        ±0.00452
w3      0.28262        ±0.01621
A3      0.31357        ±0.03981
```

(111) x = 0.45 (200)

```
Data: A45111_B
Model: Lorentz

Chi^2/DoF      = 0.00016
R^2    = 0.99787

y0     0.02656        ±0.00239
xc1    38.71618       ±0.00602
w1     0.26132        ±0.00663
A1     0.35096        ±0.03142
xc2    38.82183       ±0.00954
w2     0.17878        ±0.02557
A2     0.07158        ±0.02808
```

```
Data: A45200_B
Model: Lorentz

Chi^2/DoF      = 0.00036
R^2    = 0.99357

y0     0.04037        ±0.00241
xc1    44.46691       ±0.0084
w1     0.42151        ±0.02766
A1     0.19465        ±0.02003
xc2    44.94313       ±0.0189
w2     0.55135        ±0.105
A2     0.19121        ±0.0502
xc3    45.30151       ±0.00256
w3     0.3216 ±0.01043
A3     0.4435 ±0.02496
```

(111) x = 0.50 (200)

```
Data: A50111_B
Model: Lorentz

Chi^2/DoF      = 0.00011
R^2    = 0.99831

y0     0.02478        ±0.00152
xc1    38.84828       ±0.00528
w1     0.16627        ±0.01228
A1     0.0799 ±0.01384
xc2    38.73959       ±0.00288
w2     0.21195        ±0.00447
A2     0.28589        ±0.01497
```

```
Data: A50200_B
Model: Lorentz

Chi^2/DoF      = 0.00021
R^2    = 0.99458

y0     0.03755        ±0.00137
xc1    44.35619       ±0.00367
w1     0.34989        ±0.01357
A1     0.18329        ±0.00848
xc2    45.4058        ±0.0011
w2     0.28531        ±0.00435
A2     0.41971        ±0.00748
xc3    44.89797       ±0.01994
w3     0.5961 ±0.10755
A3     0.09094        ±0.01773
```

Reference List

[1] S.–E. Park, and W. Hackenberger, *Curr. Opin. Solid State & Mater. Sci.* **6,** 11 (2002).

[2] W. G. Cady, *Piezoelectricity*, Dover Publications, Inc. New York (1964).

[3] G. H. Haertling, *J. Am. Ceram. Soc,* **82**[4], 797 (1999).

[4] Y.-H. Xu, *Ferroelectric Materials and Their Applications.* North-Holland, the Netherlands (1991).

[5] M. E. Lines and A. M. Glass, Principles and Applications of Ferroelectrics and Related Materials, Clarendon, Oxford, UK (1977).

[6] L. E. Cross and K. H. Härdtl, *Encyclopedia of Chemical Technology* **10**, 1 (1980).

[7] R. E. Eitel, Ph. D thesis in materials science and engineering, the Pennsylvania state university (2003).

[8] F. Jona & G. Shirane, *Ferroelectric Crystals,* Dover Publications Inc., New York (1993).

[9] G. Shirane and S. Hoshino, *J. Phys. Soc. Jpn.* **6**, 265 (1951).

[10] L. E. Cross, *Ferroelectrics* **76,** 241 (1987); *Ferroelectrics* **151**, 305 (1994).

[11] Z.-G. Ye, *Key Eng. Mater.* **155 – 156,** 81 (1998).

[12] G. Burns and B. A. Scott, *Solid State Commun.* **13**, 423 (1973).

[13] C. G. Stenger, F. L. Scholten and A. J. Burgraaf, *Solid State Commun.* **32,** 989 (1979).

[14] C. G. Stenger and A. F. Burgraaf, *Phys. Stat. Sol.* (a) **61,** 275 (1980).

[15] C. G. Stenger and A. F. Burgraaf, *Phys. Stat. Sol.* (a) **61**, 653 (1980).

[16] N. Setter and L. E. Cross, *J. Mater. Sci.* **15,** 2478 (1980).

[17] N. Setter and L. E. Cross, *J. Appl. Phys.* **51**(8), 4356 (1980).

[18] D. Vieland and J. F. Li, *J. Appl. Phys*, **75**(3), 1705 (1994)

[19] F. Chu, N. Setter, and A. K. Tagantsev, *J. Appl. Phys*, **74**(8), 5129 (1993).

[20] A. A. Bokov, *Ferroelectrics* **183**, 65 (1996).

[21] G. A. Smolenskii, *J. Phys. Soc. Japan*, **28** Suppl. 26 (1970).

[22] V. A. Isupov, *Ferroelectrics*, **90** 113 (1989); **143**, 109 (1993).

[23] D. Viehland, S. J. Jang, and L. E. Cross, *J. Appl. Phys.* **68**(6), 2916 (1990).

[24] V. Westphal and W. Kleemann, *Phys. Rev. Letters,* **68** (6), 847 (1992).

[25] A. A. Bokov and Z.-G. Ye, *J. Phys.: Condens. Matter* **12**, L541 (2000).

[26] A. A. Bokov and Z.-G. Ye, *Phys. Rev. B,* **65**, 144112 (2002).

[27] A. A. Bokov and Z.-G. Ye, *Phys. Rev. B*, **66**, 064103 (2002).

[28] R. Blinc, J. Dolinsek, A. Gregorovic, B. Zalar, C. Filipic, Z. Kutnjak, A. Levstik and R. Pirc, *Phys. Rev. Lett.* **83**, 424 (1999).

[29] R. Pirc and R. Blinc, *Phys. Rev. B,* **60,** 13470 (1999).

[30] A. A. Bokov and Z. –G. Ye, *Solid State Commun.* **116**, 105 (2000).

[31] A. A. Bokov, Y. H. Bing, W. Chen, and Z. –G. Ye, *Phys. Rev. B,* **68,** 052102 (2003).

[32] G. Shirane, K. Suzuki and A. Takeda, *J. Phys. Soc. Jpn.* 7, 12 (1952).

[33] G. Shirane and K. Suzuki, *J. Phys. Soc. Jpn.* 7, 333 (1952).

[34] B. Jaffe, W. R. Cook, and H. Jaffe, *Piezoelectric Ceramics*, Academic Press, London (1971).

[35] B. Noheda, D. E. Cox, G. Shirane, J. A. Gonzalo, L. E. Cross, and S-E. Park, *Appl. Phys. Lett.* **74,** 2059 (1999).

[36] B. Noheda, D. E. Cox, G. Shirane, R. Guo, B. Jones, and L. E. Cross, *Phys. Rev. B*, **63**, 014103 (2000).

[37] L. Bellaiche, A. Garcia, and D. Vanderbilt, *Phys. Rev. Lett.* **84**, 5427 (2000).

[38] H. Fu and R. E. Cohen, *Nature*, **403**, 281 (2000).

[39] A. Amin, R. E. Newnham, L. E. Cross, and D. E. Cox, *J. Solid State Chem.* **37**, 248 (1981).

[40] X.–H. Du, J. Zheng, U. Belegundu, K. Uchino, *Appl. Phys Lett,* **72**, 2421 (1998).

[41] J. F. Nye, *Physical properties of crystals*, Oxford, Clarendon Press (1985)

[42] L. E. Cross, Proceedings of the workshop on Fundamental Physics of Ferroelectrics, Aspen, New York (2000).

[43] S.–E. Park and T. R. Shrout, *Science*, **275**, 1878 (1997).

[44] J. Kuwata, K. Uchino, and S. Nomura, *Ferroelectrics* **37**, 579 (1981).

[45] T. R. Shrout, Z. P. Chang, M. Kim, and S. Markgraf, *Ferroelec. Lett.* **12**, 63 (1990).

[46] S.–E. Park, and T. R. Shrout, *J. Appl. Phys.*, **82**, 1804 (1997).

[47] S. Wada, S.-E. Park, L. E. Cross, and T. R. Shrout, presented at 9th International Meeting on Ferroelectricity, Seoul, Korea, 24-27 August, (1997).

[48] M. K. Durbin, E. W. Jacobs and J. C. Hicks, *Appl. Phys. Lett.* **74**, 2848 (1999).

[49] B. Noheda, *Curr. Opin. Solid State & Mater. Sci.* **6,** 27 (2002).

[50] D. E. Cox, B. Noheda, G. Shirane, Y. Uesu, K. Fujishiro, and Y. Yamada. *Appl. Phys. Lett.* **79**, 400 (2001).

[51] B. Noheda D.E. Cox, G. shirane, S.–E. Park, L. E. Cross and Z. Zhong, *Phys. Rev. Lett.* **86**, 3891 (2001).

[52] Z.–G. Ye, B. Noheda, M. Dong, D. E. Cox, and G. Shirane, *Phys. Rev. B*, **64**, 184114 (2001).

[53] Z.–G. Ye and M. Dong, *J. Appl. Phys.*, **87**(5), 2312 (2000).

[54] G. Xu, H. Lou, H. Xu, and Z. Yin, *Phys. Rev. B*, **64**, 020102 (2001).

[55] A. K. Sing, and D. Pandey, *J. Phys. Condens. Matter.* **13**, L931 (2001).

[56] J.-M. Kiat, Y. Uesu, B. Dkhil, M. Masuta, C. Malibert, and G. Calvarin, *Phys. Rev. B*, **65**, 064106 (2002).

[57] B. Noheda, D. E. Cox, G. Shirane, J. Gao, and Z.–G. Ye, *Phys. Rev. B,* **66,** 054104 (2002).

[58] Z.–G. Ye, *Curr. Opin. Solid State & Mater. Sci.* **6,** 35 (2002).

[59] M. Dong and Z.–G. Ye, *J. Cryst. Growth,* **209**, 81 (2000).

[60] W. Chen and Z.–G. Ye, *J. Cryst. Growth,* **233,** 503 (2001).

[61] H. Luo, G. Xu, P. Wang, and Z. Yin, *Ferroelectrics* **231**, 97 (1999).

[62] L. Zhang, M. Dong, and Z.–G. Ye, *Mater. Sci. Eng. B*, **78**, 96 (2000).

[63] F. J. Kumar, L. C. Lim, C. Chilong, and M. J. Tan, *J. Cryst. Growth,* **216**, 311 (2000).

[64] S. J. Zhang, P. W. Rehrig, C. A. Randall, and T. R. Shrout, *J. Cryst. Growth,* **234**, 415 (2002). S. J. Zhang, C. A. Randall, and T. R. Shrout, *Jpn. J. Appl. Phys.*, **41**, 722 (2002).

[65] R. E. Eitel, C. A. Randall, T. R. Shrout, P. W. Rehrig, W. Hackenberger and S–E. Park, *Jpn. J. Appl. Phys.*, **40**, 5999 (2001).

[66] S. J. Zhang, C. A. Randall, and T. R. Shrout, *Appl. Phys. Lett.* **83**, 3150 (2003).

[67] Y. Yasuda, H. Ohwa, K. Ito, M. Iwata, and Y. Ishibashi, *Ferroelectrics,* **230**, 115 (1999). Y. Yasuda, H. Ohwa, M. Kume, Y. Yamashita, *Jpn. J. Appl. Phys.*, **39**, L66 (2000). Y. Yasuda, H. Ohwa, H. Hasegawa, K. Hayashi, Y. Hosono, Y. Yamashita, M. Iwata, and Y. Ishibashi, *Jpn, J. Appl. Phys.*, **39**, 5586 (2000).

[68] G. A. Smolenskii, V. A. Isupov and A. I. Agranovskaya, *Sov. Phys. Solid State* **1**, 150 (1959).

[69] F. Galaso and W. Darby, *Inorg. Chem.*, **4**, 71 (1965).

[70] V. G. Smotrakov, I. P. Raevskii, M. A. Malitsskaya, S. M. Zaitsev, Yu. M. Popov and N. A. Strekneva, *Inorg. Mater.* **19**, 105 (1983).

[71] V. J. Tennery, K. W. Hang, and R. E. Novak, *J. Am. Cera. Soci.* **51**(12), 671 (1968).

[72] Y. Yamashita, *Jpn. J. Appl. Phys.*, **33**, 5328 (1994).

[73] Y. Yamashita, and S. Shimanuki, *Mater. Res. Bull.* **31**(7), 887 (1996).

[74] Y. Yamashita, and K. Hardada, *Jpn. J. Appl. Phys.*, **36**, 6039 (1997).

[75] K. Yanagisawa, J. C. Rendon-Angeles, H. Kanai, and Y. Yamashita, *J. Mater. Sci. Lett.* **17,** 2105 (1998).

[76] D. La-Orauttapong, B. Noheda, Z.–G, Ye, P. M. Gehring J. Toulouse, D. E. Cox and G. Shirane, *Phys. Rev. B*, **65**, 144101 (2002).

[77] S. W. Choi. T. R. Shrout, S. J. Jang and A. S. Bhalla, *Ferroelectrics*, **100**, 29 (1989).

[78] F. Chu, I. M. Reaney, and N. Setter, *Ferroelectrics*, **151**, 343 (1994).

[79] Z.–G. Ye, Y.–H. Bing, J. Gao, A. A. Bokov, P. Stephens, B. Noheda, and G. Shirane, *Phys. Rev. B*, **67**, 104104 (2003).

[80] S. Normura, *J. Phys. Soc. Jpn.*, **10**[2], 112 (1955).

[81] G. A. Smolensiki, A. I. Agranovskaya, A. M. Kalinin, and T. M. Fedorova, *Zh. Tekh. Fiz.*, **25**, 2134 (1955).

[82] B. Jaffe, R. S. Roth and S. Marzullo, *J. Res. Nat. Bur. Sta.*, **55**[5], 239 (1955).

[83] G. H. Stout and L. H. Jensen, X-ray structure determination, John Wiley & Son, New York (1989).

[84] http://americanpiezo.com/piezo_theory.

[85] An American National Standard IEEE Standard on Piezoelectricity (1979)

[86] S. J. Zhang, C. A. Randall and T. R. Shrout, *J. Appl. Phys.*, **95**(b), 4291 (2004).

[87] C. B. Sawyer and C. H. Tower, *Phys. Rev.*, **35**, 269 (1930).

[88] J. K. Sinha, *J. sci. Instrum.* **42**, 696 (1965).

[89] A Mech. Tech. Inc operating manual, Internet websites: http://www.mtiinstruments.com/pdf/mti2000.pdf

[90] H. Schmid, *Ferroelectric Ceramics*, edited by N. Sette and E. L. Cola, Birkhäuser, Basel, 107 (1991).

[91] M. Francon and S. Mallick, *Polarization Interferometers*, Wiley-Interscience, (a division of John Wiley & Sons Ltd.), New York (1971).

[92] R. Guo, L. E. Cross, S–E. Park, B. Noheda, D. E. Cox, and G. Shirane, *Phys. Rev. Lett.* **84**, 5423 (2000).

[93] K. Ohwada, K. Hirota, P. W. Rehrig, Y. Fujii, and G. Shirane, *Phys. Rev. B* **67**, 09411 (2003).

[94] Y. Yamashita, Jpn. *J. Appl. Phys.* **33,** 4652 (1994).

[95] Y.–H. Bing, and Z.–G. Ye, J. Crystal Growth, **250**, 118 (2003); Y.–H. Bing and Z.–G. Ye, Proceedings of the 13th IEEE International Symposium on Applications of Ferroelectrics, May, ISAF (2002).

[96] R. Haumont, B. Dkhil, J. M. Kiat, A. Al-Barakaty, H. Dammak, and L. Bellaiche, *Phys. Rev. B* **68**, 014114 (2003).

[97] T. R. Shrout and A. Halliyal, *Am. Ceram. Soc. Bull.,* **66** [4] 704 (1987).

[98] R. D. Shannon, *Acta Crystallogr.* A32, 751 (1976).

[99] S. S. Zumadahl, *Chemical Principles,* (third Edition), Houghton Mifflin Company, Boston, New York (1998).

[100] M. Inada, *Jpn. Natl. Tech. Rept.,* **27** [1] 95 (1977).

[101] S. L. Swartz and T. R. Shrout, Matr. Res. Bull. **17** 1245 (1982).

[102] Y. Yamashita, *Jpn. J. Appl. Phys.* **32** 5036 (1993). M. Adachi, T. Toshima, M. Takahashi, Y. Yamashita and A. Kawabata, *Jpn. J. Appl. Phys.* **34** 5324 (1995). M. Adachi, E. Miyabukuro and A. Kawabata, *Jpn. J. Appl. Phys.* **33** 5420 (1994)

[103] S. Shimanuki, S. Saitoh and Y. Yamashita, *Jpn. J. Appl. Phys.* **37,** 3382 (1998).

[104] Z.-G. Ye and H. Schmid, *Ferroelectrics* **145**, 83 (1993).

[105] M. A. Eisa, M. F. Abadir, and A. M. Gadalla, *Trans. J. Br. Ceram. Soc.* **79**[4], 100 (1980).

[106] R. F. Geller and E. N. Bunting, *J. Research Nat. Bur. Standards* **18**[5]. 585 (1937).

[107] E. M. Levin, *J. Research Nat. Bur. Standards* **70A**[1], 12 (1966).

[108] L. Zhang, M. Sc. thesis in department of Chemistry, Simon Fraser University (2000).

[109] A. A. Chernov, *Modern Crystallography III*, Springer-Verlag, Berlin Heidelberg, (1984).

[110] R. A. Laudise, *The Growth of Single Crystals*, New Jersey, Prentice-Hall Inc. (1970).

[111] N. Cabrera and R. V. Coleman, *The Art and Science of Growing Crystals*, Edit by J. J. Gilman, John Wiley & Sons, Inc., New York (1963).

[112] Y. Saito, *Statistical Physics of Crystal Growth*, Singapore, World Scientific, (1996).

[113] W. D. Lawson and S. Nielsen, *Preparation of Single Crystal*, London, Butterworths Scientific Publications (1958).

[114] J. Gao, M. Sc. thesis in department of Chemistry, Simon Fraser University (2003).

[115] A. A. Bokov, I.P. Raevskii, V. G. Smorkov, and S. M. Zaitsev, *Sov. Phys. Crystallogr.* **32**(5), 769 (1987).

[116] F. Chu, I. M. Reaney, and N. Setter, *J. Appl. Phys.* **77**(4), 1671 (1995).

[117] F. Chu, I. M. Reaney, and N. Setter, *J. Am. Ceram. Soc.* **78**(7), 1947 (1995).

[118] Work underway in collaboration with G.A. Samara, Sandia National Laboratories, Albuquerque (2005).

[119] A. A. Bokov, *JETP* **84** (5), 994 (1997).

[120] H. Vogel, *Phys. Z.* **22**, 645 (1921).

[121] G. Fulcher, *J. Am. Ceram. Soc.* **8**, 339 (1925).

[122] K. Wôjcik, *Ferroelectrics* **82**, 25 (1988).

[123] L. E. Cross, *Nature*, **432**, 24 (2004).

[124] K. K. Rajan, Y.S. Ng, J. Zhang and L. C. Lim, *Appl. Phys. Lett.* **85**[18], 4136 (2004).

[125] Y. Yasuda, H. Ohwa, M. Kume, and Y. Yamashita, *J. Cryst. Growth*, **229**, 299 (2001).

[126] See, for a review, L. E. Cross, *Ferroelectrics* **151**, 305 (1994); Z.-G. Ye, *Key Eng. Mater.* **155-156**, 81 (1998); A. A. Bokov, *Ferroelectrics* **131**, 49 (1992).

[127] See, for a review, S.-E. Park and W. Hackenberger, *Curr. Opin. Solid State Mater.* Sci. **6**, 11 (2002); L. Bellaiche, *ibid.* **6**, 19 (2002); B. Noheda, *ibid.* **6**, 27 (2002); Z.-G. Ye, *ibid.* **6**, 35 (2002).

[128] P. M. Gehring, S. Wakimoto, Z.-G. Ye and G. Shirane, *Phys. Rev. Lett.* **87**, 277601 (2001).

[129] S. Wakimoto, C. Stock, R. J. Birgeneau, Z.-G. Ye, W. Chen, W. J. L. Buyers, P. M. Gehring and G. Shirane, *Phys. Rev. B* **65**, 172105 (2002).

[130] C.-S. Tu, V. H. Schmidt, and I. G. Siny, *J. Appl. Phys.* **78**, 5665 (1995).

[131] K. Hirota, Z.-G. Ye, S. Wakimoto, P. Gehring, and G. Shirane, *Phys. Rev. B* **65**, 104105 (2002).

[132] Z.-G. Ye, *Ferroelectrics* **172**, 19-30 (1995).

[133] G. Calvarin, E. Husson and Z.-G. Ye, *Ferroelectrics* **165**, 349 (1995).

[134] G. A. Smolenskii, N. N. Krainik, A. A. Berezhnoi, and I. E. Myl'nikova, Soviet *Phys.-Solid State* **10**, 2105 (1969).

[135] Y. Yokomizo, T. Takahashi, and S. Nomura, *J. Phys. Soc. Jpn.* **28**, 1278 (1970).

[136] S. Nomura, M. Endo, and F. Kojima, *Jpn. J. Appl. Phys.* **13**, 2004 (1974).

[137] Z.-G. Ye, M. Dong and L. Zhang, *Ferroelectrics* **229,** 223 (1999).

[138] A. Lebon, H. Dammak, G. Galvarin and I. Ould Ahmedou, *J. Phys.: Condens, Matter* **14**, 7035 (2002).

[139] G. Xu, Z. Zhong, Y.-H. Bing, Z.-G. Ye, C. Stock, and G. Shirane, *Phys. Rev. B* **67**, 104102 (2003).

[140] C. Stock, R.J. Birgeneau, S. Wakimoto, J.S. Gardner, W. Chen, Z.-G. Ye, and G. Shirane, *Phys. Rev. B* **69,** 094104 (2004).

[141] P. Bonneau, P. Garnier, G. Calvarin, H. Husson, J.R. Gavarri, A.W. Hewat, and A. Morell, *J. Solid State Chem.* **91**, 350 (1991).

[142] N. Mathan, E. Husson, G. Calvarin, J. R. Gavarri, A. W. Hwat and A. Morell, *J. Phys.: Condens Matter*, **3**, 8159 (1991).

[143] B. Dkhil, J. M. Kiat, G. Calvarin, G. Baldinozzi, S. B. Vakhrushev, and E. Suard, *Phys. Rev. B* **65**, 024104 (2002).

[144] G. Xu, Z. Zhong, Y.-H. Bing, Z.-G. Ye, C. Stock, and G. Shirane, *Phys. Rev. B* **70**, 064107 (2004).

[145] A. A. Bokov, *Phys. Solid State* **36**, 19 (1994); *Ferroelectrics* **190**, 197 (1997).

[146] A. A. Bokov *JEPT* **84**, 994 (1997); *Sold State Commun.* **90,** 687 (1994).

[147] Z.-G. Ye and A. A. Bokov, *Ferroelectrics* **302,** 473 (2004).

[148] http://www.piezo-kinetics.com.

[149] http://www.sensortech.ca.